

Optotronics: Optically Inspired Electronics

Thesis by

Ehsan Afshari

In Partial Fulfillment of the Requirements

for the Degree of

Doctor of Philosophy



California Institute of Technology

Pasadena, California

2006

(Submitted July 28, 2006)

© 2006

Ehsan Afshari

All Rights Reserved

To Him who taught me to love

To my mother
for her unconditional love

Acknowledgements

During my graduate study at Caltech, I have had the chance to interact with many talented and motivated individuals in multiple disciplines, from all over the world. The most essential lesson that I learned from them, was looking at what everyone else has looked at, and seeing something new. This is the most important key to good research. I would like to express my gratitude to those who have helped me to gain this skill.

First and foremost, I would like to thank my advisor Prof. Ali Hajimiri. He has always been a good friend whom I can count on, and looked after me like an older brother. Despite our many differences, I always enjoy talking to him about all matter of things, from physics to politics. Academically, he has been a fantastic advisor who gave me the freedom to choose my project. He has been extremely patient with me and helped me in all stages of this work. He helped me to choose my carrier path, and fully supported me in pursuing it. He has taught me much and I deeply respect and care for him as a friend and a teacher.

Next, I would like to thank Prof. Jerrold Marsden and Prof. Harish Bhat for their tremendous impact on this work. They convinced me that I am not a mathematician, and helped me realize the power of collaboration. We first started working together in the summer of 2004, when Jerry kindly accepted to help me with my project. He introduced me to Harish, an exceptional mathematician and thinker, without whom this work would not have gone this far. We began a fruitful partnership which holds high hopes for the future. Harish has also been a good friend, whose knowledge and contribution goes well beyond mathematics.

I owe my passion for electronics to my undergraduate advisor Prof. Mehrdad

Sharif-Bakhtiar. He is an extraordinary teacher who could explain the most difficult concepts in a very simple form. He also taught me to be patient in research and showed me the importance of being organized.

Also I would like to thank Prof. Dimitri Psaltis, Prof. David Rutledge, Prof. Sander Weinreb, and Prof. Jerrold Marsden, my candidacy exam committee members, for their valuable feedbacks. Their technical advice improved the quality of this work, while by sharing their personal experiences they helped clarifying my future carrier options. I would like to thank them for their input and support along the way.

Special thanks to my great colleagues and friends who had a substantial influence on my work at Caltech, especially I would like to thank Abbas Komijani for being a great technical and emotional support during the past five years, and Prof. Donhee Ham for helping me to choose the topic of this theses. Additionally, I would like to express my gratitude to all the help and support which was provided by Dr. Behnam Analui and Prof. Hossein Hashemi. Also I would like to thank Prof. Arjang Hassibi, Prof. Hui Wu, Sam Mandegaran, Dr. Saleem Mukhtar, Prof. Jim Buckwalter, Dr. Xiang Guan, Dr. Chris White, Dr. Roberto Aparicio, Edward Keehr, Florian Bohn, Aydin Babakhani, Yu-Jiu Wang, and Hua Wang.

I am also thankful to my friends in Caltech, especially Amir Sadjadpour who tolerated me as a roommate for two years. He has been a true friend, full of love and compassion. I am also grateful to Prof. Babak Hassibi, Mazhar Taghavi, Abbas Nasiraei Moghaddam, Prof. Masoud Sharif, Amir Faraji-Dana, Helia Naemi, Ali Vakili, Arash Yavari, and Shervin Taghavi.

I would also like to thank Soroush Abbaspour, Leila Alinaghian, Ali Asghari, Hossein Ataei, Farnoush Banaie Kashani, Alireza Doustan, Mahdi Ebrahimian, Amir Farid, Marmar Ghadiri, Amin Ghaemi, Reza JafarKhani, Mehrdad Jahangiri, MohammadReza Jahanshahi, Amirpouya Kavousian, Ehsan Kazemian, Hadi kazemian, Mahdi Kazemian, Hadi Meidani, Saeed Mohammadi, Arezoo Momeni, Omid Momeni, Ali Niazi, Arash Noshadravan, Richard Ohanian, Mahshid Rahmani, Azadeh Rasouli, Maryam Sharif, Mehdi Sharifzadeh, Amir Tarighat-Monfared, Zahra Tehrani, Yousof Zandi, and Hadi Zandi. Thank you for *sharing*.

I have been very lucky to be surrounded by a loving family. I would like to thank Parisa and Erfan for their emotional support and love. As an older sister, Parisa has always been a source of great inspiration. Without a doubt, she is one of the most energetic and goal oriented people that I have ever known. I would also like to thank my in-laws for accepting me as their own. I like to thank Dr. Hossein Azarmnia for being such a great father, full of wisdom and motivation, Mansoureh Sheikhnia for being the coolest mother in-law, full of love and positive energy. I never imagined having a mother in-law like her. I am always eagerly waiting for the weekend when I would meet, and spend time with them. Also I like to thank Morteza for being a great brother. I know that I can always count on him, and I know how much he cares about the family, although he does not make a big show of it. I'd like to thank Mahdi Nilforoushan and Mahboubeh Azarmnia for being great friends to me. This list would not be complete without Daei Reza and Daei Kazem whom I've always enjoyed talking to about almost everything, thank you for your kindness and support.

I would like to thank my other half, Monir, for being a great support for me. Without a doubt the most important achievement of my life is finding her, she is everything that I could ask for. In short, she is my best friend in the journey of life. I don't know how to thank her, Mamnoon Monir! I would also like to thank my mother, Tahereh, for her huge impact in my life. She has been both a mother and father to me. She watched me and looked after me in all stages of my life, and made sacrifices for my advancement that are extraordinary, even for a mother. I would not be who I am today without her unconditional love and support.

Finally, I would like to thank the source of these loves and supports. He has done a lot for me: surround me with the the best people, gave me everything that I asked for, gave me a lot that I did not ask for. But the best thing that He ever did was to give me the privilege to know and love Him.

Abstract

Waves are everywhere, from the distribution of cars on a highway to the wave patterns in the ocean. Intriguing phenomena in wave propagation, such as Soliton resonance, kink-antikink interaction, self-focusing, and Peakon generation can be used in many practical applications leading to novel architectures for signal processing and generation. These E/M based approaches could be particularly useful in the case of Extremely Wide Band (EWB) (DC to more than 100GHz) circuits and systems where the limited transistor cut-off frequency, maximum power efficiency, and breakdown voltage pose serious constraints on the use of conventional circuit techniques.

To overcome the limitations of active devices in EWB signal processing and generation, we propose a general class of solutions based on novel circuit topologies inspired by commonly used structures in electromagnetics, and more specifically optics. The proposed methodology is based on nonlinear and/or inhomogeneous one-dimensional (1D) transmission lines which we have successfully extended to two-dimensional transmission lattices. The principles behind these designs stem from the mathematical theory of linear and nonlinear wave propagation. By analyzing the models for the transmission lines/lattices, we are able to exploit the large body of theory to design circuits, demonstrating the narrowest reported pulse on silicon (2.5ps), and for a single integrated-circuit silicon-based amplifier, the highest achieved center frequency of operation (85GHz) and the highest achieved power output (120mW) at this frequency. In addition, we have reported the first in-silicon transmission line system capable of sharpening both rising and falling edges of NRZ data by increasing the bandwidth. In the end, we will also present how the same approach can be applied to realize ultra-fast computation systems (such as a sub-nanosecond Fourier and Hankel

transformers in silicon) and other structures, leading to a new design discipline we like to call “Optotronics”.

Contents

Acknowledgements	iv
Abstract	vii
1 Introduction	1
1.1 Contributions	3
1.2 Organization	4
2 Wave Propagation	6
2.1 Nonlinear Phenomena	6
2.1.1 Soliton	10
2.2 Wave Propagation in Periodic Structures	13
2.2.1 Fermi-Pasta-Ulam Experiment: Birth of Soliton	13
2.3 Nonlinear Waves in Electronics	15
2.3.1 Motivation	15
2.3.2 Electrical Wave Propagation Medium	16
2.3.2.1 Sources of Nonlinearity	18
2.3.3 Historical Remarks	19
3 Theory of One-Dimensional Transmission Line	22
3.1 Uniform Nonlinear 1D Transmission Lines	23
3.1.1 Discreteness Generates Dispersion	24
3.1.2 Traveling Wave Solutions	25
3.1.3 Reduction to KdV	26

3.1.4	Remark 1: Zero-Dispersion Case	27
3.1.5	Remark 2: Linear Case	28
3.1.6	Frequency Response	28
3.2	Nonuniform Linear 1D	29
3.2.1	Linear case	30
3.2.2	Physical Scenario	31
3.2.3	Non-Dimensionalization	32
3.2.4	Exponential Tapering	32
3.2.5	Perturbative Solution	33
3.2.6	Discussion	34
3.2.7	General Case	35
3.3	Nonuniform Nonlinear Case	37
3.4	Numerics	39
3.4.1	Scheme	39
3.4.2	Remark	40
3.4.3	Results	40
4	Theory of Two-Dimensional Transmission Lattice	44
4.1	Nonuniform Linear Case	45
4.1.1	Large Lattice	47
4.1.2	Lens/Funnel	48
4.1.3	A Physical Scenario	49
4.1.4	Exact Solutions	50
4.1.5	Properties	52
4.1.6	Discussion	53
4.2	Nonuniform Nonlinear Case	54
4.3	Numerics	56
4.3.1	Linear case.	57
4.3.2	Nonlinear Case	60

5	Scattering Theory for Electrical lines/lattices	64
5.1	One-Dimensional Transmission Line	64
5.1.1	Continuum Model	65
5.1.2	Schrödinger Equation	68
5.1.3	Exponentially Tapered Line	71
5.1.4	Scattering	72
5.1.5	Reflection Coefficient for Matched Case	73
5.2	Two-Dimensional Transmission Lattice	76
5.2.1	Continuum Model	76
5.2.2	Electrical Funnel	78
5.2.3	Electrical Lens	78
6	Extremely Wideband Signal Generation and Processing	80
6.1	Pulse Narrowing Non-Linear Transmission Line	81
6.1.1	Intuitive Explanation	83
6.1.2	Pulse Degeneration Problem	84
6.2	Edge Sharpening Line	85
6.2.1	Intuitive Explanation	86
6.3	The Effect of Loss	89
6.4	Simulations	91
6.4.1	Pulse Narrowing Line	92
6.4.2	Edge Sharpening Line	93
6.5	Experimental Results	95
7	A Novel Broadband Power Generation Technique	101
7.1	Motivation	101
7.2	A variation of Electrical Funnel	102
7.3	Power Amplifier Architecture	105
7.3.1	Driver Design	107
7.4	Implementation	108
7.4.1	Measurement Results	109

7.4.2	Comparison and Conclusion	110
8	Nonlinear Resonance in Two-Dimensional Electrical Lattices	115
8.1	Introduction	115
8.1.1	KP Resonance	119
8.1.2	Resonance in Electrical Lattices	121
8.1.3	Main Results	122
8.2	Numerical Setup	123
8.3	Results of Numerical Experiments	124
8.3.1	Equal amplitude and in-phase.	124
8.3.2	Unequal Amplitude and In-Phase	126
8.3.3	Equal amplitude but out-of-phase	128
8.4	Practical Considerations	129
8.4.1	Double resonance.	129
8.4.2	Non-sinusoidal inputs	129
8.5	Discussion	131
9	Optotronics	135
9.1	Introduction	135
9.2	Methodology and Merits	137
9.3	Historical Remarks	138
9.4	Lattice Equations and PDE Models	140
9.4.1	Kirchhoff's Laws	140
9.4.2	Continuum Limit	140
9.4.3	Range of Validity	141
9.4.4	Dispersive Correction	142
9.4.5	Effect of Boundaries	143
9.5	Refraction	144
9.5.1	Snell's law	144
9.5.2	Thick Parabolic Lens	149
9.5.3	Paraxial Approximation	150

9.5.4	Numerics	151
9.6	Diffraction	154
9.6.1	Kirchhoff	159
9.6.2	Rayleigh-Sommerfeld	162
9.6.3	Huygens-Fresnel	164
9.7	Applications	166
9.7.1	Comments on the Implementation	166
9.7.2	Fourier Transform	167
10	Conclusion	172

List of Figures

2.1	Waves are everywhere: from music instruments to the surface of ocean and from freeways to Mexican wave in stadiums.	7
2.2	a Kelvin-Helmholtz instability rendered visible by clouds in Australia (source: Wikipedia, the online encyclopedia)	8
2.3	The tidal bore in Turnagain inlet (source: Wikipedia, the online encyclopedia)	9
2.4	Soliton on the Scott Russell Aqueduct on the Union Canal (Photograph by K. Paterson)	11
2.5	Nonlinear interaction of two solitary waves in the coast of California (Photograph by author)	12
2.6	The one-dimensional atomic chain model	13
2.7	Two examples of electrical wave propagation media: a a 1D LC ladder and a 2D rectangular LC lattice	17
2.8	A few possible discrete 2D low-pass LC Lattices: each branch is an inductor and at each node, there is a capacitor to the ground.	18
2.9	The lattice can be engineered to achieve desirable transfer function	19
2.10	An accumulation mode MOS varactor with its characteristic	19
3.1	1D artificial transmission line	23
3.2	Voltage V_i versus element number i at $T = 10$ ns for a 1D nonuniform linear transmission line with parameters: $N = 100$, $L_0 = 0.1$ nH, $C_0 = 1$ pF. The input, at the left end of the line ($i = 0$), is a sinusoid with frequency $\alpha = 5$ GHz.	40

3.3	Voltage V_i versus element number i at various times for the (a) uniform NLTL, with $b = 0.5$, $\lambda = 0$, and (b) nonuniform NLTL, with $b = 0.25$, $\lambda = 0.02$. All other parameters are the same as in the linear case. The input frequency is $\alpha = 5$ GHz.	42
3.4	Voltage V_i versus element number i for the 1D nonuniform NLTL, with parameters identical to the previous figure. The outgoing pulse has a larger amplitude and much smaller wavelength than the sinusoidal signal that enters at the left boundary.	43
4.1	2D transmission lattice	45
4.2	Keeping Z_{ij} constant and defining $T_{ij} = n\sqrt{L_{ij}C_{ij}}$ by the above graph results in an electric lens. Keeping T_{ij} constant and defining $Z_{ij} = \sqrt{L_{ij}/C_{ij}}$ by the above graph results in an electric funnel. Note that this is the precise impedance surface used in the 2D numerical simulations that follow.	48
4.3	Voltage V_{ij} as a function of position (i, j) for the 2D nonuniform linear lattice.	58
4.4	Current I_{ij} as a function of position (i, j) for the 2D nonuniform linear lattice, showing the funneling effect: the signal is stronger in the middle.	58
4.5	Power P_{ij} as a function of position (i, j) for the 2D nonuniform linear lattice, demonstrating the funneling effect.	59
4.6	Efficiency as a function of input frequency for the 2D nonuniform linear lattice. Note that for an extremely wide range of input frequencies (0 - 100 GHz), the lattice focuses $\geq 60\%$ of the input power.	59
4.7	Voltage V_{ij} as a function of position (i, j) for the 2D nonuniform non-linear lattice.	62
4.8	Current I_{ij} as a function of position (i, j) for the 2D nonuniform non-linear lattice.	62

4.9	Power P_{ij} as a function of position (i, j) for the 2D nonuniform non-linear lattice, demonstrating both the funneling effect and frequency upconversion.	63
4.10	Power P_{ij} as a function of position (i, j) for the 2D nonuniform nonlinear lattice. This shows the same data as Figure (4.9).	63
5.1	1D nonuniform linear transmission line	64
5.2	Reflection coefficient as a function of the ratio ω/β , for $2\beta l = 1$. Note that for sufficiently low frequencies ω , more than 15% of the input signal is reflected.	75
5.3	Reflection coefficient as a function of ω/β , for $2\beta l = 10^{-6.5}$. Note that the maximum value of the reflection coefficient is less than 10^{-13} so, for all practical purposes, we have 100% transmission of the input signal.	76
5.4	1D nonuniform linear transmission line	77
6.1	Three normalized soliton shapes for different values of L and C (a) $L=1\text{nH}$ and $C=1\text{nF}$ (b) $L=2\text{nH}$ and $C=2\text{nF}$ (c) $L=4\text{nH}$ and $C=4\text{nF}$	82
6.2	Dispersion and non-linear effects in the NLTL	83
6.3	Output waveforms of the normal and gradual soliton line	85
6.4	Schematic of the gradually scaled non-linear transmission line	86
6.5	Schematic of an accumulation mode MOS varactor	87
6.6	Capacitance versus voltage for a MOSVAR	87
6.7	How rise and fall time vary within the NLTL	88
6.8	A proposed NLTL for symmetrical edge sharpening	89
6.9	Simple model of a lossy non-linear transmission line with series resistor	90
6.10	Simple model of a lossy non-linear transmission line with parallel resistor	91
6.11	Measured characteristic of MOSVAR used in the line	92
6.12	Simulated output waveform of the pulse narrowing line using ADS	93
6.13	Simulated input and scaled output waveforms of the edge sharpening line using ADS	94

6.14	Chip micro photograph: the middle line is an edge sharpening line and the other two are pulse narrowing lines.	95
6.15	The frequency response of the oscilloscope	96
6.16	The frequency response of the cables, connectors, and probes	97
6.17	Input and output of pulse narrowing line	98
6.18	Response of the measurement setup to an ideal input	98
6.19	Input and output waveforms of the edge sharpening line	99
6.20	Output waveforms of the edge sharpening line with different amplitude verifying the nonlinear behavior of the line	100
7.1	2D square electrical lattice	103
7.2	Basic idea of a funnel	104
7.3	Simulation results of an ideal funnel with $30\text{pH} \leq L \leq 150\text{pH}$ and $30\text{fF} \leq C \leq 300\text{fF}$	105
7.4	Combiner structure	106
7.5	The architecture of power amplifier	106
7.6	Cascode architecture	107
7.7	Maximum stable power gain of a cascode stage vs. a single transistor .	108
7.8	One stand alone distributed power amplifier	108
7.9	Simulated gain of each distributed amplifier	109
7.10	Chip micro photograph	110
7.11	Measurement setup	111
7.12	The power amplifier chip under test	112
7.13	Measured small signal gain of the amplifier	113
7.14	Measured peak output power of the amplifier	113
7.15	Large signal behavior of the amplifier at 85GHz	114
8.1	2-D Nonlinear Transmission Lattice	115
8.2	1-D Nonlinear Transmission Line	116
8.3	2-D Nonlinear Lattice Block	117

8.4	Right boundary of the 2-D electrical lattice, showing the resistive termination.	124
8.5	Resonance amplitude A_R and efficiency A_R/A as a function of incoming amplitude A , for the case of in-phase, equal amplitude incoming waves, showing (1) the robustness of nonlinear combining ($A_R > 2A$) in all cases; (2) the heightened efficiency for certain input voltages, i.e. two signals of amplitude $A = 0.3V$ combine nonlinearly to produce an $A_R > 6A$ output pulse; and (3) the saturation of output amplitude A_R for high input voltages A	132
8.6	Plot of $V_{ij}(t_0)$ for a particular instant of time $t_0 > 0$, showing the generation of a sharp soliton-like nonlinear pulse. The solution shown is for an 80×80 lattice, assuming left- and bottom-boundary input signals (8.14) with equal amplitudes $A_L = A_B = 0.5$. The capacitor model is given by (8.12) with parameters $b = 0.5$ and $V_M = 1.9$	133
8.7	Resonance amplitude A_R as a function of interaction angle θ , for the case of incoming waves with equal amplitude $0.25V$	133
8.8	Voltage $V_{ij}(t_0)$ (in Volts) and power $P_{ij}(t_0) = V_{ij}(t_0)I_{i+1/2,j}(t_0)$ (in Watts) at a particular instant of time $t_0 > 0$ after three nonlinear interactions have occurred, producing a large nonlinear pulse propagating horizontally to the right.	134
9.1	Two-dimensional lattice of inductors and capacitors (2-D LC lattice) .	135
9.2	Incident, reflected, and transmitted waves in a simple refraction problem	145
9.3	Refraction problem for thick parabolic lens	149

- 9.4 Refraction in a 2-D LC lattice, showing the validity of Snell's law. The black lines show incident and refracted wave vectors predicted by Snell's law. Colors correspond to level sets of the voltage $V_{ij}(t)$, at a particular instant of time $t > 0$. At $t = 0$, voltage forcing is switched on along the left boundary; resulting waves propagate at an angle, towards the interface at $i = 30$, where they are refracted, causing a change in the direction and wavelength of the wave. For $i < 30$, the lattice delay equals τ_1 , while for $i > 30$, the lattice delay equals τ_2 152
- 9.5 Plane slab showing pure transmission and wavelength expansion in the $20 \leq i \leq 70$ section. Colors correspond to level sets of the voltage $V_{ij}(t)$, at a particular instant of time $t > 0$. At $t = 0$, voltage forcing is switched on along the left boundary; resulting waves propagate to the right, towards the interface at $i = 20$, where they are refracted, causing a change in wavelength. At $i = 70$, the wave encounters a second interface and is refracted again, causing the wavelength to return to its original value. The lattice delay equals τ_1 except inside the $20 \leq i \leq 70$ section, where the delay equals τ_2 153
- 9.6 Total internal reflection. Colors correspond to level sets of the voltage $V_{ij}(t)$, at a particular instant of time $t > 0$. At $t = 0$, voltage forcing is switched on along the left boundary at nodes $1 \leq j \leq 20$; resulting waves propagate at a sharp angle towards the interface at $i = 20$, where they undergo total internal reflection and are sent back towards the boundary at $i = 0$. The waves bounce repeatedly off the effective boundaries at $i = 0$ and $i = 20$ as they propagate upwards towards $j = 100$. The lattice delay equals τ_1 for $i < 20$ and equals τ_2 for $i > 20$. In this simulation, unlike the previous two, we used a 100×100 lattice. 155

9.7	Simulation of a uniform 2-D LC lattice showing diffractive effects. The input signal is our choice of forcing function at the left boundary of the lattice, and the output signal is the signal at the right boundary of the lattice. The forcing is sinusoidal and given by (9.25), with $\omega = 60\text{GHz}$. Lattice inductances are $L = 30\text{pH}$ and lattice capacitances are $C = 20\text{fF}$.	156
9.8	Setup for deriving Green's function representation of $U(P_0)$.	157
9.9	Setup for deriving Kirchhoff diffraction integral.	159
9.10	Illumination by point source in Kirchhoff diffraction integral.	161
9.11	Setup for Sommerfeld Green's function	162
9.12	Huygens-Fresnel picture showing illumination on a line several wavelengths away from the thin slit diffraction aperture.	164
9.13	Architecture	167
9.14	Results for two different numerical simulations of the 2-D LC lattice showing how diffraction and lensing effects combine to effectively take the spatial 1-D Fourier transform of the input signal. The plots on the left (input signals) correspond to two different choices of p_j in expression (9.33), with $\omega = 60\text{GHz}$. Lattice parameters are $L = 30\text{pH}$ and $C = 20\text{fF}$, except in a lens-shaped region in the center of the lattice where L is unchanged but $C = 60\text{fF}$. For each input signal, such a lattice was simulated, and the plots on the right show $V_{100,j}(t)$ as a function of vertical section number j , for a particular instant of time $t > 0$.	168
9.15	Numerical simulation of the 2-D LC lattice (in black) as compared with our analytical prediction (in blue) and the true Fourier transform (in green) of the input given by (9.34), with $\omega = 60\text{GHz}$. Lattice parameters are unchanged from Figure 9.14. The black curve shows the numerically computed values of $V_{100,j}(t)$ as a function of vertical section number j , for a particular instant of time $t > 0$.	170
9.16	Sinc input for the 2-D LC lattice, corresponding to Equation (9.35) with $\omega = 60\text{GHz}$. The input $V_{1,j}(t)$ is plotted versus vertical section number j at a fixed instant of time t .	171

9.17 Simulated output $V_{100,j}(t)$ at a fixed instant of time $t > 0$, plotted versus vertical section number j . The input that generated this output is given by Equation (9.35) and Figure 9.16. Lattice parameters are unchanged from Figure 9.14. 171

List of Tables

3.1	Definition of terms	22
7.1	A comparison between this work and other designs	111
8.1	Amplitude A_R of the outgoing resonant pulse that forms from two incoming sinusoids of amplitude A_L and A_B . All amplitudes are in Volts.	127
8.2	Efficiency $A_R/(A_L + A_B)$ (or the ratio of outgoing amplitude to the sum of incoming amplitudes) as a function of A_L and A_B . All amplitudes are in Volts.	127
8.3	Output amplitude A_R (in Volts) and efficiency A_R/A for nonlinear resonance involving two square waves inputs each of amplitude A (in Volts).	130

Chapter 1

Introduction

“The future of integrated electronics is the future of electronics itself. The advantages of integration will bring about a proliferation of electronics, pushing this science into many new areas.” as prophesied G. Moore forty years ago [1]. Today we see the realization of his insight. Not so long ago, a single transistor used to cost a few dollars. Nowadays, for a few dollars we can buy a memory or a microprocessor which has tens of billions transistors on it. It seems that no other field has had such a fast growth.

The continuous development of high performance integrated circuits has led to an explosion in the communication and computation systems. Over the past few years, wireless communication has had an immense growth. Cellular phones are an example of this development. One of the most appealing aspects of wireless networks is that they avoid the high cost of reconfiguring networks: they can be created in just weeks by deploying a small number of base stations, to create high-capacity wireless access systems. They also function well in places where using wires is not an option. The users have the ability to access voice or data while they are mobile, and thousands of subscribers could be connected to a network and share its capacity.

This level of efficiency has broken the boundaries and limits of communication by providing the users easy, unlimited access from any location in the world. Any user could connect to the network -even from the remotest location- and utilize all the available resources. This has made the world a smaller place, removing the barrier in space. According to the U.S. Census Bureau, in 2003, there were 159 million

cell phone subscribers in the US, up from the 34 million users in 1995. More than 25 million households now own laptop computers, and 5.3 million households have wireless Internet access [2].

In this expanding marketplace, integrated circuits technology is chosen based on cost and performance. Technologies such as CMOS, SiGe BiCMOS, InP HBT, GaAs HBT, and GaN HBT can coexist in today's market due to performance and cost tradeoffs. Most microwave and mm-wave (frequencies beyond 30GHz) applications, such as broadband wireless access or vehicular radars, were only within the realm of compound semiconductor devices. The main problem with compound semiconductor technologies is that they are not cost effective. This is due to their inability to reliably integrate different functions (*e.g.*, digital circuits with large number of transistors) on a single chip. However, unlike compound semiconductors, the major advantage of silicon-based technologies is their ever increasing capacity for integration that enables realization of complex circuits at very low cost. Yet silicon has limited performance at high frequency applications, creating a need for other compounds.

Fortunately, the speed of integrated devices improves as their size shrinks. Device scaling has been the main key to success in the semiconductor industry, and it is applicable for all semiconductor processes including silicon. However, there are at least two impediments to scaling; The first limitation is the huge development cost of a new process, and the second problem is technical complications in very small sized devices. For example, decreasing the size of CMOS devices will result in increasing the gate leakage due to decreasing the gate dielectric thickness and subthreshold leakage. This phenomenon increases the idle power of digital gates resulting in the loss of an important advantage of silicon-based technologies. Furthermore, as we reduce transistors sizes, mesoscopic and short channel effects such as hot electron effects, drain induced barrier lowering and mobility degradation transpire. The fundamental limit that we face in scaling the transistors is the gate-dielectric tunneling effect which limits our gate-oxide thickness to a few atoms or approximately 1nm compared to the 3.5nm in production today.

As a solution, we should develop innovative circuit design methodologies capable

of building circuit blocks which operate close to the cut-off frequency of the devices or even beyond it. In other words, as faster processes are continuously being developed, we need to develop novel circuit architectures to enhance high frequencies performance.

1.1 Contributions

In this work, we propose novel circuit topologies inspired by commonly used structures in electromagnetics, and more specifically optics. The proposed methodology is based on nonlinear and/or inhomogeneous one-dimensional (1D) transmission lines which we have successfully extended to two-dimensional transmission lattices. The principles behind these designs stem from the mathematical theory of linear and nonlinear wave propagation. By analyzing the models for the transmission lines/lattices, we are able to exploit the large body of theory to design circuits, demonstrating:

- The narrowest reported pulse on silicon (2.5ps),
- The first in-silicon transmission line system capable of sharpening both rising and falling edges of NRZ data by increasing the bandwidth,
- For a single integrated-circuit silicon-based amplifier, the highest achieved center frequency of operation (85GHz) and the highest achieved power output (120mW) at this frequency,
- Ultra-fast computation systems such as a sub-nanosecond Fourier and Hankel transformers in silicon.

Also we show how the same approach can be applied to realize other structures, leading to a new design discipline we like to call "*Optotronics*".

1.2 Organization

This thesis concentrates on new ways of designing circuits for very high frequency and/or high power applications. Chapter 2 reviews the roots of these design ideas which is the theory of wave propagation in different disciplines. We see that different effects can be studied by wave propagation theory if the natural wavelength is large compared to the microscopic length. Then historical background of soliton pulses is presented. An overview of nonlinear wave propagation in electronics winds up the chapter.

Chapter 3 to 5 cover the theory of wave propagation in one and two dimensional *LC* lattices. they show how to treat the effect of dispersion, nonlinearity, and inhomogeneity. Several analytical solutions as well as numerical results have been presented. The equations that we consider are mostly the model equations for the circuits shown in chapter 6 and chapter 7. The link between these model equations and well-known equations such as KdV and nonlinear Schrödinger equation is studied.

Chapters 6 and chapter 7 introduce the application of these theories. Chapter 6 presents two nonlinear transmission lines. The first one is a soliton line, capable of generating ultra narrow pulses on silicon substrate. Second transmission line can sharpen both rising and falling edges of NRZ data by increasing the bandwidth. The design and measurement of these lines is covered. Chapter 7 shows the application of 2D transmission lattices in broadband power combining. this chapter is wrapped up with simulation and measurement results of a power amplifier fabricated in silicon.

Chapter 8 deals with the interaction of nonlinear waves in *LC* lattices in the regime where both (1) wave amplitude is large compared with wavelength and (2) wavelength is comparable to lattice spacing. Direct numerical simulations show that two plane waves of equal amplitude A incident on the lattice boundary can result in a single outgoing pulse of amplitude $> 6A$, which exceeds the $A + A \rightarrow 4A$ bound in resonance theory for the Kadomtsev-Petviashvili (KP) equation. The KP equation is the weakly nonlinear continuum limit of the lattice equations. This study shows that resonance is robust even in a strongly nonlinear, highly discrete system. The

effects of unequal input amplitudes, out-of-phase input signals, multiple collisions, and non-sinusoidal inputs are considered.

Finally we generalize these techniques in chapter 9. We show, through direct numerical simulations of Kirchhoff's laws, that two-dimensional (2-D) LC lattices support optical phenomena such as refraction and diffraction, which can be applied to design (1) electrical lens and (2) analog Fourier transform circuits. Numerical simulations are validated by analysis of continuum models that effectively capture the behavior of the discrete lattice equations, for signals with frequency content in a certain range. These models consist of, respectively, a two-dimensional Helmholtz equation and a two-dimensional Helmholtz equation with a fourth-order dispersive correction. Solutions of these models are used to derive standard and dispersively corrected versions of Snell's law, as well as diffraction integrals for 2-D waves. Issues related to fabricating such lattices on a standard silicon substrate are discussed.

Chapter 2

Wave Propagation

Waves are everywhere; from the distribution of cars on a highway [3] to the formation of clouds in sky [4], most waves are disturbances that propagate through a medium, often transferring energy. By propagating, waves transfer energy from one point to another, with little or no permanent displacement of the particles of the medium. In other words, relative to the total mass of the medium, there is little or no associated mass transport. Usually waves are oscillations around some fixed positions in a given medium. Figure 2.1 shows few examples of wave phenomenon.

All waves, longitudinal or transverse, electric or elastic, linear or nonlinear, have certain similar behavior in common. The model of wave propagation in a dispersive medium developed by Lord Kelvin, has been successfully used for different types of waves. One can model and explain various phenomena by applying wave propagation theory. As this work focuses more on nonlinear waves and their characteristics, we present the following examples to illustrate this approach. There are excellent references on linear wave phenomena, such as [5][6][7].

2.1 Nonlinear Phenomena

We have all seen propagation of wave in a corn field. Microscopically, this wave is generated since the stalks of the corn move harmonically due to the wind, causing the neighboring ears to interact with each other. Macroscopically, the corn field can be viewed as a dense fluid with waves propagating on its surface due to the flow of



Figure 2.1: Waves are everywhere: from music instruments to the surface of ocean and from freeways to Mexican wave in stadiums.

the air. This is the well-known Kelvin-Helmholtz instability which results from two adjacent shears of fluids traveling with different velocity. Interestingly, this instability is a function of relative velocity of the shears and it is independent of the density of the fluids. A non-zero curvature will lead to a slight centrifugal force which can cause the flow of one fluid around the other. This effect leads to a change in pressure, which amplifies the ripple. The most familiar example of such a behavior is wind blowing over calm water. Tiny dimples in the smooth surface will quickly be amplified to small waves and finally to frothing white-caps. Referring back to the corn field, if the stalk bending is more than a threshold, the stalk will break resulting in a permanent finger print of the wave over the field. One way to control Kelvin-Helmholtz instabilities is to introduce perpendicular periodicities; that means we could save corns by adding periodic trees perpendicular to the direction of the wind [8].

Another example of Kelvin-Helmholtz instability in the nature is the formation of

a class of clouds called Herringbone clouds. Figure 2.2 shows a good example of such clouds before it diffuses.



Figure 2.2: a Kelvin-Helmholtz instability rendered visible by clouds in Australia (source: Wikipedia, the online encyclopedia)

Yet another place that we have experienced nonlinear effects is car traffic. Whitham [3] was first who modeled car traffic using fluid mechanics and explained the effect of traffic lights, condition of the road, and street junctions with the propagation of shock waves. This approach had led to a breakthrough in studying and controlling the car traffic. [9][10][11][12].

A *tidal bore* is a remarkable member of the class of the nonlinear waves. It occurs in shallow rivers with a mild sloping riverbed and a broad funnel shaped estuary. The tide forms a wave that travels up in such a river or narrow bay, against the direction of the current [13][14]. For a tidal bore to be formed, a large tidal range -typically more than six meters between high and low water- is necessary. Because of these conditions, bores occur in relatively few locations worldwide. Figure 2.3 shows an example of this fascinating wave.

The flow of electrons in a solid is easily explained by a Drude (1863-1906) model. In this model, the current density J is related to the electrical field E by $J = (\sigma)E = (ne\mu)E = (ne^2\tau/m)E$ where n is electron density, e is its charge, μ is electron mobility,



Figure 2.3: The tidal bore in Turnagain inlet (source: Wikipedia, the online encyclopedia)

and m is its effective mass to take into account the periodicity of the lattice in which the electrons transfer in. If the above parameters are constant, we will end up with Ohm's law which is a linear relationship between current density and electrical field. However, for large values of electrical field, the electron might be excited to a higher band where the effective mass of the electron may change, due to different relationship between energy and wave number in the new band. For some materials, *e.g.*, GaAs, the effective mass of electron at the new band is larger, resulting in a decrease of J with increasing E . In such a case, the differential resistance is negative and it results in an instability mechanism that leads to propagation of nonlinear stable pulses known as Gunn domains [15]. This phenomenon provide the basic idea for many oscillators [16].

As the last example, let's briefly discuss one of the great discoveries of the last century: morphogenesis (from the Greek *morph* shape and *genesis* creation), which is one of fundamental aspects of developmental biology. Theory of morphogenesis involves an attempt to understand the processes that control the organized spatial distribution of cells during the embryonic development of an organism and which give rise to the characteristic forms of tissues, organs, and overall body anatomy. Some of

the earliest ideas on how physical and mathematical processes and constraints affect biological growth were written by D'Arcy Wentworth Thompson [17] and Alan Turing [18]. They showed that a homogenous mixture of chemicals could lead to periodic time variation in the concentration of a particular chemical or to an inhomogeneous spatial separation of chemicals. Also Turing demonstrated that nonlinear chemical reactions together with diffusion could lead to a spatial separation of the chemicals. Later experiments showed that a homogenous mixture of certain chemicals could result in spatial color pattern. All of these effects can be explained in terms of nonlinear wave propagation in time and space.

Conclusion. The message of these wide range of examples is that we could effectively study different effects by wave propagation theory if the natural wavelength is large compared to the microscopic length.

2.1.1 Soliton

Perhaps soliton is the most famous nonlinear wave. Soliton is a self-reinforcing solitary wave caused by a delicate balance between nonlinear and dispersive effects in the medium. It is not easy to define precisely what a soliton is unless we get into substantial mathematics. Drazin and Johnson [19] describe solitons as solutions of nonlinear differential equations which

1. represent waves of permanent form;
2. are localized, so that they decay or approach a constant at infinity;
3. can interact strongly with other solitons, but they emerge from the collision unchanged apart from a phase shift, so they act somewhat similar to particles.

The concept of a solitary wave was introduced to science by John Scott Russell 170 years ago [20]. In 1834 he observed a wave which was formed when a rapidly drawn boat came to a sudden stop in narrow channel. According to his diary, this wave continued "at great velocity, assuming the form of a large solitary elevation,



Figure 2.4: Soliton on the Scott Russell Aqueduct on the Union Canal (Photograph by K. Paterson)

a well-defined heap of water that continued its course along the channel apparently without change of form or diminution of speed”. He pursued the wave on horseback for more than a mile before returning home to reconstruct it in a water tank. Figure 2.4 shows where he observed soliton and a successful attempt to recreate it. After this discovery, soliton has become important subject of research in diverse fields of physics and engineering. Solitons also occur in other media such as:

- The flow of heat in solids is related to the propagation of solitons. The relationship between soliton amplitude, velocity, and width has been verified. At the microscopic level, usually we deal with phonons. There are number of interesting phenomena that can be explained by this point of view. For example we could study phonon-phonon interaction which is essential for understanding thermal conductivity. Fermi, Ulam, and Pasta [21] numerically showed that phonons don’t come to thermal equilibrium, but rather they have nearly periodic variations. Ten years later Zabusky and Kruskal [22] showed that this is correct and it can be explained in terms of solitons. We will discuss this remarkable discovery in the section 2.2.
- A. S. Davydov [23] has applied similar rules to the transport of energy in protein

chains. He studied chemical changes which leads to the transfer of adenosine triphosphate (ATP) in α -helical protein chains with the idea of soliton propagation. Here the dispersion caused by the resonance interaction of intrapeptide dipole vibrations amide-I and nonlinearity caused by the connection of these vibrations with local displacement of equilibrium positions of peptide groups.

- In 1973, Akira Hasegawa [24] of Bell Labs was the first to suggest that solitons could exist in optical fibers, due to a balance between self-phase modulation [25] and anomalous dispersion [26]. He also proposed the idea of a soliton-based transmission system to increase performance of optical telecommunications.

Regardless of their medium, solitary waves show very intriguing properties, for example in a 2D medium, under certain conditions, two solitons can combine in a nonlinear fashion meaning that they combine to a single outgoing wave with peak amplitude *greater* than the sum of the incoming waves' amplitudes. Figure 2.5 shows an example of this phenomenon on the coast of California.



Figure 2.5: Nonlinear interaction of two solitary waves in the coast of California (Photograph by author)

We will discuss this behavior and other properties of solitons in the following chapters.

2.2 Wave Propagation in Periodic Structures

The first work on wave propagation in periodic structures was that of Newton [27] in his effort to derive a formula for the velocity of sound. He modeled the propagation of sound in the air by propagation of an elastic wave along a lattice of masses and springs. The lattice consists of equispaced equal masses, m , that attract each other with elastic force with constant e as shown in figure 2.6.

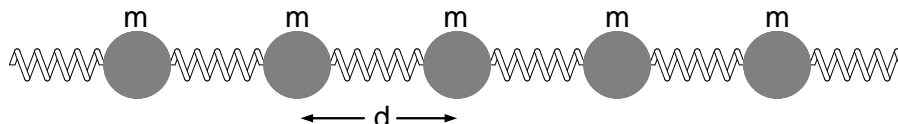


Figure 2.6: The one-dimensional atomic chain model

He obtained a closed form expression for the velocity of sound:

$$V = d\sqrt{\frac{e}{m}} = \sqrt{\frac{ed}{\rho}} \quad (2.1)$$

where d is the spacing of masses and ρ is density. To verify this model, he used the density of air and isothermal bulk modulus of air as ed . This computed result was smaller than experimental value and hence the model did not match with reality. In 1822 Laplace noticed that expansions and condensations associated with sound waves occur adiabatically and hence adiabatic elastic constant should be used instead of the isothermal value. With this correction the model matched experiments. After this initial work, number of scientists have looked into various kinds of wave propagation in periodic structures. For a complete historical background see [33].

2.2.1 Fermi-Pasta-Ulam Experiment: Birth of Soliton

Among different problems in this category, heat-transfer probably concerns us the most. Fermi, Ulam, and Pasta [21] studied the flow of incoherent thermal energy in a solid by modeling it by a 1-D lattice consisting of equal masses connected with nonlinear elasticity (similar to Figure 2.6 but with nonlinear springs).

For small displacements, the interactions among particles are harmonic and therefore the equations of motion of particles can be decoupled and the dynamics of the lattice can be described by superposition of mutually independent *normal modes*. Because these normal modes are independent, if a normal mode is excited, its energy is not transferred to other modes. As a result, a lattice with harmonic oscillations is called *nonergodic*: it never reaches the thermal equilibrium.

What would happen if we add nonlinearity to the equation? Debye [28] and Peierls [29] suggested that in this case, the normal modes will interact and the energy transfers from one mode to others. Consequently, after many iterations, the system would exhibit 'thermalization' that is an *ergodic* behavior in which the influence of the initial modes of vibration fades in importance and the system becomes random, with all modes excited almost equally. In 1955, Fermi, Pasta, Ulam attempted to verify this assumption with one of the first dynamics calculations performed on a computer. They assumed a quadratic nonlinearity and surprisingly they realized that the system does not approach energy equilibrium, that is, the energy in one mode does not spread to the rest. Instead the energy almost periodically returned to the original mode.

This recurrence phenomenon, known as FPU problem, suggests that the system is almost completely integrable. Ten years later, Zabusky and Kruskal [22] showed that, for the FPU problem with a cubic nonlinearity, the Korteweg-de Vries (KdV) equation [30] (discovered in 1895 by D. J. Korteweg and G. de Vries to model water waves in a shallow canal) represents a good approximation to the actual equations of motion of the system. They also observed the asymptotic breakdown of the solution of the KdV equation into a train of solitons, whose particle-like behavior allowed them to interpret the FPU recurrence as a Poincaré recurrence of the initial state: A sinusoidal initial condition launched to the system evolves to multiple solitons which travel with different velocities. These solitons collide but they emerge from the collision unchanged apart from a phase shift. At some point in time, there is an instant when the solitons collide at the same point and hence the initial condition comes close to recurrence. The exact recurrence is not possible due to small phase

shifts associated with soliton collisions.

In 1967 Gardner [31] showed that if the initial condition is localized, we can find the analytical solution of the KdV equation through *inverse scattering method*. One year later, Miura [32] developed a method of generating an infinite sequence of constants of motion associated with the KdV equation. This was another explanation of why solitons have their structural stability.

At the end of this section, let us note that the classical work of Brillouin [33] on crystal lattices makes explicit the analogy between crystal lattices, mass-spring models, and LC lattices in one, two, and three spatial dimensions. Brillouin's primary focus in this work was the development of band-gap theories for lattices with periodic inhomogeneities.

2.3 Nonlinear Waves in Electronics

2.3.1 Motivation

Recently, there has been growing interest in using silicon-based integrated circuits for broadband, high frequency applications. The high level of integration offered by silicon enables numerous new topologies and architectures for low-cost reliable SoC applications at microwave and millimeter wave bands, such as broadband wireless access (*e.g.*, WiMax), vehicular radars at 24GHz and 77GHz citePfeiffer, short range communications at 24GHz and 60GHz, and ultra narrow pulse generation for UWB radar.

If we attempt to build these high frequency broadband circuits with transistors, we are limited by the highest possible transistor cut-off frequency f_T , the maximum efficiency of the transistor, and also its breakdown voltage. These same considerations hold for the wider class of active devices. Even if we restrict consideration to silicon-based technologies, active devices are technology-dependent, making it difficult to port the design from one CMOS technology to another. Therefore, active device solutions to the signal generation/processing problem will be limited in both

functionality and portability. Also, existing high frequency circuits typically use either tuned circuits (*e.g.*, LC tank) or microwave techniques (*e.g.*, transmission lines as impedance transformers). These approaches are inherently narrow band and cannot be used in applications such as ultra wide-band impulse radio and ultra wide-band radar (*e.g.*, ground penetrating radar), pulse sharpening, jitter reduction, or a wide band power amplifier.

The theory of wave propagation in linear and nonlinear media is an attractive candidate to face these challenges. For example the ability of solitons to propagate with small dispersion can be used as an effective means to transmit data, modulated as short pulses over long distances; one example of this is the ultra wide band impulse radio that has gained popularity [34].

Furthermore, another advantage of using electrical medium as the wave propagation medium is that it could provide a great platform to demonstrate and verify mathematical and physical theories. For example, a two dimensional *LC* lattice, shown in the next section, is a perfect medium to observe nonlinear wave propagation phenomena such as formation of solitons, kinks, Kelvin-Helmholtz instability, and nonlinear Schrödinger equation. It is also possible to develop new phenomena in electrical circuits which have many applications such as power combining and ultra fast specialized computations.

2.3.2 Electrical Wave Propagation Medium

An electrical wave propagation medium could be formed by connecting inductors and capacitors. Figure 2.7 shows two examples of these medium: a 1D LC ladder and a 2D LC lattice. Of course, these are not the only possible configurations for LC lattices: We could build high-pass, band-pass, and low-pass structures, triangular, rectangular, and hexagonal lattices, add resistors or active devices to the lattice, and add nonlinear elements. These structures can support wave propagation in certain frequency ranges. For example, Figure 2.8 shows three low-pass electrical lattice with their cut-off frequency, ω_c , that is the maximum frequency that can travel inside the

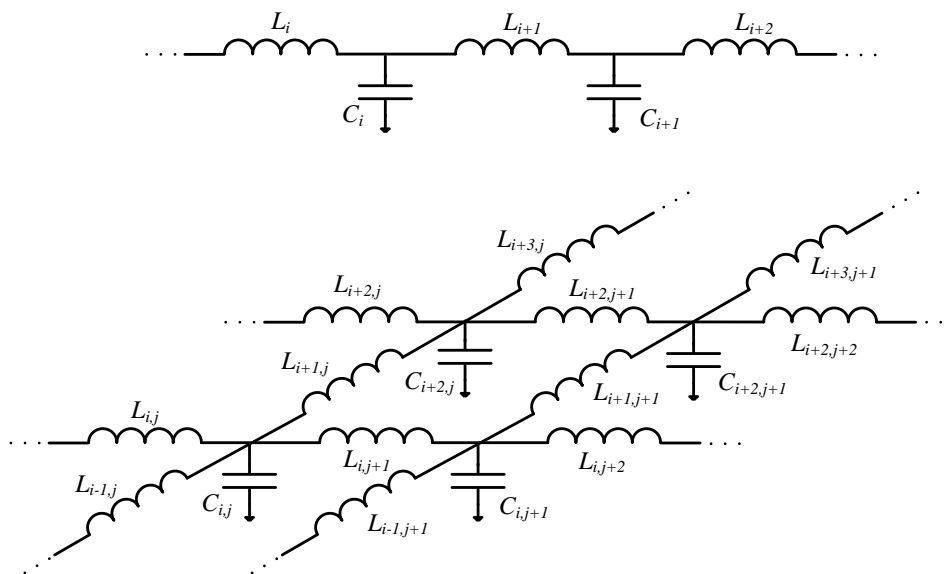


Figure 2.7: Two examples of electrical wave propagation media: a 1D LC ladder and a 2D rectangular LC lattice

lattice. For details on how to compute this frequency please see Chapters 4 and 8. It is noteworthy that with today's state of the art integrated circuit technologies, on a silicon substrate, if we use micro strip lines, as inductors and metal to metal capacitance as capacitors, the minimum possible inductance and capacitance are, approximately, $L_M = 30$ pH and $C_M = 5$ fF. Below these values, the parasitic inductance and capacitance would be dominant. Using these values, we find that the maximum frequency for plane wave propagation on a 2-D rectangular silicon transmission lattice is $f_M \approx 1.16$ THz which is much higher than the cut-off frequency of actives in the same process.

Generally, these lattices can be inhomogeneous where the values of inductors and capacitors vary in space. When the inductors and capacitors do not change too abruptly, it is possible to define local parameters such as characteristic impedance, propagation delay, at each node as a function of the location of that node. Defining local impedance and velocity as functions of location, allows us to engineer the lattice to achieve the desired propagation and reflection properties. In general, we might change one of the lattice parameters such as impedance, velocity, inductance, capac-

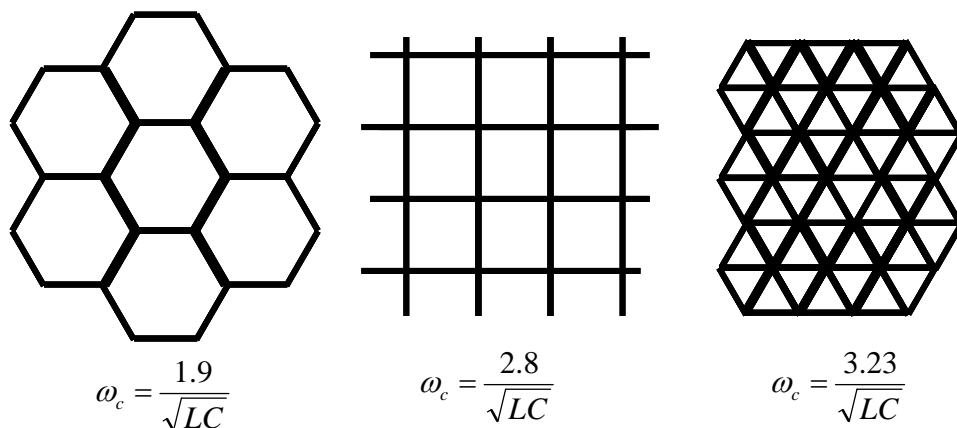


Figure 2.8: A few possible discrete 2D low-pass LC Lattices: each branch is an inductor and at each node, there is a capacitor to the ground.

itance, or even the termination of different nodes in order to get the desired transfer function. Figure 2.9 shows an example of this idea where input signal is applied to the left boundary and the output signal is taken from the right boundary.

So a transmission surface could be used to process the input signal. This is potentially a very fast computation technique and is very similar to changing ε and μ of a medium to change the propagation of an EM wave, or the case of quantum mechanics where changing potential barrier could result in desired scattering parameters.

2.3.2.1 Sources of Nonlinearity

The nonlinear elements could be added to the electrical lattice in order to form electrical nonlinear wave propagation media. The nonlinear elements could be voltage dependant capacitors or current dependant inductors. In this work, we mainly focus on nonlinear capacitors, since it is not easy to fabricate nonlinear inductors in today's integrated processes.

An accumulation mode MOS varactor [35] is an example of the voltage dependant capacitance. Figure 2.10 shows the structure and characteristic of this device. The structure is very similar to an nMOS transistor but it has $n+$ source and drain inside an n-tub instead of a p-tub. As gate voltage increases more electron accumulates under the gate, reducing the effective spacing between capacitor plates. The secondary

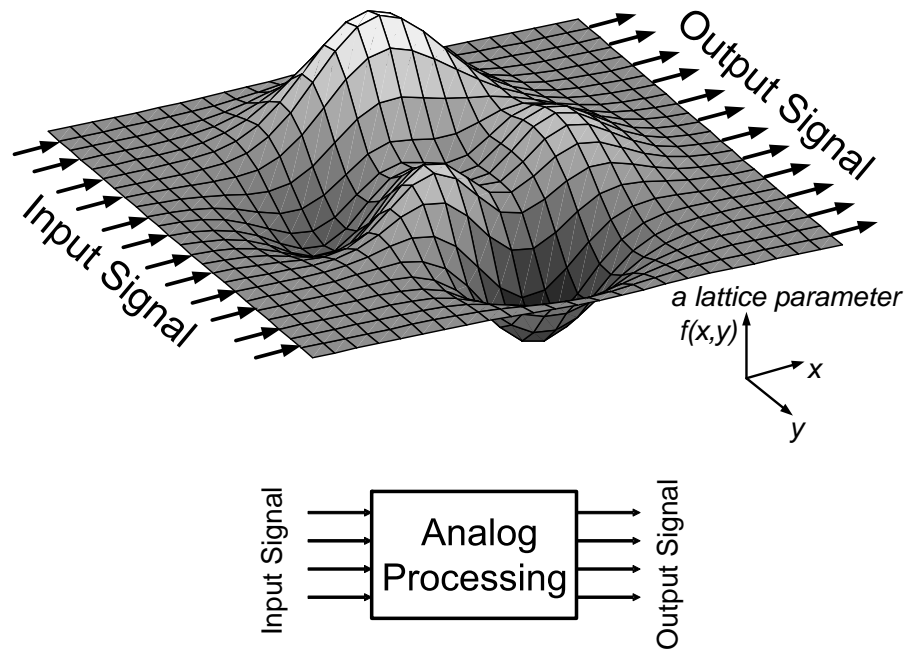


Figure 2.9: The lattice can be engineered to achieve desirable transfer function reduction in capacitance is due to poly-silicon depletion [36][37] and short-channel charge quantization [37] effects.

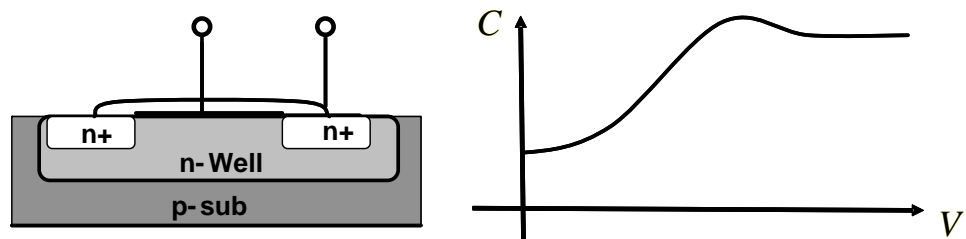


Figure 2.10: An accumulation mode MOS varactor with its characteristic

2.3.3 Historical Remarks

Compared to other disciplines like optics or plasma physics there has not been lots of work on nonlinear wave propagation in electrical domain.

It has been known [38][39][40][4] since the 1960s that the presence of voltage-dependent capacitors in these one-dimensional structures leads to nonlinear wave

phenomena. Scott's classical treatise [4] was among the first to treat the physics of transmission lines. Scott showed that the Korteweg-de Vries (KdV) equation describes weakly nonlinear waves in the 1D uniform nonlinear transmission line (NLTL). Later, Nejoh showed that if the nonlinearity is moved from the capacitor parallel to the shunt branch of the line to a capacitor parallel to the series branch, the nonlinear Schrödinger (NLS) equation is obtained instead [41].

In 1982, model equations for 1D lines that combine nonuniformity, nonlinearity, and resistive loss have been derived by Pantano [42]. In his work, he showed the Burgers- and KdV-type equations govern propagation of waves in NLTL. He also found solitons with varying characteristics. This was a great step toward modeling the NLTL, but more analytical and numerical results were necessary. In other work by Ikezi, numerics and experiments [43] indicated that a nonuniform NLTL could be used for "temporal contraction" of pulses. Later, Rodwell [44] used nonlinear capacitors on a GaAs substrate to generate picosecond pulses. He also used NLTL to form shock waves with very fast rising edge.

Also, 1D nonlinear transmission lines have been studied by various groups [45] [46] [43] [47] [48] with a focus on generation of ultrashort, high-power, stable electrical pulses. Finally, Ballantyne [49] used a uniform NLTL and a feedback loop to make a baseband soliton oscillator in electrical domain.

Because of lack of application and higher level of complexity, two dimensional nonlinear LC lattices have received much less attention. Recently, Dinkel [50], assumed a uniform, nonlinear 2D lattice and showed that the Kadomtsev-Petviashvili (KP) equation [51] describes weakly nonlinear wave propagation in such lattices.

At the other end of the spectrum, nonuniform linear transmission lines have been extensively used by the microwave community for impedance-matching and filtering. In fact, the idea of a nonuniform linear transmission line goes back to the work of Heaviside in the nineteenth century—see Kaufman's bibliography [52] for details.

It seems that more analysis and physical interpretation in this area is needed, specially for two dimensional structures that promise new applications. Theory of wave propagation in one- and two-dimensional transmission lattices with the aim of

clarifying the effects of discreteness, nonuniformity, and nonlinearity is necessary. By finding the links between wave propagation in electrical structures and other media such as fluids or plasma, we could exploit the theory of wave propagation and find new applications for NLTLs. In the following chapters, we will discuss the theory of 1D and 2D transmission media and then demonstrate various applications for them, and compare their performance with classical approaches.

Chapter 3

Theory of One-Dimensional Transmission Line

Before proceeding to the theory of wave propagation in 1D transmission line, we make a few definitions, in table 3.1 that will help categorize the transmission lines under consideration.

In this work, We review one-dimensional transmission line theory with the aim of clarifying the effects of discreteness, nonuniformity, and nonlinearity. Continuum equations that accurately model these effects are derived. The speed and amplitude of outgoing signals are analyzed directly from the continuum model. We show numerically that introducing weak nonlinearity causes outgoing pulses to assume a soliton-like shape. In the present work, we do not consider current-dependent inductors because of implementation issues.

Definitions:	
<i>Linear</i>	Capacitors and inductors are constant with respect to changes in voltage.
<i>Nonlinear</i>	Capacitors are voltage-dependent and/or inductors are current-dependent.
<i>Uniform</i>	Identical capacitors and inductors are used throughout the line.
<i>Nonuniform</i>	Different capacitors and inductors are used in different parts of the line.

Table 3.1: Definition of terms

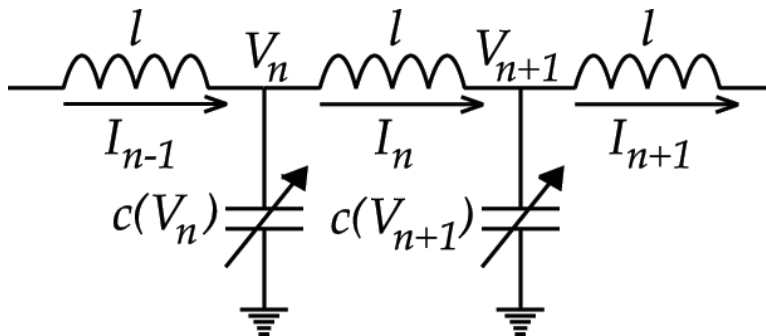


Figure 3.1: 1D artificial transmission line

3.1 Uniform Nonlinear 1D Transmission Lines

In this section, we review a few facts about uniform NLTLs and their use for *pulse narrowing* (Figure 3.1). The nonlinear transmission line we consider, consists of series inductors and nonlinear (voltage dependant) shunt capacitors. At node n in the transmission line, Kirchoff's laws yield the following coupled system of ODEs:

$$V_n - V_{n+1} = \frac{d\phi_{n+1/2}}{dt} \quad (3.1a)$$

$$I_{n-1/2} - I_{n+1/2} = \frac{dQ_n}{dt}. \quad (3.1b)$$

Here $\phi_{n+1/2} = \ell I_{n+1/2}$ is the magnetic flux through the inductor that is between nodes n and $n+1$, and $dQ_n = c(V_n)dV_n$ is the charge on the varactor at node n . Using this, (3.1) can be rewritten and combined into

$$\ell \frac{d}{dt} \left[c(V_n) \frac{dV_n}{dt} \right] = V_{n+1} - 2V_n + V_{n-1}. \quad (3.2)$$

Starting from this semi-discrete model, we develop a continuum model in the standard way. Write x_n as the position of node n along the line; assume that the nodes are equispaced and that $h = x_{n+1} - x_n$ is small. Then, define $V(x, t)$ such that $V(x_n, t) = V_n(t)$. This means that $V_{n+1} = V(x_{n+1}) = V(x_n + h)$. We Taylor expand to fourth-order in h and find that (3.2) is equivalent to

$$\ell \frac{\partial}{\partial t} \left[c(V) \frac{\partial V}{\partial t} \right] = h^2 \frac{\partial^2 V}{\partial x^2} + \frac{h^4}{12} \frac{\partial^4 V}{\partial x^4}. \quad (3.3)$$

Let $L = \ell/h$ and $C(V) = c(V)/h$ be, respectively, the inductance and capacitance per unit length. Then (3.3) becomes

$$L \frac{\partial}{\partial t} \left[C(V) \frac{\partial V}{\partial t} \right] = \frac{\partial^2 V}{\partial x^2} + \frac{h^2}{12} \frac{\partial^4 V}{\partial x^4}. \quad (3.4)$$

We regard this as a continuum model of the transmission line that retains the effect of discreteness in the fourth-order term.

3.1.1 Discreteness Generates Dispersion

Considering small sinusoidal perturbations about a constant voltage V_0 , we compute the dispersion relation* for (3.4):

$$\omega(k) = kv \sqrt{1 - \frac{h^2}{12} k^2}, \quad (3.5)$$

where $v = 1/\sqrt{LC(V_0)}$. We see that for $h > 0$, $\omega(k)$ depends nonlinearly on k . Wavetrains at different frequencies move at different speeds.

In the applied mathematics/physics literature, one finds authors introducing dispersion into transmission lines through the use of shunt-arm capacitors [41]. This is unnecessary. Experiments on transmission lines we have described, without shunt-

*Here L and C are distributed parameters with units of, respectively, inductance per unit length and capacitance per unit length—this implies that v has units of velocity. Meanwhile, k has units of inverse length here, so the quantity hk is dimensionless, consistent with the $h \rightarrow 0$ limit of the dispersion relation that we describe later.

arm capacitors, reveal that dispersive spreading of wavetrains due to the discrete nature of the line is a commonly observed phenomenon. Accurate continuum models of the transmission line we have considered should include this discreteness-induced dispersion. Therefore, we use information about the $h = 0$ case only if it leads to mathematical insights about the $h > 0$ case, which is what truly concerns us.

3.1.2 Traveling Wave Solutions

Retaining h as a small but non-zero parameter, we search for traveling-wave solutions of (3.4), of the form $V(x, t) = f(u)$ where $u = x - \nu t$. Using this ansatz and the varactor model $C(V) = C_0(1 - bV)$, we obtain the following ODE:

$$(\nu^2 - \nu_0^2)f'' = \frac{h^2\nu_0^2}{12}f^{(4)} + \frac{b\nu^2}{2}(f^2)'' , \quad (3.6)$$

where $\nu_0^{-2} = LC_0$ and primes denote differentiation with respect to u . Now integrating twice with respect to u , we obtain

$$(\nu^2 - \nu_0^2)f = \frac{h^2\nu_0^2}{12}f'' + \frac{b\nu^2}{2}f^2 + \tilde{A}u + \tilde{B}. \quad (3.7)$$

We search for a localized solution, for which $f, f', f'' \rightarrow 0$ as $u \rightarrow \pm\infty$. This forces the constants to be zero: $\tilde{A} = \tilde{B} = 0$. Now multiplying (3.7) by $2f'$, integrating with respect to u , and again setting the constant to zero:

$$(f')^2 = Af^2 - Bf^3, \quad (3.8)$$

where

$$A = \frac{12(\nu^2 - \nu_0^2)}{h^2\nu_0^2} \quad \text{and} \quad B = \frac{4b\nu^2}{h^2\nu_0^2}.$$

The first-order ODE (3.8) can be integrated exactly. Taking the integration constant to be zero, we obtain the single-pulse solution

$$V(x, t) = \frac{3(\nu^2 - \nu_0^2)}{b\nu^2} \operatorname{sech}^2 \left[\frac{\sqrt{3(\nu^2 - \nu_0^2)}}{\nu_0 h} (x - \nu t) \right]. \quad (3.9)$$

The sech^2 form of this pulse is the same as for the soliton solution of the Korteweg-de Vries (KdV) equation. Indeed, applying the reductive perturbation method to (3.4), we obtain KdV in the unidirectional, small-amplitude limit.

3.1.3 Reduction to KdV

Starting with (3.4) and again modeling the varactors by $C(V) = C_0(1-bV)$, introduce a small parameter $\varepsilon \ll 1$ and change variables via

$$s = \varepsilon^{1/2}(x - \nu_0 t), \quad T = \varepsilon^{3/2}t, \quad (3.10)$$

with $\nu_0^{-2} = LC_0$. Writing

$$V(x, t) = V(\varepsilon^{-1/2}s + \nu_0\varepsilon^{-3/2}T, \varepsilon^{-3/2}T),$$

we find that

$$\frac{\partial}{\partial x} = \varepsilon^{1/2} \frac{\partial}{\partial s} \quad \text{and} \quad \frac{\partial}{\partial t} = \varepsilon^{3/2} \frac{\partial}{\partial T} - \varepsilon^{1/2} \nu_0 \frac{\partial}{\partial s}. \quad (3.11)$$

Using the formula for $C(V)$, we rewrite the left-hand side of (3.4):

$$LC_0 \frac{\partial}{\partial t} \left[(1 - bV) \frac{\partial V}{\partial t} \right] = \nu_0^{-2} \frac{\partial^2}{\partial T^2} \left(V - \frac{b}{2} V^2 \right).$$

Using this and (3.11), we rewrite (3.4) in terms of the long space and time variables s and T :

$$\nu_0^{-2} \left(\varepsilon^3 \frac{\partial^2}{\partial T^2} - 2\varepsilon^2 \nu_0 \frac{\partial^2}{\partial T \partial s} + \varepsilon \nu_0^2 \frac{\partial^2}{\partial s^2} \right) \left(V - \frac{b}{2} V^2 \right) = \varepsilon \frac{\partial^2 V}{\partial s^2} + \frac{h^2}{12} \varepsilon^2 \frac{\partial^4 V}{\partial s^4} \quad (3.12)$$

Now introducing the formal expansion

$$V = \varepsilon V_1 + \varepsilon^2 V_2 + \dots, \quad (3.13)$$

the order ε^2 terms in (3.12) cancel. Keeping terms to lowest order, ε^3 , we find

$$\nu_0 \frac{\partial^2 V_1}{\partial s \partial T} + \frac{b\nu_0^2}{4} \frac{\partial^2 V_1^2}{\partial s^2} + \frac{\nu_0^2 h^2}{24} \frac{\partial^4 V_1}{\partial s^4} = 0, \quad (3.14)$$

In what follows, we abuse notation by using V to denote V_1 . Integrating (3.14) with respect to s yields the KdV equation:

$$\frac{\partial V}{\partial T} + \frac{b\nu_0}{2} V \frac{\partial V}{\partial s} + \frac{\nu_0 h^2}{24} \frac{\partial^3 V}{\partial s^3} = 0. \quad (3.15)$$

The KdV equation has been investigated thoroughly and many of its properties are well-known, including solution by inverse scattering, complete integrability, and geometric structure [8]. Hence we will not pursue these topics here.

3.1.4 Remark 1: Zero-Dispersion Case

If we had a purely continuous transmission line, we would take the $h \rightarrow 0$ limit of (3.4) and obtain

$$L \frac{\partial}{\partial t} \left[C(V) \frac{\partial V}{\partial t} \right] = \frac{\partial^2 V}{\partial x^2}. \quad (3.16)$$

This equation, which in general yields discontinuous shock solutions, has been studied before [58] and we will not repeat the general analysis. However, note that if we carry out the reductive perturbation method on (3.16), we end up with the $h \rightarrow 0$ limit of (3.15), which is the inviscid Burgers equation:

$$\frac{\partial V}{\partial T} + \frac{bc_0}{2} V \frac{\partial V}{\partial s} = 0. \quad (3.17)$$

It is well-known [59] that for any choice of initial condition $V(x, 0)$, no matter how smooth, the solution $V(x, t)$ of (3.17) develops discontinuities (shock waves) in finite time. Meanwhile, for large classes of initial data, the KdV equation (3.15) possesses solutions that stay smooth globally in space and time [60].

What is intriguing is this: suppose we keep h as an arbitrary, non-zero parameter and solve (3.15) analytically, using the inverse scattering method. We obtain a

function $u^h(x, t)$. In the work of Lax and Levermore[61], it was shown that in the zero-dispersion $h \rightarrow 0$ limit, the sequence $u^h(x, t)$ does *not* converge to a solution of Burgers' equation (3.17). Therefore, we conclude that the $h > 0$ continuum model allows fundamentally different phenomena than the $h = 0$ model. In the nonlinear regime, we must keep track of discreteness.

3.1.5 Remark 2: Linear Case

Note that if $C(V) = C$ is constant, we arrive at the linear, dispersive wave equation

$$\frac{\partial^2 V}{\partial t^2} - \frac{1}{LC} \frac{\partial^2 V}{\partial x^2} = \frac{h^2}{12} \frac{\partial^4 V}{\partial x^4}. \quad (3.18)$$

This equation can be solved exactly using Fourier transforms. In fact, we will carry out this procedure for a similar equation in the following section.

3.1.6 Frequency Response

So far we have discussed special solutions of (3.4) and the KdV equation. Our primary concern is the transmission lines for the mixing of EWB signals. The physical setup requires that an incoming signal enter the transmission line at, say, its left boundary. The signal is transformed in a particular way and exits the line at, say, its right boundary.

Various authors have examined the initial-value problem for the KdV equation. It is found that, as $t \rightarrow \infty$, the solution of the KdV equation consists of a system of interacting solitons. Therefore, we expect that incoming sinusoidal signals will be reshaped into a series of soliton-like pulses. Suppose we wish to determine the precise frequency response in the nonlinear regime: given an input sinusoid of frequency α , we expect to see solitons of frequency $F(\alpha)$ at the output end of the line. We will address the problem of quantitatively determining $F(\alpha)$ in future work.

For now, we mention that a comprehensive mathematical analysis of the *quarter-*

plane problem

$$u_t + uu_x + u_{xxx} = 0 \tag{3.19a}$$

$$u(x, 0^+) = 0 \tag{3.19b}$$

$$u(0, t) = g(t) \tag{3.19c}$$

for the KdV equation is not possible at this time. This includes the frequency response problem for which $g(t) = A \sin \alpha t$. Inverse scattering methods applied to (3.19) yield information only in the simplest of cases, i.e. when $g(t)$ is a constant[62]. The problem is that in order to close the evolution equations for the scattering data associated with (3.19), one needs to postulate some functional form for $u_x(0, t)$ and $u_{xx}(0, t)$. It does not appear possible to say *a priori* what these functions should be.

One approach[63] is to postulate that these functions vanish identically for all t . They obtain approximate closed-form solutions in the case where $g(t)$ is a single square-wave pulse, with $g(t) \equiv 0$ for $t > T$. In future work, we will investigate whether this is possible if $g(t)$ is a sinusoidal pulse.

In this work, we attempt an analytical solution of the frequency response problem only in the *linear* regime. For the *nonlinear* regime, we discuss special solutions and the solution of the initial-value problem for the underlying model equations, to gain a qualitative understanding of the models. For quantitative information about the general nonlinear, nonuniform frequency response problem, we use direct numerical simulations of the semidiscrete model equations.

3.2 Nonuniform Linear 1D

In this section, models for nonuniform transmission lines will be derived and their dynamics will be discussed. We study the one-dimensional case because they can be solved exactly; these solutions will be used in our analysis of the two-dimensional case. By nonuniform, we mean that the inductance $L(x)$ and capacitance $C(x)$ varies

as a function of position:

$$\frac{\partial L}{\partial x} \neq 0, \quad \frac{\partial C}{\partial x} \neq 0.$$

3.2.1 Linear case

For now, assume that the line is linear:

$$\frac{\partial L}{\partial I} = 0, \quad \frac{\partial C}{\partial V} = 0.$$

Then, modifying (3.1), we obtain the exact, semi-discrete model

$$V_n - V_{n+1} = \ell_{n+1/2} \frac{dI_{n+1/2}}{dt} \quad (3.20a)$$

$$I_{n-1/2} - I_{n+1/2} = c_n \frac{dV_n}{dt}, \quad (3.20b)$$

which can be combined into the single second-order equation

$$\ell_{n+1/2}(V_{n-1} - V_n) - \ell_{n-1/2}(V_n - V_{n+1}) = c_n \ell_{n-1/2} \ell_{n+1/2} \frac{d^2 V_n}{dt^2}. \quad (3.21)$$

Let $L(x)$ and $C(x)$ be, respectively, the inductance and capacitance per unit length at the position x along the transmission line. This yields the relations $L(x) = \ell_n/h$ and $C(x) = c_n/h$, and allows us to expand

$$\begin{aligned} \ell_{n+1/2} &= hL(x + h/2) = h \left(L + \frac{h}{2} \frac{dL}{dx} + \frac{h^2}{8} \frac{d^2L}{dx^2} + \frac{h^3}{48} \frac{d^3L}{dx^3} + O(h^4) \right) \\ \ell_{n-1/2} &= hL(x - h/2) = h \left(L - \frac{h}{2} \frac{dL}{dx} + \frac{h^2}{8} \frac{d^2L}{dx^2} - \frac{h^3}{48} \frac{d^3L}{dx^3} + O(h^4) \right). \end{aligned}$$

Expanding V as before, we retain terms up to fifth-order in h on both sides:

$$\begin{aligned} h^3(LV_{xx} - V_x L_x) + h^5 \left(\frac{1}{12} LV_{xxxx} + \frac{1}{8} L_{xx} V_{xx} - \frac{1}{6} L_x V_{xxx} - \frac{1}{24} L_{xxx} V_x \right) \\ = h^3 C \left(L^2 - \frac{h^2}{4} (L_x)^2 \right) V_{tt}, \quad (3.22) \end{aligned}$$

where we have used subscripts to denote differentiation. We now assume that L varies slowly as a function of space, so that $L \gg hL_x$. Hence our continuum model is:

$$V_{xx} - LCV_{tt} = V_x \frac{L_x}{L} - h^2 \left(\frac{1}{12} V_{xxxx} - \frac{1}{6} \frac{L_x}{L} V_{xxx} \right). \quad (3.23)$$

To be clear, we specify that $L : [0, \infty) \rightarrow \mathbb{R}$ and $C : [0, \infty) \rightarrow \mathbb{R}$ are smooth and positive. The parameter h is a measure of discreteness, which as discussed above, contributes dispersion to the line.

3.2.2 Physical Scenario

We are interested in solving the following *signaling problem*: the transmission line is dead (no voltage, no current) at $t = 0$, at which point a sinusoidal voltage source is switched on at the left boundary. We assume that the transmission line is long, and that it is terminated at its (physical) right boundary in such a way that the reflection coefficient there is very small. This assumption means that we may model the transmission line as being semi-infinite.

We formalize this as an initial-boundary-value problem (IBVP). Given a transmission line on the half-open interval $[0, \infty)$, we seek a function $V(x, t) : [0, \infty) \times [0, \infty) \rightarrow \mathbb{R}$ that solves

$$LCV_{tt} = V_{xx} + \frac{h^2}{12} V_{xxxx} - \frac{L_x}{L} \left(V_x + \frac{h^2}{6} V_{xxx} \right) \quad (3.24a)$$

$$V(x, 0) = 0 \quad (3.24b)$$

$$V_t(x, 0) = 0 \quad (3.24c)$$

$$V(0, t) = A \sin \alpha t \quad (3.24d)$$

$$V_x(0, t) = 0 \quad (3.24e)$$

where A, α are arbitrary constants, while λ must be positive.

3.2.3 Non-Dimensionalization

Examining the form of problem (3.24), we expect that when $L_x = 0$ (the uniform case), it may be possible to find exact traveling wave solutions. Hence we exploit the linearity of (3.24a) and seek solutions when L is a slowly varying function of x .

In order to carry this out, we must first non-dimensionalize the continuum model (3.23). Suppose that the transmission line consists of N sections, each of length h . This gives a total length $d = Nh$. Next, suppose that we are interested in the dynamics of (3.24) on the time scale T . Using the constants d and T , we introduce the rescaled, dimensionless length and time variables

$$x' = \frac{x}{d} \quad \text{and} \quad t' = \frac{t}{T}. \quad (3.25)$$

We then non-dimensionalize (3.23) by writing it in terms of the variables (3.25):

$$\frac{LCd^2}{T^2} V_{t't'} = V_{x'x'} + \frac{1}{12N^2} V_{x'x'x'x'} - \frac{L_{x'}}{L} (V_{x'} + \frac{1}{6N^2} V_{x'x'x'}). \quad (3.26)$$

For the purposes of notational convenience, we omit primes from now on.

3.2.4 Exponential Tapering

The general nonuniform problem, with arbitrary L and C , may not be classically solvable in closed-form. Here we consider the exponentially tapering given by

$$L(x) = Be^{\lambda x} \quad (3.27a)$$

$$C(x) = \frac{1}{B\nu_0^2} e^{-\lambda x} \quad (3.27b)$$

where ν_0, λ, B are positive constants. In our discussion of 2D transmission lattices, we will see that a generalization of this tapering solves certain EWB signal-shaping problems. Using (3.27), the non-dimensionalized 1D equation (3.26) simplifies con-

siderably to

$$\frac{\nu_0^{-2}d^2}{T^2}V_{tt} = V_{xx} + \frac{1}{12N^2}V_{xxxx} - \lambda \left(V_x + \frac{1}{6N^2}V_{xxx} \right). \quad (3.28)$$

We will analyze this equation subject to the previously discussed initial/boundary conditions (3.24b-3.24e).

3.2.5 Perturbative Solution

We will find solutions of (3.28) accurate to first order in λ . Let us begin by solving the $\lambda = 0$ case. Note that the case $\lambda = 0$ arose in our discussion of the uniform problem (see (3.18)).

From the setup of the problem, it is clear that the solution will consist of a wavetrain moving to the right at some finite speed. Hence we try the ansatz

$$V(x, t) = \begin{cases} f(kx - \omega t) & x < \frac{\omega}{k}t \\ 0 & x \geq \frac{\omega}{k}t \end{cases} \quad (3.29)$$

Substituting this into (3.28) gives

$$\frac{\nu_0^{-2}d^2}{T^2}\omega^2 f''(z) = k^2 f''(z) + \frac{1}{12N^2}k^4 f^{(4)}(z),$$

where $z = kx - \omega t$. Integrating twice with respect to z and setting integration constants to zero gives a second-order ODE, which has the general solution

$$f(kx - \omega t) = \bar{A} \sin \left(\frac{N\sqrt{12(k^2 - \nu_0^{-2}d^2T^{-2}\omega^2)}}{k^2}(kx - \omega t) + \psi \right).$$

Now imposing the boundary condition (3.24d), we solve for the amplitude and phase: $(\bar{A}, \psi) = (-A, 0)$. We also obtain the dispersion relation

$$\omega^2 = k^2 \frac{\nu_0^2 T^2}{2d^2} \left(1 \pm \sqrt{1 - \frac{1}{3} \frac{\nu_0^{-2} h^2}{T^2} \alpha^2} \right).$$

Because this is a dispersion relation for a non-dimensionalized equation, ω and k are unitless[†], as is the parameter α . For a physical solution, the phase velocity must be positive ($\omega/k > 0$), so we raise the above equation to the 1/2 power and discard the negative root. Putting everything together, we have the two fundamental modes

$$V_{\pm}(x, t) = \begin{cases} \sin\left[\alpha\left(\frac{k}{\omega_{\pm}}x - t\right)\right] & x < \frac{\omega_{\pm}}{k}t \\ 0 & x \geq \frac{\omega_{\pm}}{k}t. \end{cases} \quad (3.30a)$$

$$\frac{\omega_{\pm}}{k} = \frac{\nu_0 T}{\sqrt{2}d} \left(1 \pm \sqrt{1 - \frac{1}{3} \frac{\nu_0^{-2} h^2}{T^2} \alpha^2}\right)^{1/2}. \quad (3.30b)$$

By linearity of (3.28), the general solution of the $\lambda = 0$ equation is the superposition

$$V = -A_1 V_+ - A_2 V_-, \quad (3.31)$$

where $A_1 + A_2 = A$. Applying the second boundary condition (3.24e) we have

$$A_1 = \frac{A\omega^+}{\omega^+ - \omega^-}, \quad A_2 = -\frac{A\omega^-}{\omega^+ - \omega^-}. \quad (3.32)$$

3.2.6 Discussion

Using the dispersion relation (3.30b), we can calculate the cut-off frequency of the line. This is the frequency α for which ω becomes imaginary, which in the case of (3.30b) gives the relation

$$\alpha^2 < \frac{3T^2}{lc}.$$

Here we used the definition $\nu_0^{-1} = \sqrt{LC}$ where $L = l/h$ and $C = c/h$.

Taking $h = 0$ in the above formula produces the classical solution to the linear wave equation, with the single right-moving mode

$$\omega_0/k = \nu_0.$$

[†]The careful reader may verify that, because L and C still represent *distributed* inductance and capacitance, the number ν_0^2 has units of velocity squared, implying that the right-hand side of dispersion relation (3.30b) is also unitless, and remains so even in the $h \rightarrow 0$ limit.

Taking $h > 0$ in (3.30), we find three effects of discreteness. The first is dispersion: though the phase velocity equals the group velocity of the outgoing signal, viz.

$$\frac{\omega_{\pm}}{k} = \frac{d\omega_{\pm}}{dk},$$

we see from (3.30b) that both of these velocities are nonlinear functions of α , the frequency of the incoming signal. Second, there are now two right-moving modes, one fast and one slow, corresponding to ω^+/k and ω^-/k . Finally, discreteness causes a decrease in the maximum speed of the wave train; this follows immediately from $\omega^+/k < \omega_0/k$.

3.2.7 General Case

We examine (3.28) with $\lambda > 0$. On physical grounds we expect that the voltage grows as a function of distance from its starting point $x = 0$. Accordingly, we introduce the ansatz

$$V^{\lambda}(x, t) = \exp(c_1 x) f(z) \tag{3.33}$$

where $z = kx - \omega t$. Inserting (3.33) in (3.28), we obtain

$$\begin{aligned} \nu_0^{-2} \omega^2 f'' &= (c_1^2 f + 2c_1 k f' + k^2 f'') + \frac{h^2}{12} (c_1^4 f + 4c_1^3 k f' + 6c_1^2 k^2 f'' + 4c_1 k^3 f^{(3)} + k^4 f^{(4)}) \\ &\quad - \lambda \left(c_1 f + k f' + \frac{h^2}{6} (c_1^3 f + 3c_1^2 k f' + 3c_1 k^2 f'' + k^3 f^{(3)}) \right). \end{aligned} \tag{3.34}$$

Choose $c_1 = \lambda/2$ to eliminate the $f^{(3)}$ terms exactly. Two of the f' terms cancel. We further ignore all terms of order λ^m , $m \geq 2$, obtaining

$$\nu_0^{-2} \omega^2 f'' = k^2 f'' + \frac{h^2}{12} k^4 f^{(4)},$$

which is precisely the equation we solved in the $\lambda = 0$ case. Hence an approximate solution of (3.28), correct to $\mathcal{O}(\lambda^2)$, is given by

$$V^{\lambda}(x, t) = \exp(\lambda x/2) V(x, t), \tag{3.35}$$

with V defined in (3.30-3.32).

Discussion. The qualitative effect of a small but positive value of λ is now clear. The frequency and speed of propagation for the outgoing signal is unchanged from the $\lambda = 0$ case. The only effect we expect to observe is growth of the initial sinusoid as it propagates down the line.

Since it appears from (3.35) that we have produced a voltage that is unbounded in space, we remind the reader that in reality, the transmission line is terminated at its right boundary, say at $x = X$. So long as the resistive termination is chosen so that the reflection coefficient is nearly zero, we may use (3.35) to predict the waveform at any point $x \in [0, X]$.

Remark. Exact solutions of (3.34) can be obtained computationally. Let us outline the procedure in this case. First, we write the full expression of (3.34) in the form

$$\sum_{i=0}^4 q_{i+1} f^{(i)}(z) = 0, \text{ where } \mathbf{q} = \begin{pmatrix} -(\lambda^2/4) - (\lambda^4 h^2/64) \\ (\lambda^3 h^2/12)k \\ k^2 - \nu_0^{-2} \omega^2 - (\lambda^2 h^2/8)k^2 \\ 0 \\ h^2 k^4/12 \end{pmatrix}. \quad (3.36)$$

Here we use the convention that $\mathbf{q} = (q_1, q_2, q_3, q_4, q_5)$. One way to determine a unique solution is to specify the four initial conditions $f^{(i)}(0)$ where $i = 0, 1, 2, 3$. We leave it as an exercise to show that the four conditions (3.24b-3.24e) also determine the solution uniquely. Then (3.36) can be solved via the matrix exponential. Let $\mathbf{y} \in \mathbb{R}^4$ have coordinates $y_i = f^{(i-1)}$ for $i = 1, 2, 3, 4$. Now write (3.36) as the first-order system

$$\frac{d\mathbf{y}}{dz} = M\mathbf{y}, \quad (3.37)$$

where

$$M = \begin{pmatrix} 0 & 1 & 0 & 0 \\ 0 & 0 & 1 & 0 \\ 0 & 0 & 0 & 1 \\ -q_1/q_5 & -q_2/q_5 & -q_3/q_5 & 0 \end{pmatrix}. \quad (3.38)$$

The solution to (3.37) is then

$$\mathbf{y}(z) = e^{Mz} \mathbf{y}(0). \quad (3.39)$$

In practice, given particular values of all required constants, the solution can be found easily using Matlab. As a final remark, note that we do not need to compute the entire vector \mathbf{y} , but merely the first component $y_1(z) = f(z)$.

3.3 Nonuniform Nonlinear Case

Of course, we can build transmission lines that are both nonuniform and nonlinear. To model such lines, we recognize that $c_n(V)$ in (3.20b) is no longer time-independent. Hence combining (3.20a) and (3.20b) in the nonlinear case, where $\partial C/\partial V \neq 0$, we find

$$\ell_{n+1/2}(V_{n-1} - V_n) - \ell_{n-1/2}(V_n - V_{n+1}) = \ell_{n-1/2} \ell_{n+1/2} \frac{d}{dt} \left(c_n \frac{dV_n}{dt} \right). \quad (3.40)$$

From here, the derivation of the continuum model proceeds precisely as in the linear case. The end result is

$$V_{xx} - L \frac{\partial}{\partial t} (CV_t) = V_x \frac{L_x}{L} - h^2 \left(\frac{1}{12} V_{xxxx} - \frac{1}{6} \frac{L_x}{L} V_{xxx} \right). \quad (3.41)$$

Suppose we take $C(x, V) = C_0(x)(1 - bV)$ and $L(x)C_0(x) = \nu_0^{-2}$. Then introducing the change of variables (3.10), we may again use (3.11) to rewrite our equation. We note that in order to balance terms, we must treat the inductance in a particular way. We first write

$$L(x) = L(\varepsilon^{-1/2}s + \nu_0 \varepsilon^{-3/2}T),$$

so that

$$\frac{\partial L}{\partial T} = \varepsilon^{-3/2} \frac{dL}{dx}.$$

In this case, the order ε^3 equation is

$$\nu_0 \frac{\partial^2 V_1}{\partial s \partial T} + \frac{b\nu_0^2}{4} \frac{\partial^2 V_1^2}{\partial s^2} + \frac{\nu_0^2 h^2}{24} \frac{\partial^4 V_1}{\partial s^4} - \nu_0^2 \frac{L_T}{L} \frac{\partial V_1}{\partial s} = 0. \quad (3.42)$$

By introducing the time variable $\tau = \nu_0 T$ and taking $L_T/L = \lambda/\nu_0$, we remove ν_0 from the equation. We integrate with respect to s , obtaining

$$V_\tau + \frac{b}{2} V V_s + \frac{h^2}{24} V_{sss} - \lambda V = 0, \quad (3.43)$$

where as before we use V to denote V_1 , the leading-order contribution in the expansion (4.25). Equation (3.43) has been studied before as a "variable-depth" KdV equation. The now classical result[64] is that for λ small but positive, the usual soliton waveform of the KdV equation is modified by a shelf of elevation that trails the solitary wave. That is, the solution is no longer a symmetric sech^2 pulse, but instead the wave decays at its left boundary with a larger height than at its right boundary. The shelf elevation is $\mathcal{O}(\lambda)$ while its length is $\mathcal{O}(\lambda^{-1})$. The detailed $\tau \rightarrow \infty$ dynamics have been analyzed[65] by way of the transformation

$$V(s, \tau) = u(s, \tau) \exp(\lambda\tau),$$

which is used to convert (3.43) to a variable-coefficient KdV equation

$$u_\tau + \frac{b}{2} e^{\lambda\tau} u u_s + \frac{h^2}{24} u_{sss} = 0.$$

It is found that on a sufficiently large time scale, the trailing shelf degenerates into a train of small-amplitude solitary waves.

3.4 Numerics

We have performed direct numerical simulations of realistic transmission lines, using a finite-difference scheme. After describing the numerical scheme, we discuss different test cases. Our first goal is to validate our continuum models by comparing their predictions against numerical solutions of the underlying semi-discrete equations. Our second goal is to demonstrate useful applications through carefully selected numerical experiments.

3.4.1 Scheme

Equations (3.23) and (3.41) are, respectively, linear and nonlinear continuum models of the semi-discrete system (3.20). Continuum models are very useful for analytical studies; for numerical studies, we work directly with the semi-discrete system (3.20), which we rewrite here:

$$\frac{dI_{n+1/2}}{dt} = \frac{V_n - V_{n+1}}{\ell_{n+1/2}}, n \in [0, 1, 2, \dots, N] \quad (3.44a)$$

$$\frac{dV_n}{dt} = \frac{I_{n-1/2} - I_{n+1/2}}{c_n(V_n)}, n \in [1, 2, \dots, N - 1]. \quad (3.44b)$$

As in the continuum model, we take the line to be initially dead,

$$V_n(0) = 0 \quad \text{and} \quad \frac{dV_n}{dt}(0) = 0, \quad n > 0, \quad (3.45)$$

and we also incorporate sinusoidal forcing at the left boundary:

$$V_0(t) = A \sin \alpha t. \quad (3.46)$$

However, for obvious reasons, the computational transmission line cannot be semi-infinite. We terminate the line at node N , necessitating the right boundary condition

$$V_N(t) = I_{N-1/2}(t)R, \quad (3.47)$$

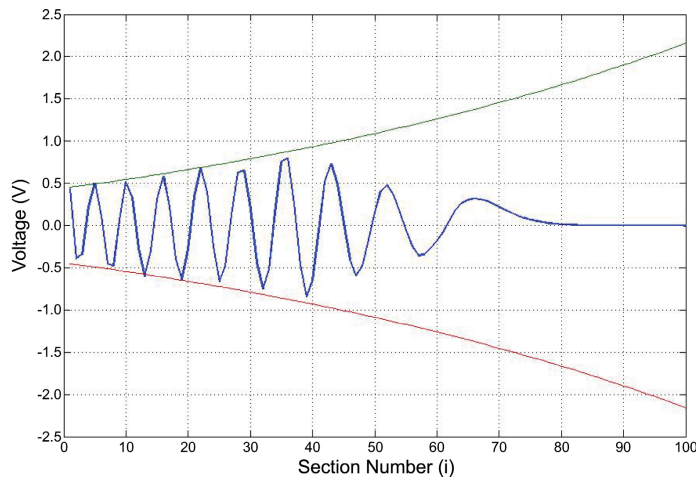


Figure 3.2: Voltage V_i versus element number i at $T = 10$ ns for a 1D nonuniform linear transmission line with parameters: $N = 100$, $L_0 = 0.1$ nH, $C_0 = 1$ pF. The input, at the left end of the line ($i = 0$), is a sinusoid with frequency $\alpha = 5$ GHz.

where R is the termination resistance. We choose R such that the reflection coefficient at the right boundary is practically zero. Taking (3.44-3.47) together, we have a closed system for the interior voltages and inductances. We solve this system directly using the standard `ode45` Runge-Kutta method in Matlab.

3.4.2 Remark

The procedure described above is entirely equivalent to solving the PDEs (3.23) and (3.41) by the method of lines combined with a finite difference spatial discretization. The method is accurate to second-order in space and fourth-order in time.

3.4.3 Results

First we simulate a linear exponentially tapered line. As predicted by the perturbative theory, we see two modes propagating inside an exponentially shaped envelope. As shown in Figure 3.2, the amplitude of the wave increases slowly as a function of element number.

Next we simulate both uniform and nonuniform NLTs. In the nonuniform case,

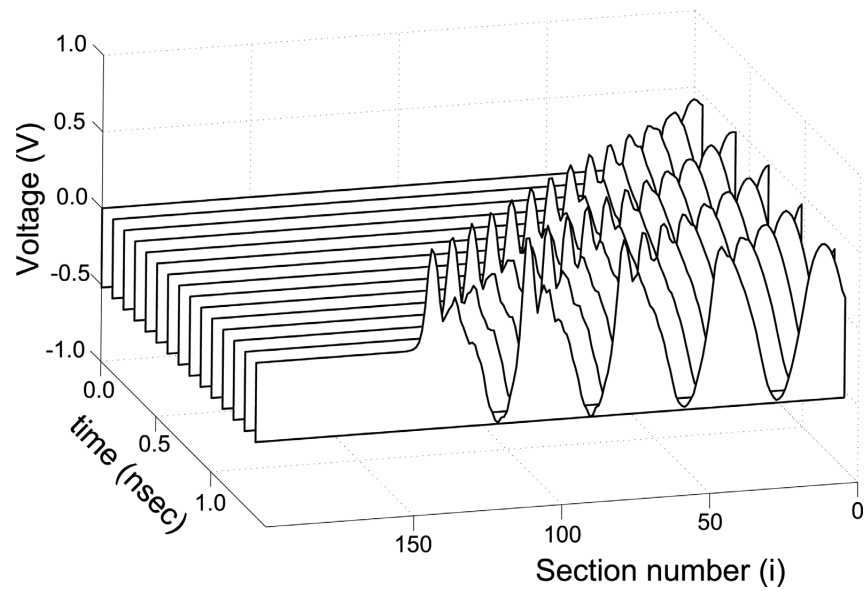
we use the exponential tapering described above. We observe in Figure 3.3(a) that sinusoids are now converted to soliton-like waveforms. If we switch on nonuniformity, multiple pulse generation is suppressed, as shown in Figure 3.3(b). That is, fewer solitonic pulses are generated from the same incoming sinusoidal signal.

The nonuniformity also allows us to narrow the width of pulses considerably, as demonstrated in 3.4. Note that Figure 3.4 also shows that the resulting pulses are not symmetric, as predicted by theory. The asymmetry appears on the left (trailing) side of the pulse.

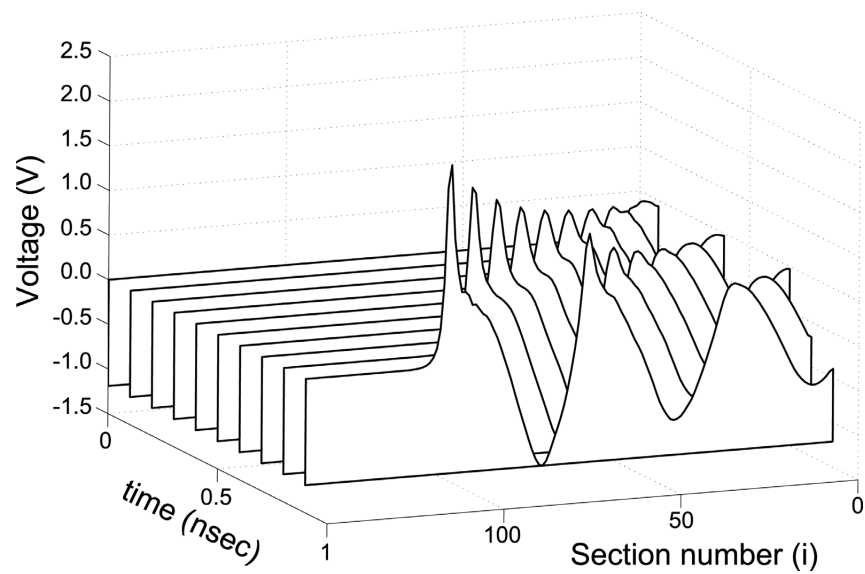
To summarize,

- The nonuniform linear transmission line can be used for pulse compression / voltage amplification. However, the frequency and speed of outgoing waves cannot be significantly altered using a linear circuit.
- The nonuniform nonlinear transmission line can increase both the voltage amplitude and the frequency content of incoming waves.

In the next chapter, we generalize 1D transmission lines to 2D transmission lattices. The extra dimension allows us to create a circuit that can simultaneously upconvert and combine incoming signals.



(a) Uniform



(b) Nonuniform

Figure 3.3: Voltage V_i versus element number i at various times for the (a) uniform NLTL, with $b = 0.5$, $\lambda = 0$, and (b) nonuniform NLTL, with $b = 0.25$, $\lambda = 0.02$. All other parameters are the same as in the linear case. The input frequency is $\alpha = 5$ GHz.

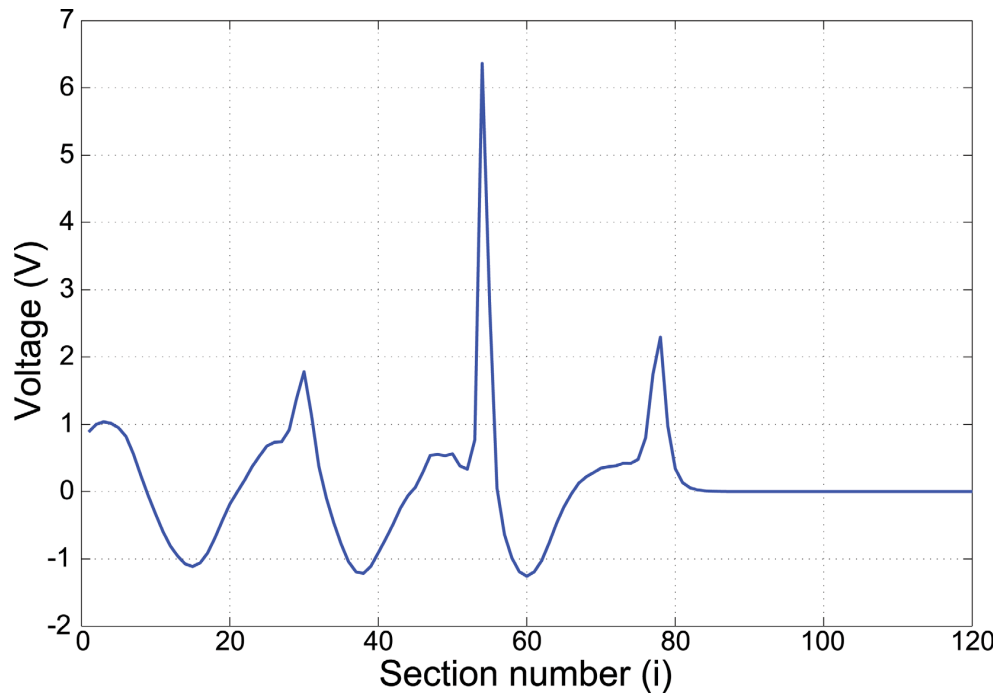


Figure 3.4: Voltage V_i versus element number i for the 1D nonuniform NLTL, with parameters identical to the previous figure. The outgoing pulse has a larger amplitude and much smaller wavelength than the sinusoidal signal that enters at the left boundary.

Chapter 4

Theory of Two-Dimensional Transmission Lattice

In this chapter, the extension of 1D transmission line to two dimensions is considered. For the description of long waves in a 2D lattice consisting of 1D lines coupled together by capacitors, one obtains a modified Zakharov-Kuznetsov (ZK) equation [57]. It should be mentioned that in §2.9 of Scott's treatise[4], precisely this sort of lattice is considered, and a coupled mode theory is introduced. These lattices consist of weakly coupled 1D transmission lines, in which wave propagation in one direction is strongly and inherently favored.

When a small transverse perturbation is added to the KdV equation, one obtains a Kadomtsev-Petviashvili (KP) model equation. Dinkel et al. [50] carry out this procedure for a uniform nonlinear 2D lattice, and mention that the circuit may be useful for "mixing" purposes; however, no physical applications are described beyond this brief mention in the paper's concluding remarks.

In this work, for a linear nonuniform lattice, we write the continuum model and derive a family of exact solutions. A continuum model is also derived for the nonlinear nonuniform lattice. In this case, we apply the reductive perturbative method and show that a modified Kadomtsev-Petviashvili (KP) equation describes weakly nonlinear wave propagation in the lattice.

Furthermore, we present a variety of numerical results. We choose the inductance and capacitance of lattice elements in a particular way, which we call an electric lens

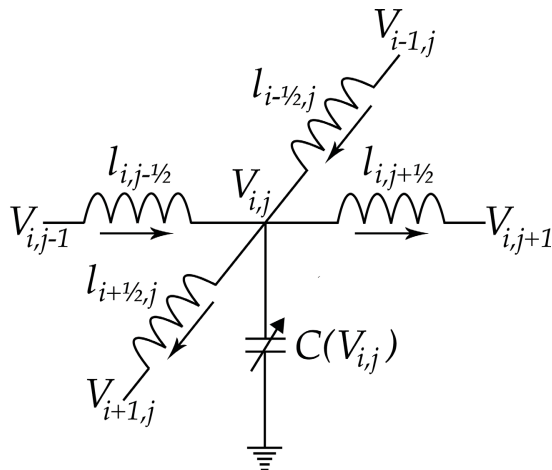


Figure 4.1: 2D transmission lattice

or funnel configuration. We solve the semi-discrete model of the lattice numerically, and show that the resulting solutions have physically useful properties. For example, our numerical study predicts that a linear nonuniform lattice can focus up to 70% of the power of input signals with frequency content in the range 0-100 GHz. We present numerical studies of nonlinear lattices as well. In this case, power focusing is present alongside frequency upconversion, or the ability of the lattice to *increase* the frequency content of input signals. The numerical studies show that nonlinear nonuniform lattices can be used for wideband signal shaping applications.

4.1 Nonuniform Linear Case

Consider a section of the two-dimensional transmission lattice shown in Figure 4.1. Using only regular polygons, there are three possible lattice blocks that can be used to tile the two-dimensional plane: triangular, rectangular, and hexagonal. Though the governing equations in each case will be different, at the continuum limit, they will have the same physical properties. Therefore, for mathematical simplicity, we analyze only the rectangular case. As in the previous section, we suppose that the

lattice is nonuniform, meaning

$$\nabla L(x, y) \neq \mathbf{0}, \quad \nabla C(x, y) \neq \mathbf{0}.$$

For now, we assume the lattice is linear:

$$\frac{\partial C}{\partial V} = 0, \quad \frac{\partial L}{\partial I} = 0.$$

Then Kirchoff's laws yield the semi-discrete system:

$$I_{i,j-1/2} + I_{i-1/2,j} - I_{i+1/2,j} - I_{i,j+1/2} = c_{ij} \frac{dV_{ij}}{dt} \quad (4.1a)$$

$$V_{ij} - V_{i,j-1} = -\ell_{i,j-1/2} \frac{d}{dt} I_{i,j-1/2} \quad (4.1b)$$

$$V_{ij} - V_{i+1,j} = \ell_{i+1/2,j} \frac{d}{dt} I_{i+1/2,j} \quad (4.1c)$$

Differentiating (4.1a) with respect to time, we substitute (4.1b-4.1c), yielding

$$\frac{V_{ij} - V_{i,j-1}}{\ell_{i,j-1/2}} + \frac{V_{ij} - V_{i-1,j}}{\ell_{i-1/2,j}} + \frac{V_{ij} - V_{i+1,j}}{\ell_{i+1/2,j}} + \frac{V_{ij} - V_{i,j+1}}{\ell_{i,j+1/2}} = -c_{ij} \frac{d^2 V_{ij}}{dt^2}. \quad (4.2)$$

Taking the continuum limit in the usual way, we obtain the $\mathcal{O}(h^0)$ lattice model

$$\nabla^2 V - LCV_{tt} = \frac{\nabla V \cdot \nabla L}{L}, \quad (4.3)$$

where

$$\nabla^2 V = V_{xx} + V_{yy}.$$

Or, if we keep all terms at order h^2 , we obtain

$$\begin{aligned} \nabla^2 V - LCV_{tt} &= \frac{\nabla V \cdot \nabla L}{L} \\ &- h^2 \left[\frac{1}{12} (V_{xxxx} + V_{yyyy}) - \frac{1}{6} \frac{L_x V_{xxx} + L_y V_{yyy}}{L} - \frac{1}{4} \frac{L_x^2 V_{yy} + L_y^2 V_{xx}}{L^2} \right] \end{aligned} \quad (4.4)$$

In the practical examples we consider, L will be a slowly varying function of both x and y , rendering negligible the terms involving squared derivatives of L , i.e., L_x^2/L^2 and L_y^2/L^2 . Our $\mathcal{O}(h^2)$ lattice model is

$$\nabla^2 V - LCV_{tt} = \frac{\nabla V \cdot \nabla L}{L} - \frac{h^2}{12} (V_{xxxx} + V_{yyyy}) + \frac{h^2}{6} \frac{L_x V_{xxx} + L_y V_{yyy}}{L} \quad (4.5)$$

In this equation, the left-hand side is the normal wave propagation equation. On the right, the first term corresponds to the inhomogeneity, the second term is due to the discreteness and the last term represents both inhomogeneity and discreteness.

4.1.1 Large Lattice

e will now consider an extremely large lattice, i.e., the case when M and N are both very large. In this case, we may ignore the $\mathcal{O}(h^2)$ terms and use (4.3) as our governing equation. The reason is simple: suppose we non-dimensionalize (4.5) and write an equation analogous to the 1D equation (3.26). The third- and fourth-order derivatives of voltage V will be multiplied by factors of $1/N^2$ and $1/M^2$ in the resulting equation; hence these terms are negligible.

The approximation gains further justification due to the linearity of (4.5). Let V^h denote the solution of (4.5). Because (4.5) is linear, we expect that for small h , the solution can be expanded in the form

$$V^h(x, y, t) = V_0(x, y, t) + h^2 V_1(x, y, t) + \mathcal{O}(h^4),$$

where V_0 is the solution of the $h = 0$ equation (4.3). Then it is clear that

$$|V^h - V_0| = \mathcal{O}(h^2),$$

or in words, the solution V_0 is in fact the zero-dispersion limit of the solutions V^h . Note that a similar analysis would *not* work in the nonlinear regime—see our earlier remarks on zero-dispersion limits for uniform 1D NLTs.

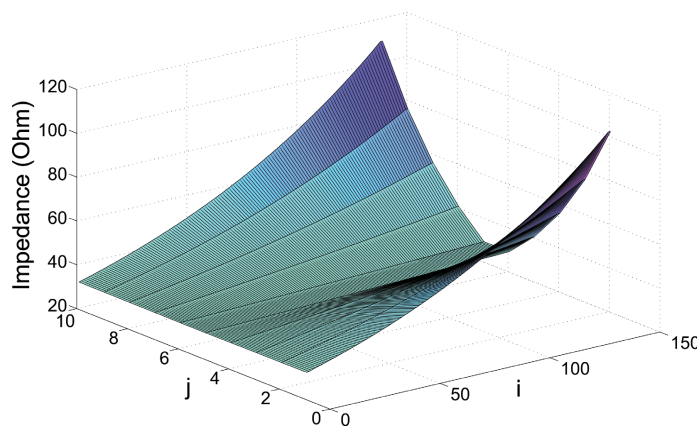


Figure 4.2: Keeping Z_{ij} constant and defining $T_{ij} = n\sqrt{L_{ij}C_{ij}}$ by the above graph results in an electric lens. Keeping T_{ij} constant and defining $Z_{ij} = \sqrt{L_{ij}/C_{ij}}$ by the above graph results in an electric funnel. Note that this is the precise impedance surface used in the 2D numerical simulations that follow.

4.1.2 Lens/Funnel

For the purposes of combining signals, we wish to build an *electric lens* or *electric funnel*. The situation is analogous to that in optics. The main physical property of the lens that is responsible for its focusing action is the wave velocity increases as we go farther away from the z -axis as shown in Figure 4.2. In this way, the input sources add coherently at the focal point.

Let us examine some physical arguments that suggest various configurations of L and C which result in lens/funnel circuits. Standard transmission line theory shows that the delay of the LC transmission line is approximately

$$T = n\sqrt{LC}$$

where n is the number of LC sections. Also the characteristic impedance of the line is given by:

$$Z = \sqrt{L/C}.$$

In order to have a lens, we keep the impedance Z constant but let the delay T vary in space as shown in Figure 4.2. Of course, this method works for a single frequency. (For other frequencies, the phase shift from the input to the output is different, and as a result, the focal length is different as well).

Another approach is to keep T constant (i.e. keep constant the delay from the input to the output), while increasing Z as shown in Figure 4.2. This approach works for all frequencies and the resulting circuit is wideband. We call this circuit a funnel.

Here we concentrate our efforts on the two-dimensional *electric funnel* that has a shape similar to that of these functions:

$$\begin{aligned} L(x, y) &= B \exp(\lambda xy^2) \\ C(x, y) &= \frac{1}{B\nu_0^2} \exp(-\lambda xy^2), \end{aligned}$$

where ν_0, λ, B are positive constants. In what follows, we assume that $L(x, y)C(x, y) = \nu_0^{-2}$ everywhere, but we will leave open the exact functional expression for L .

4.1.3 A Physical Scenario

The transmission lattice is dead (no voltage, no current) at $t = 0$, at which point a sinusoidal voltage source is switched on at the left boundary. We assume that the transmission lattice is long in the x coordinate, and that it is terminated at its (physical) right boundary in such a way that the reflection coefficients there are very small. Hence we model the transmission lattice as semi-infinite in the x coordinate, but bounded in the y coordinate by the lines $y = -1$ and $y = +1$.

We formalize this as an initial-boundary-value problem (IBVP). Given a transmission lattice on $S = [0, \infty) \times [-1, 1]$, we seek a function $V(x, y, t) : S \times [0, \infty) \rightarrow \mathbb{R}$

that solves

$$\nu_0^{-2}V_{tt} = \nabla^2V - \frac{\nabla V \cdot \nabla L}{L} \quad (4.6a)$$

$$V(x, y, 0) = 0 \quad (4.6b)$$

$$V_t(x, y, 0) = 0 \quad (4.6c)$$

$$V(0, y, t) = A \sin \alpha t \quad (4.6d)$$

$$V_x(0, y, t) = 0 \quad (4.6e)$$

where A, α are arbitrary constants. We first describe a family of exact solutions of this system that can be derived in an elegant fashion. Then we describe numerical simulations for a specific class of functions L . The simulations will show the EWB signal-shaping properties of the lattice.

4.1.4 Exact Solutions

Suppose we insist on a solution V that is separable in the following sense:

$$V(x, y, t) = f(x, y)g(x, t). \quad (4.7)$$

Here g satisfies the constant impedance equation $\nu_0^{-2}g_{tt} = \nabla^2g$, i.e.

$$g(x, t) = -A \sin \left[\frac{\alpha}{\nu_0}(x - \nu_0 t) \right]. \quad (4.8)$$

In words, V represents a sinusoidal wave front g that propagates to the right along perfectly horizontal rays, with spatially dependent amplitude f . Inserting (4.7) into (4.6a) gives

$$\left(f_{xx} - f_x \frac{L_x}{L} \right) + \left(f_{yy} - f_y \frac{L_y}{L} \right) = \left(f \frac{L_x}{L} - 2f_x \right) \frac{g_x}{g}. \quad (4.9)$$

Now suppose that $(fL_xL^{-1} - 2f_x) \neq 0$. In this case, we could divide both sides of (4.9) by this quantity and obtain

$$\left(f\frac{L_x}{L} - 2f_x\right)^{-1} \left[\left(f_{xx} - f_x\frac{L_x}{L}\right) + \left(f_{yy} - f_y\frac{L_y}{L}\right)\right] = \frac{g_x}{g}.$$

As the left-hand side is time-independent, we would deduce that

$$\frac{\partial}{\partial t} \frac{g_x}{g} = 0,$$

which is a contradiction. Hence we know that

$$f\frac{L_x}{L} - 2f_x = 0,$$

which can be integrated easily, giving

$$f(x, y) = \kappa_1(y)\sqrt{L(x, y)}, \quad (4.10)$$

where κ_1 is an arbitrary positive function of y only. Reexamining (4.9), we see that a sufficient condition for a solution is if f and L satisfy

$$\left(f_{xx} - f_x\frac{L_x}{L}\right) = 0 \quad (4.11a)$$

$$\left(f_{yy} - f_y\frac{L_y}{L}\right) = 0. \quad (4.11b)$$

Substituting (4.10) into the first equation, we obtain an equation in L only:

$$-3(L_x)^2 + 2LL_{xx} = 0.$$

This ODE can be solved, and the answer is

$$L(x, y) = \frac{4}{(\kappa_3(y)x + \kappa_2(y))^2} \quad (4.12)$$

where $\kappa_3(y), \kappa_2(y)$ are functions of y only, and $\kappa_3 > 0$. Now substituting this back into (4.10), we obtain

$$f(x, y) = \frac{2\kappa_1(y)}{\kappa_3(y)x + \kappa_2(y)}. \quad (4.13)$$

Boundary conditions dictate that $f(0, y) = 1$, so we must have $2\kappa_1 = \kappa_2$. Now using (4.12) and (4.13) in the final equation (4.11b), we derive

$$\frac{\kappa_3}{\kappa_1} = \frac{\kappa_{3yy}}{\kappa_{1yy}}, \quad (4.14)$$

which relates κ_3 to κ_1 .

Result. Putting everything together, we arrive at the following result. Suppose that we are given $\kappa_2(y) > 0$ and $\kappa_3(y) > 0$ that satisfy the equation

$$\kappa_3 = \frac{\kappa_2}{\kappa_{2yy}} \kappa_{3yy}. \quad (4.15)$$

Then, using the inductance $L(x, y) = 4(\kappa_3(y)x + \kappa_2(y))^{-2}$, the equation (4.6) has the exact solution

$$V(x, y, t) = \frac{-A\kappa_2(y)}{\kappa_3(y)x + \kappa_2(y)} \sin \left[\frac{\alpha}{\nu_0} (x - \nu_0 t) \right]. \quad (4.16)$$

4.1.5 Properties

Using (4.16), we compute various quantities of interest.

1. *Current.* So far we have assumed that the current vector has a preferred direction and can be modeled by the scalar I . However, directly taking the continuum limit of (4.1b-4.1c) yields a formula for the current vector \mathbf{i} :

$$\mathbf{i} = -\frac{1}{L} \int \nabla V dt \quad (4.17)$$

Let $G = \int g(x, t) dt$ where g was defined in (4.8). Then substitution of the exact

solution (4.16) in (4.17) gives

$$\mathbf{i} = -\frac{1}{4} \begin{pmatrix} -\kappa_2\kappa_3G + \kappa_2(\kappa_3x + \kappa_2)G_x \\ \kappa_2'\kappa_3xG - \kappa_2\kappa_3'xG \end{pmatrix}. \quad (4.18)$$

2. *Power.* We compute $P = \|\mathbf{i}\|V$ and obtain

$$P = \frac{\kappa_2}{2} \left[\frac{\kappa_2^2\kappa_3^2 + x^2(\kappa_2'^2\kappa_3^2 - 2\kappa_2'\kappa_2\kappa_3'\kappa_3 + \kappa_2^2\kappa_3'^2)}{(\kappa_3x + \kappa_2)^2} G^2 - \frac{2\kappa_2^2\kappa_3}{\kappa_3x + \kappa_2} GG_x + \kappa_2^2 G_x^2 \right]^{1/2}. \quad (4.19)$$

Though we will not pursue this approach further in this thesis, we outline how the exact solution might be used in practice. Suppose we are interested in building a circuit that shapes signals in a particular way. Translated into our mathematical framework, this means that we seek an inductance function L that gives solutions V such that either V , \mathbf{i} , or P has some desired shape. For simplicity, suppose we are interested in designing a circuit such that $P(R, y, t)$ has a given profile for some fixed $R \in (0, \infty)$.

Now in principle, for a certain class of functions $p(y, t)$, it is possible to find κ_2 and κ_3 in such a way that (4.15) is satisfied *and*

$$P(R, y, t) = p(y, t). \quad (4.20)$$

Equation (4.15) and (4.20) are two equations for the two unknowns κ_2 and κ_3 . Suppose we find κ_2 and κ_3 that satisfy these constraints. Then we may immediately write the inductance L that we should use in our circuit to achieve the desired output power.

4.1.6 Discussion

We have chosen a particular L that allows us to explicitly solve the IBVP (4.6) assuming perfectly straight propagation of waves. In general, the solution $V(x, y, t)$ will not assume the convenient separation (4.7) that we have assumed, and an explicit

closed-form solution may not exist. A general funnel-shaped inhomogeneity causes rays to bend; the solution will be of the form

$$V(x, y, t) = f(x, y)g[\mathbf{k}(\mathbf{x}) \cdot \mathbf{x} - \omega t],$$

where the wave vector \mathbf{k} is not constant in space. We will explore applications of this idea in future work.

4.2 Nonuniform Nonlinear Case

Let us now add nonlinearity to the nonuniform 2D transmission lattice, i.e., suppose that

$$\frac{\partial C}{\partial V} \neq 0.$$

As in the 1D case, the continuum equation needs only one modification in the second-order time-derivative term. That is, examining the semi-discrete equations (4.1) we see that if c_{ij} depends on V_{ij} , then differentiating (4.1a) results in the right-hand side $\frac{d}{dt} \left(c_{ij} \frac{dV_{ij}}{dt} \right)$. This carries over to the continuum model, which we write for the nonlinear case:

$$L \frac{\partial}{\partial t} \left[C(V) \frac{\partial V}{\partial t} \right] = \nabla^2 V + \frac{h^2}{12} (V_{xxxx} + V_{yyyy}) - \frac{\nabla V \cdot \nabla L}{L} - \frac{h^2}{6} \frac{L_x V_{xxx} + L_y V_{yyy}}{L}. \quad (4.21)$$

We carry out the reductive perturbation procedure on this equation, to determine how long, uni-directional waves propagate through the lattice. Suppose that the varactors satisfy $C(V, x, y) = C_0(x, y)(1 - bV)$, and that $\nu_0^{-2} = L(x, y)C_0(x, y)$. Introduce the scaled variables

$$\xi = \varepsilon^{1/2}(x - \nu_0 t) \quad (4.22a)$$

$$\eta = \varepsilon y \quad (4.22b)$$

$$T = \varepsilon^{3/2} t. \quad (4.22c)$$

which correspond to the notions that (1) the wave motion occurs primarily along the semi-infinite x direction, (2) the wave form varies far less in the y direction than the x direction, (3) the length of the wave is large compared to its speed of propagation. In the scaled variables, we have

$$V(x, y, t) = V(\varepsilon^{-1/2}\xi + \nu_0\varepsilon^{-3/2}T, \varepsilon^{-1}\eta, \varepsilon^{-3/2}T),$$

which gives

$$\frac{\partial}{\partial x} = \varepsilon^{1/2} \frac{\partial}{\partial \xi} \quad (4.23a)$$

$$\frac{\partial}{\partial y} = \varepsilon \frac{\partial}{\partial \eta} \quad (4.23b)$$

$$\frac{\partial}{\partial t} = \varepsilon^{3/2} \frac{\partial}{\partial T} - \varepsilon^{1/2} \nu_0 \frac{\partial}{\partial \xi}. \quad (4.23c)$$

The inductance transforms as

$$L(x, y) = L(\varepsilon^{-1/2}\xi + \nu_0\varepsilon^{-3/2}T, \varepsilon^{-1}\eta).$$

Again we use $\partial L/\partial x = \varepsilon^{3/2}(\partial L/\partial T)$ and also $\partial L/\partial y = \varepsilon(\partial L/\partial \eta)$. Now introducing (4.23) into (4.21) we have

$$\begin{aligned} & \nu_0^{-2} \left(\varepsilon^3 \frac{\partial^2}{\partial T^2} - 2\varepsilon^2 \nu_0 \frac{\partial^2}{\partial T \partial \xi} + \varepsilon \nu_0^2 \frac{\partial^2}{\partial \xi^2} \right) \left(V - \frac{b}{2} V^2 \right) \\ &= \varepsilon \frac{\partial^2 V}{\partial \xi^2} + \varepsilon^2 \frac{\partial^2 V}{\partial \eta^2} + \frac{h^2}{12} \varepsilon^2 \frac{\partial^4 V}{\partial \xi^4} + \frac{h^2}{12} \varepsilon^4 \frac{\partial^4 V}{\partial \eta^4} \\ & \quad - \varepsilon^2 \frac{L_T}{L} V_\xi - \varepsilon^2 \frac{L_\eta}{L} V_\eta - \frac{h^2}{6} \left(\varepsilon^3 \frac{L_T}{L} V_{\xi\xi\xi} + \varepsilon^4 \frac{L_\eta}{L} V_{\eta\eta\eta} \right). \quad (4.24) \end{aligned}$$

Now introducing the formal expansion

$$V = \varepsilon V_1 + \varepsilon^2 V_2 + \dots, \quad (4.25)$$

and keeping terms to lowest order, ε^3 , we write a modified KP equation

$$2\nu_0^{-1}V_{T\xi} + b(VV_\xi)_\xi + \frac{h^2}{12}V_{\xi\xi\xi\xi} + V_{\eta\eta} - \frac{L_T}{L}V_\xi - \frac{L_\eta}{L}V_\eta = 0.$$

Introducing the time variable $\tau = (\nu_0/2)T$, we have the perturbed KP equation

$$V_{\tau\xi} + b(VV_\xi)_\xi + \frac{h^2}{12}V_{\xi\xi\xi\xi} + V_{\eta\eta} - \frac{\nu_0}{2}\frac{L_\tau}{L}V_\xi - \frac{L_\eta}{L}V_\eta = 0. \quad (4.26)$$

In the case where the line is uniform and $L_\tau = L_\eta = 0$, this reduces to the standard KP-II equation, or KP equation with positive dispersion:

$$\left[V_\tau + b(VV_\xi)_\xi + \frac{h^2}{12}V_{\xi\xi\xi\xi} \right]_\xi + V_{\eta\eta} = 0. \quad (4.27)$$

We make the trivial observation that for both (4.26) and (4.27), if we take V to be a one-dimensional wave front propagating across the (ξ, η) plane, i.e. $V(\xi, \eta, \tau) = V(\xi, \tau)$, then both equations reduce to the KdV equations considered earlier. Of course, (4.27) displays a wealth of phenomena beyond the KdV equation, of which soliton resonance is perhaps the most intriguing from the applications point of view. We will discuss this phenomenon in Chapter 8 in more details.

4.3 Numerics

So far we have presented analytical results for both linear and nonlinear lattices. Let us now turn to numerical simulations of the lattice dynamics, starting from Kirchoff's equations (4.1). These equations are discrete in space but continuous in time. For a lattice with M elements in the vertical direction and N elements in the horizontal direction, we have a system of $2MN$ ordinary differential equations (ODEs). By prescribing inductance and capacitance functions L and C together with initial and boundary conditions, we may numerically integrate these ODEs and solve for the voltage and current in the lattice. In our studies, we shall suppose that the lattice is initially dead: that is, at $t = 0$, all voltages and currents are zero except at the left

boundary. The left boundary is where we introduce the input signal, via

$$V_{1,j}(t) = V_0 \sin \alpha t.$$

Although our methods are general, in this work, we shall present results for lattices in which $M < N$.

For all subsequent numerical results, we will use the “funnel” inductance function of the form

$$L(x, y) = L_0 \exp(\lambda MNh^2 x|y|). \quad (4.28)$$

Recall that for the funnel, we keep LC constant, which means that

$$C(x, y) = C_0 \exp(-\lambda MNh^2 x|y|). \quad (4.29)$$

Physical limitations for on-chip fabrication of inductors and capacitors limit the maximum and minimum inductance and capacitance in the lattice. Hence for $N = 100$, λ should be of the order 10^{-2} .

4.3.1 Linear case.

First let us discuss numerical results for a linear nonuniform lattice. Given an input signal with power that is distributed evenly in the vertical direction, we will find that the power of the output signal is focused in a narrow vertical region. We present results for a lattice in the funnel configuration (4.28-4.29) with $L_0 = 0.1\text{nH}$, $C_0 = 1\text{pF}$, and $\lambda = 0.02$.

For Figures 4.3-4.5, the input frequency $\alpha = 10\text{GHz}$. As shown in Figure 4.3, the voltage increases as the wave front moves to the right. However, due to the constant delay ($LC = \text{const}$), we do not see bending of the wave form. Also, due to the linearity of the lattice, the output frequency is the same as the input frequency. For the same simulation, the current is shown in Figure 4.4. We clearly see the focusing of current near the central line $j = M/2$.

Let us explain these results intuitively. The current is voltage divided by impedance.

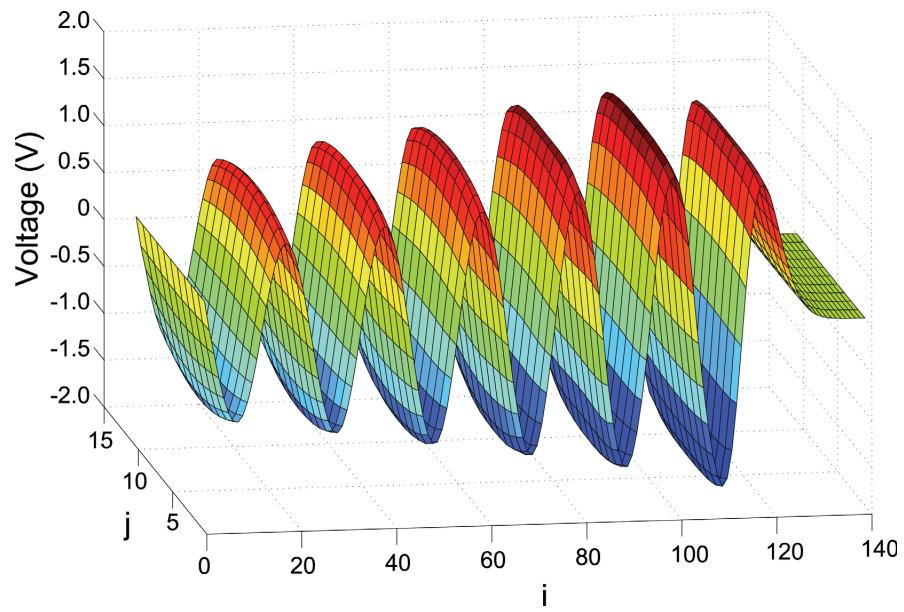


Figure 4.3: Voltage V_{ij} as a function of position (i, j) for the 2D nonuniform linear lattice.

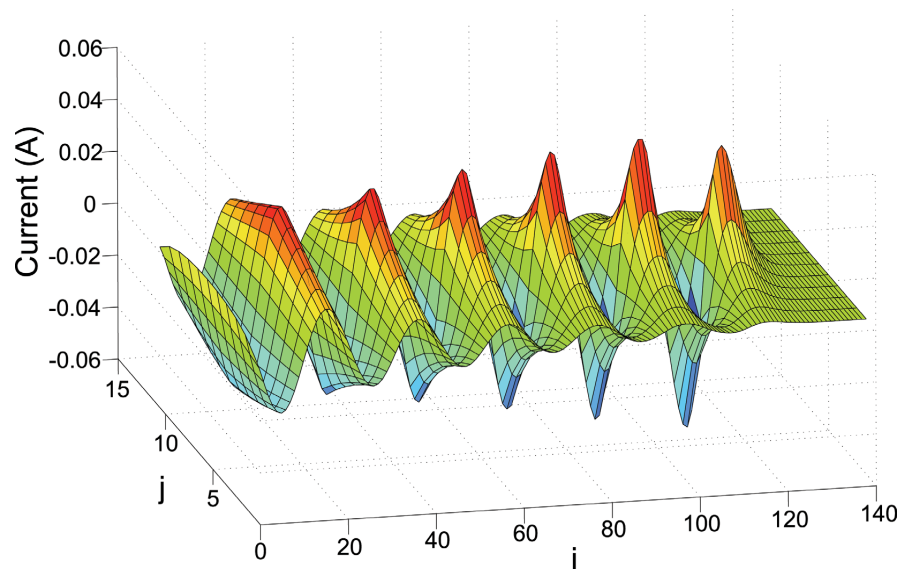


Figure 4.4: Current I_{ij} as a function of position (i, j) for the 2D nonuniform linear lattice, showing the funneling effect: the signal is stronger in the middle.

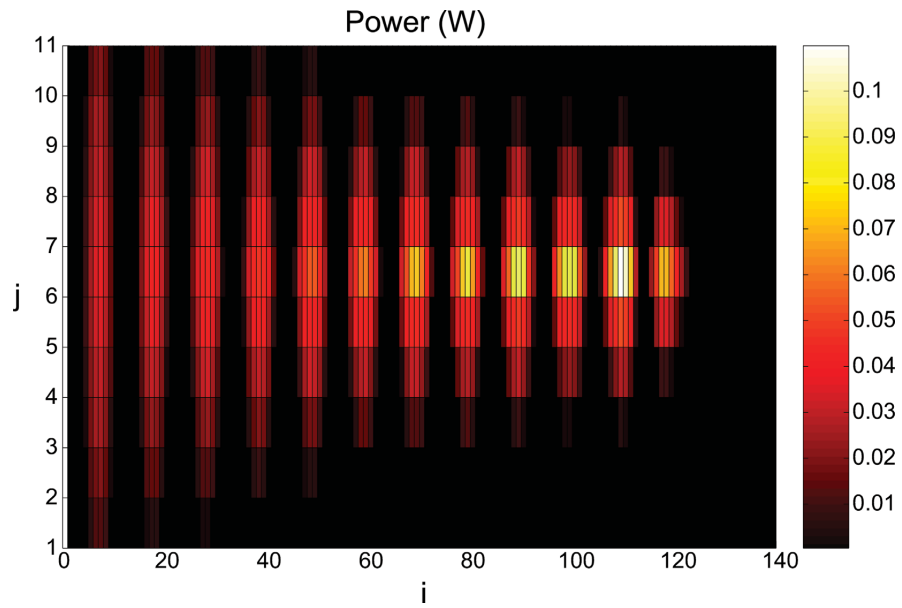


Figure 4.5: Power P_{ij} as a function of position (i, j) for the 2D nonuniform linear lattice, demonstrating the funneling effect.

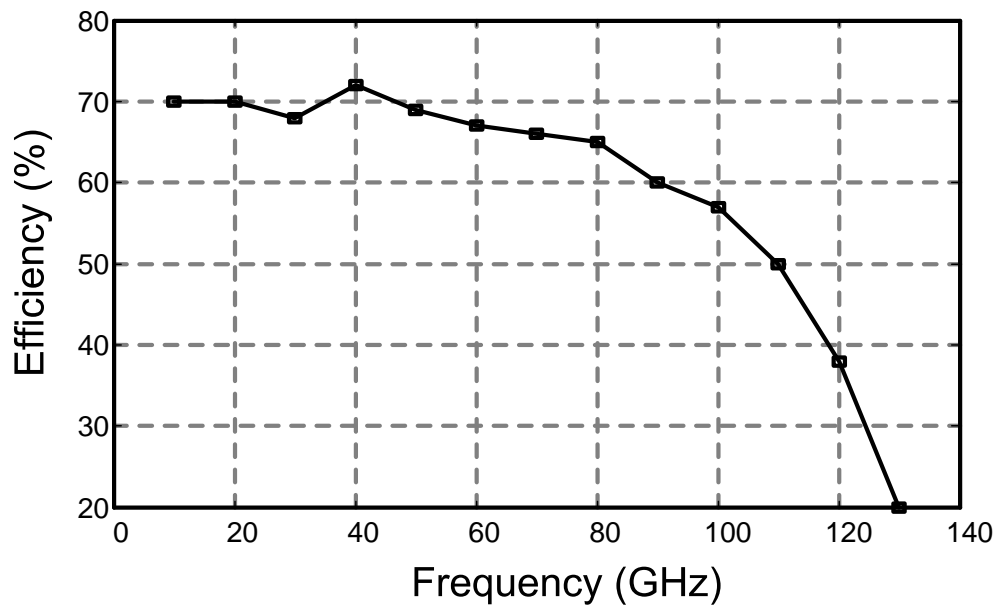


Figure 4.6: Efficiency as a function of input frequency for the 2D nonuniform linear lattice. Note that for an extremely wide range of input frequencies (0 - 100 GHz), the lattice focuses $\geq 60\%$ of the input power.

Based on Figure 4.3, we see that for each fixed i , the voltage is constant across all j . However, the impedance is larger at the vertical edges (see Figure 4.2), so the current is smaller there.

Figure 4.5 shows the instantaneous power profile in the lattice, computed using the previous solutions ($P = VI$). Note that the power is distributed evenly at $i = 0$, but at $i = 110$, the power is narrowly focused nearly the central line $j = M/2$.

For EWB applications, it is necessary that this power focusing behavior occur for input signals with frequency content in the range $0 \leq \alpha \leq 100\text{GHz}$. This is precisely what is shown in Figure 4.6. To produce this data, we simulated the linear uniform lattice repeatedly, with increasing values of α . In this figure, $L_0 = 0.1\text{nH}$, $C_0 = 1\text{pF}$, and $\lambda = 0.03$. The plotted quantity is the percentage of the input power that has been focused onto the central element of the lattice, at a fixed $i > 0$, and at a fixed time $t > 0$. (Recall that at $t = 0$, the power is distributed evenly, which means that the fraction of power in the central element at $i = 0$ is exactly $1/M$.)

4.3.2 Nonlinear Case

Next we provide numerical results for a nonlinear nonuniform lattice. To summarize, nonlinearity causes a change in the shape and frequency content of the input signal, features that are not present in linear lattices. We present results for a lattice in the funnel configuration, where L is the same as in the linear case—see (4.28). Nonlinearity arises from voltage-dependent capacitors, which we model using the first-order approximation

$$\begin{aligned} C(V) &= C_0(1 - bV) \\ C_0(x, y) &= \widehat{C}_0 \exp(-\lambda MNh^2x|y|). \end{aligned} \tag{4.30}$$

For our simulations, we choose $L_0 = 0.1\text{nH}$, $C_0 = 1\text{pF}$, $\lambda = 0.02$, and $b = 0.25\text{volts}^{-1}$.

Figures 4.7 and 4.8 show the voltage and current, respectively, for a rectangular lattice where $M = 9$ and $N = 140$. The plot of the voltage in Figure 4.7 shows similar behavior as in the one-dimensional nonlinear case—see Figure 3.4. In particular,

Figure 4.7 shows the narrowing of the input wave front at $i = 70$. One feature of the simulation that our theory does not explain is the nonuniform distribution of the voltage in j , for any fixed i .

For the same simulation, we plot the current in Figure 4.8, and observe the focusing of current along the center line $j = M/2$. The input wave front narrows considerably by $i = 70$. Nonlinearity of the lattice yields currents that are focused across a much narrower range of vertical elements than is possible in linear lattices. Note especially the sharp drop-off in current that is already present at $j = 50$. Not only is the focusing sharp, but it occurs faster than in the linear case.

Figures 4.9 and 4.10 show the instantaneous power profile ($P = VI$) for a lattice with $M = 5$ and $N = 140$. These plots demonstrate both the funneling effect and frequency upconversion. As shown, the maximum power level is higher than in the linear case, because the lattice compresses power simultaneously in space and time. (In the linear case, the power is compressed in space only.)

Conclusion Chapters 3 and 4 cover the theory of wave propagation in one and two dimensional LC lattices and show how to treat the effect of dispersion, nonlinearity, and inhomogeneity. Several analytical solutions as well as numerical results have been presented. Before we discuss the application of these theories in chapters 6 and 7, let us consider another approach for solving lattice equations using scattering method in the chapter 5.

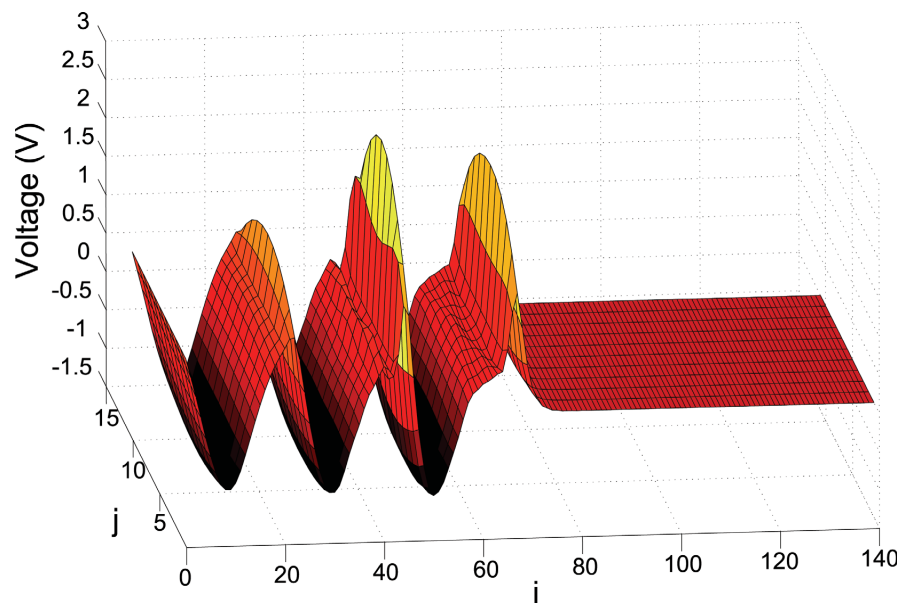


Figure 4.7: Voltage V_{ij} as a function of position (i, j) for the 2D nonuniform nonlinear lattice.

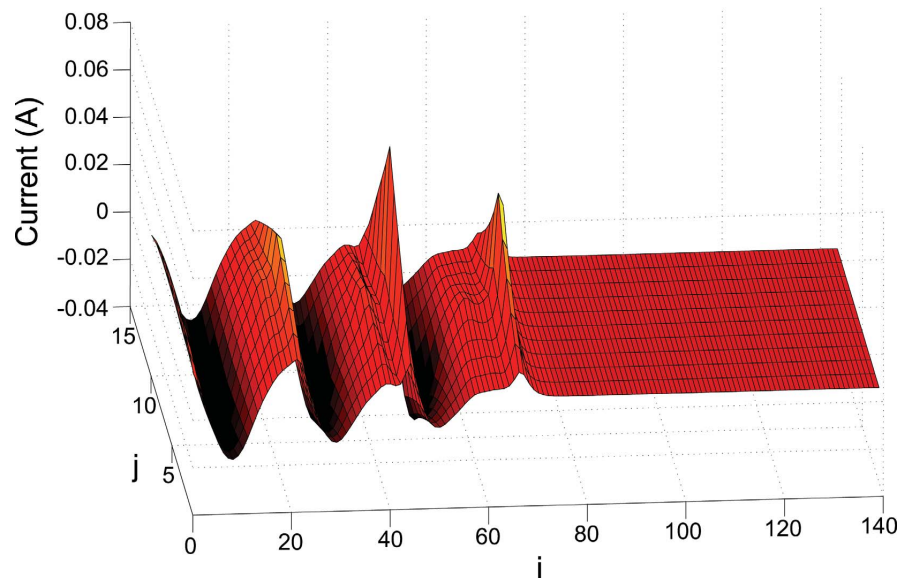


Figure 4.8: Current I_{ij} as a function of position (i, j) for the 2D nonuniform nonlinear lattice.

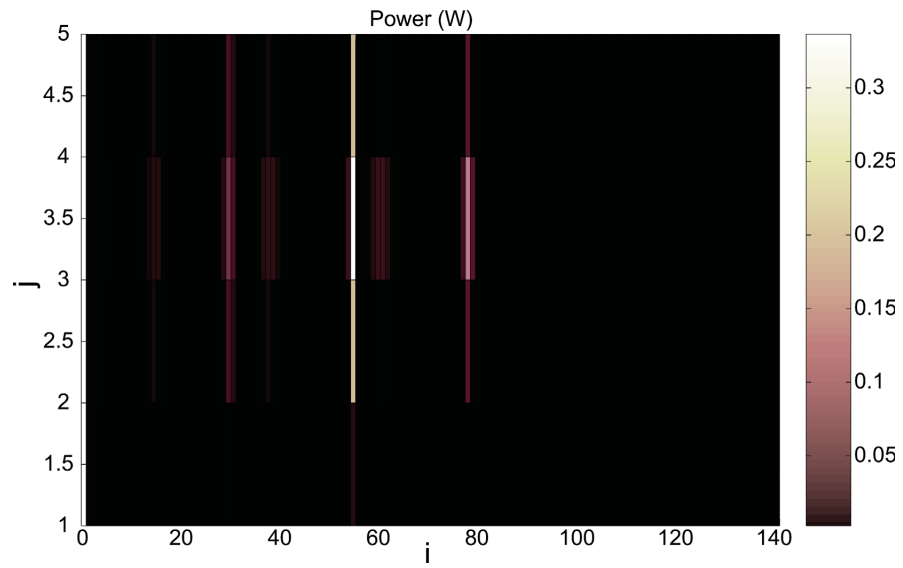


Figure 4.9: Power P_{ij} as a function of position (i, j) for the 2D nonuniform nonlinear lattice, demonstrating both the funneling effect and frequency upconversion.

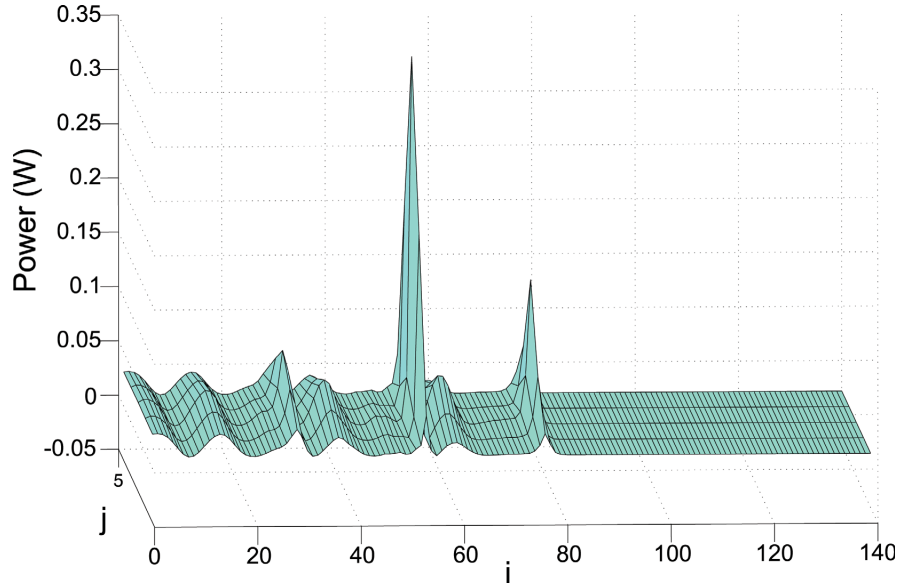


Figure 4.10: Power P_{ij} as a function of position (i, j) for the 2D nonuniform nonlinear lattice. This shows the same data as Figure (4.9).

Chapter 5

Scattering Theory for Electrical lines/lattices

An alternative approach to analytically solve one and two dimensional lattices, shown in previous chapters, is presented in this chapter. Here we introduce change of variables in order to modify our partial differential equations to the well-known equations such as Schrödinger equation. First we examine this method in one dimensional nonuniform transmission lines and then we will attempt to extend same methods to the problem of two dimensional inhomogeneous lattice.

5.1 One-Dimensional Transmission Line

Lets start with a 1D transmission line shown in 5.1

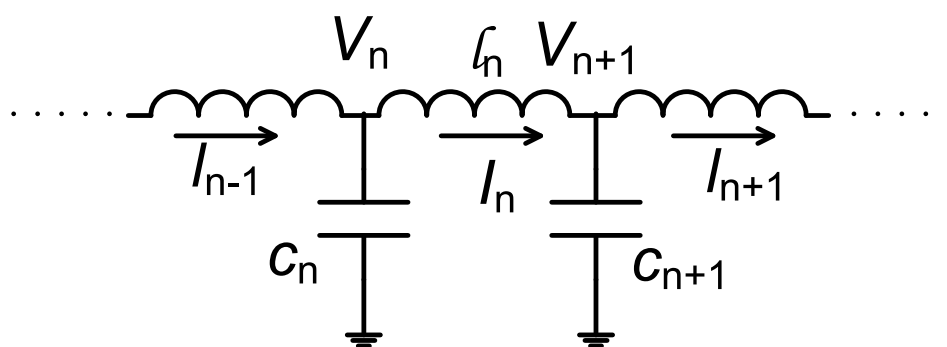


Figure 5.1: 1D nonuniform linear transmission line

We begin with the equations for current and voltage in a linear, one-dimensional,

infinite lattice:

$$c_n \frac{dV_n}{dt}(t) = I_{n-1}(t) - I_n(t) \quad (5.1a)$$

$$\ell_n \frac{dI_n}{dt}(t) = V_n(t) - V_{n+1}(t) \quad (5.1b)$$

5.1.1 Continuum Model

In order to pass to a continuum limit, we suppose that the elements in the lattice are separated by a constant distance h . Then, we introduce variables $I(z, t)$ and $V(z, t)$ which are meant to approximate the discrete variables $I_n(t)$ and $V_n(t)$, respectively. Specifically, we intend that

$$V(nh, t) = V_n(t) \quad (5.2a)$$

$$I(nh, t) = I_n(t) \quad (5.2b)$$

This implies that

$$\frac{\partial V}{\partial t}(nh, t) = \frac{dV_n}{dt}(t) \quad (5.3a)$$

$$\frac{\partial I}{\partial t}(nh, t) = \frac{dI_n}{dt}(t) \quad (5.3b)$$

Taylor expansions of (5.2) yield

$$V((n+1)h, t) = V(nh, t) + h \frac{\partial V}{\partial z}(nh, t) + O(h^2) \quad (5.4a)$$

$$I((n-1)h, t) = I(nh, t) - h \frac{\partial I}{\partial z}(nh, t) + O(h^2). \quad (5.4b)$$

Using (5.2-5.4) in (5.1) gives

$$c_n \frac{\partial V}{\partial t}(nh, t) = -h \frac{\partial I}{\partial z}(nh, t) + O(h^2) \quad (5.5a)$$

$$\ell_n \frac{\partial I}{\partial t}(nh, t) = -h \frac{\partial V}{\partial z}(nh, t) + O(h^2) \quad (5.5b)$$

We introduce the capacitance per unit length, $C(z)$, and the inductance per unit length, $L(z)$. These new quantities are related to the old ones by

$$hC(nh) = c_n \tag{5.6a}$$

$$hL(nh) = \ell_n \tag{5.6b}$$

Substituting (5.6) in (5.5), dividing by an overall factor of h , and using $z = nh$ results in

$$C(z) \frac{\partial V}{\partial t}(z, t) = -\frac{\partial I}{\partial z}(z, t) + O(h) \tag{5.7a}$$

$$L(z) \frac{\partial I}{\partial t}(z, t) = -\frac{\partial V}{\partial z}(z, t) + O(h) \tag{5.7b}$$

Then, as $h \rightarrow 0$, we obtain the continuum model

$$C \frac{\partial V}{\partial t} = -\frac{\partial I}{\partial z} \tag{5.8a}$$

$$L \frac{\partial I}{\partial t} = -\frac{\partial V}{\partial z} \tag{5.8b}$$

The typical initial-value problem for this system goes as follows: suppose, for all z , we are given $C(z)$, $L(z)$, $I(z, 0)$, and $V(z, 0)$. Using this information, solve (5.8) for the current $I(z, t)$ and $V(z, t)$ for all z and for all $t > 0$.

Remarks:

1. If we had included higher-order derivatives in the Taylor expansions (5.4), we could have accounted for dispersion in the lattice. Because all the dynamical equations we consider are *linear*, dispersion would produce a perturbative correction to the zero-dispersion solution. If h is sufficiently small, the behavior of (5.8) will closely approximate the true behavior.
2. Note that when L and C are both constant, system (5.8) reduces to the linear

wave equations

$$LC \frac{\partial^2 V}{\partial t^2} - \frac{\partial^2 V}{\partial z^2} = 0 \quad (5.9a)$$

$$LC \frac{\partial^2 I}{\partial t^2} - \frac{\partial^2 I}{\partial z^2} = 0 \quad (5.9b)$$

The solution of the initial-value problem for (5.9) is then given by D'Alembert's formula. The situation is identical to Maxwell's equations in a medium where both the permittivity and permissivity are constant.

3. Because the solution of (5.8) is known when L and C are constant, one may attempt an *adiabatic approximation* when L and C are *slowly varying functions* of the position z . This has not yet been attempted systematically.

Fourier transform. In what follows, we make use of the Fourier transform *in time*. For a function $f(z, t)$ we define its Fourier transform to be

$$\widehat{f}(z, \omega) = \frac{1}{2\pi} \int_{-\infty}^{\infty} f(z, t) e^{i\omega t} dt. \quad (5.10)$$

Given the Fourier transform $\widehat{f}(z, \omega)$, we may reconstruct the original signal using the inversion formula

$$f(z, t) = \int_{-\infty}^{\infty} \widehat{f}(z, \omega) e^{-i\omega t} d\omega. \quad (5.11)$$

In particular, using integration by parts, we may show that the Fourier transform of the time-derivative of $f(z, t)$ has a particularly nice form:

$$\begin{aligned} \frac{\partial \widehat{f}}{\partial t}(z, \omega) &= \frac{1}{2\pi} \int_{-\infty}^{\infty} \frac{\partial f}{\partial t}(z, t) e^{i\omega t} dt \\ &= -\frac{1}{2\pi} \int_{-\infty}^{\infty} f(z, t) \frac{\partial}{\partial t} e^{i\omega t} dt \\ &= -i\omega \frac{1}{2\pi} \int_{-\infty}^{\infty} f(z, t) e^{i\omega t} dt \\ &= -i\omega \widehat{f}(z, \omega). \end{aligned} \quad (5.12)$$

The Fourier transform is especially well-suited to constant coefficient linear partial differential equations posed on an infinite domain. Examining our system (5.8), we see that though $C(z)$ and $L(z)$ depend on space, they are constant with respect to time. Hence, taking the Fourier transform of (5.8), both $C(z)$ and $L(z)$ pass through the time integrals. For the time-derivatives, we apply (5.12), and thus obtain

$$i\omega C(z)\widehat{V}(z, \omega) = \frac{\partial \widehat{I}}{\partial z}(z, \omega) \quad (5.13a)$$

$$i\omega L(z)\widehat{I}(z, \omega) = \frac{\partial \widehat{V}}{\partial z}(z, \omega) \quad (5.13b)$$

Because (5.13) contains derivatives only with respect to the variable z , it is a system of *ordinary* rather than *partial* differential equations. In what follows, we will work *only* with the Fourier transforms $\widehat{V}(x, \omega)$ and $\widehat{I}(x, \omega)$. Therefore, we will leave off the “hats” and use $V(x, \omega)$ and $I(x, \omega)$.

5.1.2 Schrödinger Equation

We now describe how (5.13) is mathematically equivalent to the Schrödinger equation associated with a certain potential. This discussion follows Klemer and Sharpe [1984], IEEE Transactions on Antennas and Propagation, Vol. AP-32, No. 2, pp. 181-184.

First we introduce a change of variables:

$$x := x(z) = \int_0^z \sqrt{L(z')C(z')} dz'. \quad (5.14)$$

We may think of x as a normalized distance, though it has units of time since the delay \sqrt{LC} has units of time/distance. We also define the local characteristic impedance

$$Z_0(x) = \sqrt{\frac{L(x)}{C(x)}}. \quad (5.15)$$

Using (5.14-5.15), we may rewrite (5.13) as

$$i\omega \frac{1}{Z_0(x)} V(x, \omega) = \frac{dI}{dx}(x, \omega) \quad (5.16a)$$

$$i\omega Z_0(x) I(x, \omega) = \frac{dV}{dx}(x, \omega). \quad (5.16b)$$

To verify that (5.16) is equivalent to (5.13), substitute $x = x(z)$ into (5.16), multiply by $dx/dz = \sqrt{L(z)C(z)}$, and then apply the chain rule in reverse. Next, we introduce the normalized voltage U and normalized current W defined by

$$U(x, \omega) = \frac{V(x, \omega)}{\sqrt{Z_0(x)}} \quad (5.17a)$$

$$W(x, \omega) = I(x, \omega) \sqrt{Z_0(x)}. \quad (5.17b)$$

Differentiating (5.17) with respect to x yields

$$\frac{dU}{dx} = (Z_0)^{-1/2} \frac{dV}{dx} - \frac{V}{2} (Z_0)^{-3/2} \frac{dZ_0}{dx} \quad (5.18a)$$

$$\frac{dW}{dx} = \frac{dI}{dx} (Z_0)^{1/2} + \frac{I}{2} (Z_0)^{-1/2} \frac{dZ_0}{dx}. \quad (5.18b)$$

Using (5.16) and (5.17), we may write this as

$$\frac{dU}{dx} = i\omega W - \frac{U}{2} (Z_0)^{-1} \frac{dZ_0}{dx} \quad (5.19a)$$

$$\frac{dW}{dx} = i\omega U + \frac{W}{2} (Z_0)^{-1} \frac{dZ_0}{dx} \quad (5.19b)$$

There is a quantity on the right-hand sides of (5.19) that we will call $p(x)$, and it is defined as:

$$\frac{1}{2} (Z_0(x))^{-1} \frac{dZ_0}{dx}(x) = \frac{d}{dx} \log \sqrt{Z_0(x)} =: p(x). \quad (5.20)$$

Using the definition of $p(x)$ in (5.19), we may write

$$\frac{dU}{dx}(x, \omega) + p(x)U(x, \omega) = i\omega W(x, \omega) \quad (5.21a)$$

$$\frac{dW}{dx}(x, \omega) - p(x)W(x, \omega) = i\omega U(x, \omega) \quad (5.21b)$$

Now, by differentiating (5.21a) with respect to x and then using (5.21a-5.21b) to eliminate first-derivatives of U and W , we obtain the following second-order equation for U :

$$\frac{d^2U}{dx^2}(x, \omega) + [\omega^2 + p'(x) - p^2(x)] U(x, \omega) = 0. \quad (5.22)$$

Rewriting this in the more suggestive form

$$\left[\frac{d^2}{dx^2} + p'(x) - p^2(x) \right] U = -\omega^2 U,$$

it is clear that (5.22) is mathematically identical to the time-independent Schrödinger equation

$$\left[-\frac{\hbar^2}{2m} \frac{d^2}{dx^2} + V \right] \psi = E\psi.$$

The quantity $p'(x) - p^2(x)$ can be thought of as a potential $V(x)$, while $-\omega^2$ can be thought of as an energy eigenvalue E .

In what follows, we will specify an exponentially tapered impedance function $Z_0(x)$, which corresponds to a piecewise constant choice of $p(x)$. Then, borrowing scattering theory techniques from quantum mechanics, we will solve the reflection/transmission problem for (5.22) with our particular choice of $p(x)$. At this point, our discussion departs from that of Klemer and Sharpe. Their analysis of the scattering problem is valid only in the large ω regime.

5.1.3 Exponentially Tapered Line

We consider a transmission line with local characteristic impedance given by

$$Z_0(x) = \begin{cases} z_1 & x < 0 \\ \alpha^2 \exp(2\beta x) & 0 < x < l \\ z_2 & x > l \end{cases} \quad (5.23)$$

We say that the impedance is *matched* if $Z_0(x)$ is continuous at $x = 0$ and $x = l$, i.e., if $\alpha^2 = z_1$ and $\beta = (\log z_2/z_1)/2l$. For the above choice of $Z_0(x)$, we apply definition (5.20) and obtain the following expression for $p(x)$:

$$p(x) = \begin{cases} 0 & x < 0 \\ \beta & 0 < x < l \\ 0 & x > l \end{cases} \quad (5.24)$$

As promised, the exponentially tapered impedance profile (5.23) corresponds to a piecewise constant function p with zero derivative p' . Using (5.24) in (5.22) gives two equations: for $x < 0$ and $x > l$, we must find $U(x, \omega)$ that solves

$$\frac{d^2 U}{dx^2}(x, \omega) + \omega^2 U(x, \omega) = 0. \quad (5.25)$$

When $0 < x < l$, we must find $U(x, \omega)$ that solves

$$\frac{d^2 U}{dx^2}(x, \omega) + (\omega^2 - \beta^2)U(x, \omega) = 0. \quad (5.26)$$

Both equations (5.25-5.26) can be solved trivially using linear combinations of exponentials. For example, we may immediately write down the most general solution of (5.26):

$$U(x, \omega) = A(\omega) \exp(i\sqrt{\omega^2 - \beta^2}x) + B(\omega) \exp(-i\sqrt{\omega^2 - \beta^2}x). \quad (5.27)$$

This solution is valid as long as $\omega \neq \beta$. Here $A(\omega)$ and $B(\omega)$ are unknown amplitude coefficients. Without specifying further conditions on (5.25-5.26), we cannot obtain more information from this approach.

5.1.4 Scattering

Let us study the (forward) scattering problem for (5.25-5.26). We imagine a situation in which we send an incident wave from $x = -\infty$ towards the beginning of the tapered section at $x = 0$. The incident wave interacts with the inhomogeneity located between $x = 0$ and $x = l$. Part of the incident wave is *transmitted* through the inhomogeneity and propagates from $x = l$ outward to $x = +\infty$. The remaining part of the incident wave is *reflected* and propagates backward from $x = 0$ to $x = -\infty$.

Mathematically, we represent this picture by writing, for $x < 0$,

$$U(x, \omega) = a_1(\omega) \exp(i\omega x) + b_1(\omega) \exp(-i\omega x), \quad (5.28)$$

and for $x > l$,

$$U(x, \omega) = c_1(\omega) \exp(i\omega x). \quad (5.29)$$

Here $a_1(\omega)$ is the amplitude of the incident wave, $b_1(\omega)$ is the amplitude of the reflected wave, and $c_1(\omega)$ is the amplitude of the transmitted wave. In the interior, inhomogeneous region $0 < x < l$, we have (5.27) as before. We summarize this in one equation:

$$U(x, \omega) = \begin{cases} a_1(\omega) \exp(i\omega x) + b_1(\omega) \exp(-i\omega x) & x < 0 \\ A(\omega) \exp(i\beta r x) + B(\omega) \exp(-i\beta r x) & 0 < x < l \\ c_1(\omega) \exp(i\omega x) & x > l \end{cases} \quad (5.30)$$

Here we have used

$$r = \sqrt{\frac{\omega^2}{\beta^2} - 1}. \quad (5.31)$$

Now using (5.21a), we may write down $W(x, \omega)$ in each of the three regions:

$$W(x, \omega) = \begin{cases} a_1(\omega) \exp(i\omega x) - b_1(\omega) \exp(-i\omega x) & x < 0 \\ \beta A(\omega) \omega^{-1} (r - i) \exp(i\beta r x) - \beta B(\omega) \omega^{-1} (r + i) \exp(-i\beta r x) & 0 < x < l \\ c_1(\omega) \exp(i\omega x) & x > l \end{cases} \quad (5.32)$$

For this scattering problem, we are interested in obtaining relationships between the five quantities a_1 , b_1 , c_1 , A , and B . In particular, we seek a closed form expression for the *reflection coefficient*

$$\rho = \left\| \frac{b_1}{a_1} \right\|$$

and the *transmission coefficient*

$$\tau = \left\| \frac{c_1}{a_1} \right\|.$$

Because of the relation $\rho^2 + \tau^2 = 1$, we need only determine one of the two quantities.

Through definition (5.17), the functions U and W determine, respectively, the voltage V and current I in the transmission line. Voltage and current are physically measurable quantities, and therefore V and I must be continuous at $x = 0$ and $x = l$.

To carry out this analysis in the greatest generality, we would have to assume that $Z_0(x)$, given for example by (5.23), is discontinuous at $x = 0$ and $x = l$.

Therefore, in general, we would have to use (5.30) and (5.32) together with (5.23) to write down expressions for V and I in each of the three regions. Then, enforcing continuity of V and I at the boundaries $x = 0$ and $x = l$ would yield four relations between the five unknown amplitude coefficients, and exact expressions for the reflection and transmission coefficients would quickly follow.

5.1.5 Reflection Coefficient for Matched Case

or the *matched* case, we know that Z_0 is continuous at $x = 0$ and $x = l$. In this case, both U and W are also continuous at $x = 0$ and $x = l$.

Enforcing continuity of U and W at $x = 0$ gives

$$\begin{aligned} a_1 + b_1 &= A + B \\ a_1 - b_1 &= \beta\omega^{-1}A(r - i) - \beta\omega^{-1}B(r + i). \end{aligned}$$

Combining these equations, we obtain

$$\frac{b_1}{a_1} = \frac{1 + i\beta\omega^{-1} - \beta\omega^{-1}rq}{1 - i\beta\omega^{-1} + \beta\omega^{-1}rq},$$

where

$$q = \frac{A - B}{A + B}.$$

Then, enforcing continuity of U and W at $x = l$ gives

$$\begin{aligned} A \exp(i\beta rl) + B \exp(-i\beta rl) &= c_1 \exp(i\omega l) \\ \beta A \omega^{-1}(r - i) \exp(i\beta rl) - \beta B \omega^{-1}(r + i) \exp(-i\beta rl) &= c_1 \exp(i\omega l) \end{aligned}$$

Combining these equations, we obtain the following relation between A and B :

$$A = -B \frac{1 + \beta\omega^{-1}(r + i)}{1 - \beta\omega^{-1}(r - i)} \exp(-2i\beta rl).$$

We may then substitute this expression into q and then into b_1/a_1 . Let

$$y = \frac{\omega}{\beta}.$$

Then the final result is, for $y > 1$,

$$\left\| \frac{b_1}{a_1} \right\|^2 = \frac{-1 + \cos(2\beta l \sqrt{y^2 - 1})}{1 - 2y^2 + \cos(2\beta l \sqrt{y^2 - 1})}, \quad (5.33)$$

while for $y < 1$, the final result is

$$\left\| \frac{b_1}{a_1} \right\|^2 = \frac{-1 + \cosh(2\beta l \sqrt{1 - y^2})}{1 - 2y^2 + \cosh(2\beta l \sqrt{1 - y^2})}. \quad (5.34)$$

We note that the reflection coefficient is indeed continuous at $y = 1$ and the limit there is

$$\lim_{y \rightarrow 1} \left\| \frac{b_1}{a_1} \right\|^2 = \frac{l^2 \omega^2}{1 + l^2 \omega^2}. \quad (5.35)$$

For extremely low and extremely high frequencies, we have the limits

$$\begin{aligned} \lim_{y \rightarrow 0} \left\| \frac{b_1}{a_1} \right\|^2 &= \tanh^2(l\beta) \\ \lim_{y \rightarrow \infty} \left\| \frac{b_1}{a_1} \right\|^2 &= 0 \end{aligned}$$

This confirms Klemer and Sharpe's result that sufficiently large frequencies are, for all practical purposes, completely transmitted.

Qualitatively, the shape of $\|b_1/a_1\|^2$ is the same regardless of the scaling parameter $2\beta l$. Quantitatively, this parameter is crucial towards determining whether there is appreciable reflection for sufficiently low frequencies. For example, when $2\beta l = O(1)$, we find that reflection of sufficiently low-frequency incoming signals is significant:

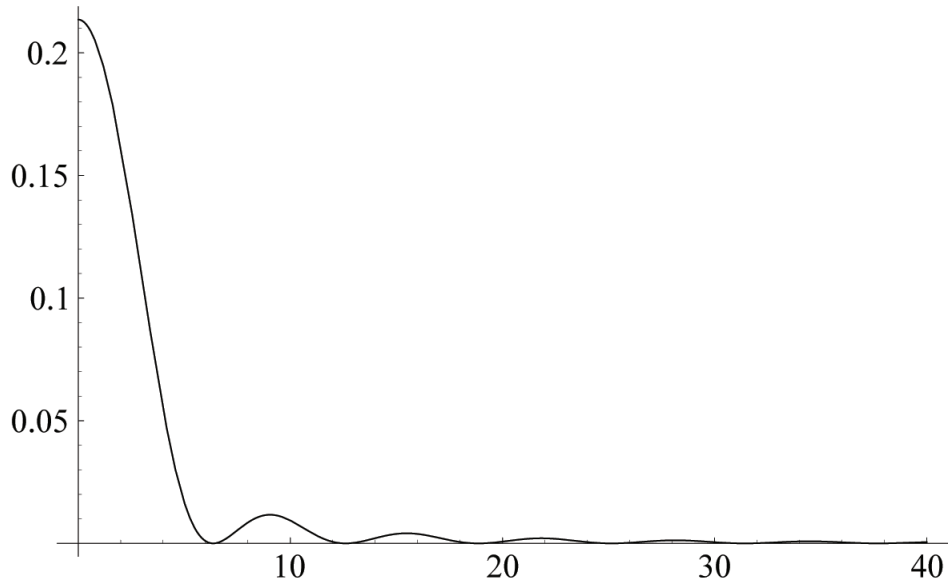


Figure 5.2: Reflection coefficient as a function of the ratio ω/β , for $2\beta l = 1$. Note that for sufficiently low frequencies ω , more than 15% of the input signal is reflected.

However, when $2\beta l$ is small, reflection is negligible for all frequencies. For example, when $2\beta l = O(10^{-6})$, we have

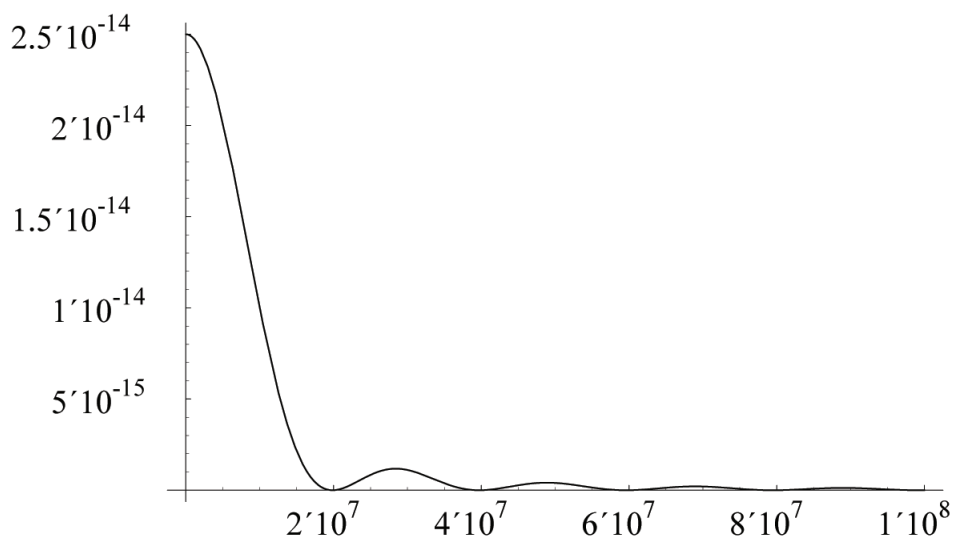


Figure 5.3: Reflection coefficient as a function of ω/β , for $2\beta l = 10^{-6.5}$. Note that the maximum value of the reflection coefficient is less than 10^{-13} so, for all practical purposes, we have 100% transmission of the input signal.

5.2 Two-Dimensional Transmission Lattice

In this section we examine the same approach for the case of 2D inhomogenous lattice shown in figure 5.4.

5.2.1 Continuum Model

We begin with the continuum model of the lattice (see chapter 4), neglecting the dispersion:

$$LCV_{tt} = \nabla^2 V - \frac{\nabla V \cdot \nabla L}{L} \quad (5.36)$$

or in fourier domain:

$$-\omega^2 \tau^2 V = \nabla^2 V - \frac{\nabla V \cdot \nabla L}{L} \quad (5.37)$$

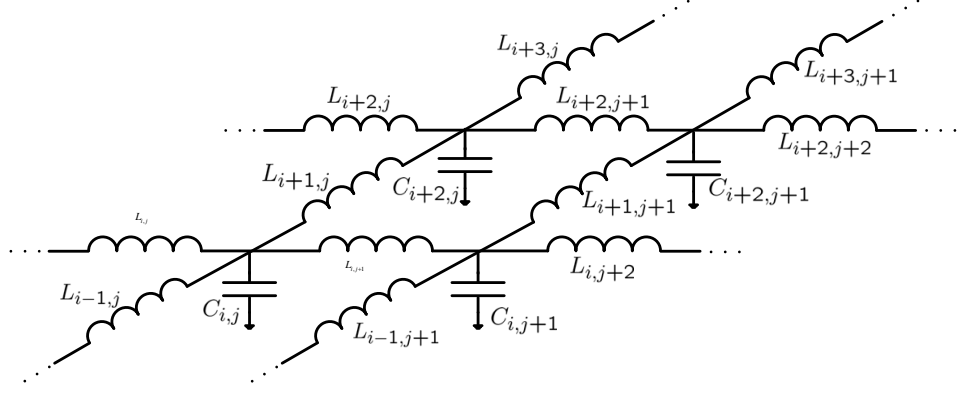


Figure 5.4: 1D nonuniform linear transmission line

Now we examine the same change of variable for the case of 2D described by (5.37):

$$u = \frac{V}{\sqrt{Z_0}} \implies \nabla u = \frac{\nabla V}{\sqrt{Z_0}} - \frac{1}{2}(Z_0)^{-3/2}(\nabla Z_0)V \quad (5.38a)$$

$$w = I\sqrt{Z_0} \implies \nabla w = \nabla I\sqrt{Z_0} + \frac{1}{2}(Z_0)^{-1/2}(\nabla Z_0)I \quad (5.38b)$$

by defining p as

$$\vec{p} = \nabla(\ln \sqrt{Z_0}) \quad (5.39)$$

we will have:

$$\nabla u = \frac{\nabla V}{\sqrt{Z_0}} - u \vec{p} \quad (5.40)$$

by taking the divergence of the above and substituting into (5.37), we will have:

$$(\nabla^2 + \vec{p} \cdot \vec{p} + \nabla \cdot \vec{p} - \frac{\nabla L}{L} \cdot \vec{p})u = -\omega^2 \tau^2 u + \left(\frac{\nabla L}{L} - 2\vec{p}\right) \cdot \nabla u \quad (5.41)$$

5.2.2 Electrical Funnel

The funnel is a 2D lattice with constant τ and variable Z_0 . the first choice of funnel is:

$$L(x, y) = B \exp(\lambda xy) \quad (5.42a)$$

$$C(x, y) = \frac{\tau^2}{B} \exp(-\lambda xy) \quad (5.42b)$$

one could show that these choices of inductors and capacitors will result in:

$$(\nabla^2 - \frac{\lambda^2}{4}(x^2 + y^2))u = -\omega^2 \tau^2 u \quad (5.43)$$

this equation has solutions in Hermitian polynomial format; however the difficulty is that after we found the u and V , we should do a reverse fourier transform to have the voltage in time domain, and the solution of (5.43) does not have a simple form. Another choice of inductors and capacitors is:

$$L(x, y) = B \exp(\lambda_1 x + \lambda_2 y) \quad (5.44a)$$

$$C(x, y) = \frac{\tau^2}{B} \exp(-\lambda_1 x - \lambda_2 y) \quad (5.44b)$$

again, by finding \vec{p} and substituting it in (5.41), we will have:

$$(\nabla^2 + \frac{1}{4}(\lambda_1^2 + \lambda_2^2))u = -\omega^2 \tau^2 u \quad (5.45)$$

this equation is a well-known Helmholtz differential equation.

5.2.3 Electrical Lens

the funnel is a 2D lattice with variable τ and constant Z_0 . unfortunately, the change of variables described by (5.38) will not eliminate the τ from the equation. To solve

this problem, we are looking for transform like:

$$x = F(x', y') \quad (5.46a)$$

$$y = G(x', y') \quad (5.46b)$$

so we will have:

$$\frac{\partial V}{\partial x'} = \frac{\partial V}{\partial x} \frac{\partial F}{\partial x'} + \frac{\partial V}{\partial y} \frac{\partial G}{\partial x'} \quad (5.47a)$$

$$\frac{\partial V}{\partial y'} = \frac{\partial V}{\partial x} \frac{\partial F}{\partial y'} + \frac{\partial V}{\partial y} \frac{\partial G}{\partial y'} \quad (5.47b)$$

and similarly for the second derivatives,

$$\frac{\partial^2 V}{\partial x'^2} = \frac{\partial^2 V}{\partial x^2} \left(\frac{\partial F}{\partial x'}\right)^2 + \frac{\partial V}{\partial x} \frac{\partial^2 F}{\partial x'^2} + \frac{\partial^2 V}{\partial y^2} \left(\frac{\partial G}{\partial x'}\right)^2 + \frac{\partial V}{\partial y} \frac{\partial^2 G}{\partial x'^2} \quad (5.48a)$$

$$\frac{\partial^2 V}{\partial y'^2} = \frac{\partial^2 V}{\partial x^2} \left(\frac{\partial F}{\partial y'}\right)^2 + \frac{\partial V}{\partial x} \frac{\partial^2 F}{\partial y'^2} + \frac{\partial^2 V}{\partial y^2} \left(\frac{\partial G}{\partial y'}\right)^2 + \frac{\partial V}{\partial y} \frac{\partial^2 G}{\partial y'^2} \quad (5.48b)$$

in order to compensate the time dependence in the equation (5.37) and reduce it to the Helmholtz equation, one could show that, we must have:

$$\left(\frac{\partial F}{\partial x'}\right)^2 + \left(\frac{\partial F}{\partial y'}\right)^2 = \tau^2 \quad (5.49a)$$

$$\left(\frac{\partial G}{\partial x'}\right)^2 + \left(\frac{\partial G}{\partial y'}\right)^2 = \tau^2 \quad (5.49b)$$

$$\frac{\partial^2 F}{\partial x'^2} + \frac{\partial^2 F}{\partial y'^2} = \nabla^2 F = \frac{L_x}{L} \quad (5.49c)$$

$$\frac{\partial^2 G}{\partial x'^2} + \frac{\partial^2 G}{\partial y'^2} = \nabla^2 G = \frac{L_y}{L} \quad (5.49d)$$

the first two conditions, will result in an equation similar to (5.43) and if all four hold, we will get a simple Helmholtz equation. Equations (5.49) are similar to *Eikonal* equations in Geometric mechanics and we might be able to solve them with similar techniques; However, we will develop a simpler method to attack this problem in chapter 9 using optical ideas. Now we are ready to discuss the application of the theory of wave propagation in one and two dimensional lattices in chapters 6 and 7.

Chapter 6

Extremely Wideband Signal Generation and Processing

In this chapter, we first show a soliton line on a conventional silicon technology, which can achieve very narrow (soliton) pulses with a bandwidth in excess of the cut-off frequency, f_T , of the fastest transistor available in the process technology.

Another possible application of NLTLs is pulse sharpening for the more traditional non-return-to-zero (NRZ) data transmission in digital circuits by improving the edges of the pulses. Improving the transitions by shrinking the rise and fall times of pulses can be useful in other applications, such as high-speed sampling and timing systems. Non-linear transmission lines' (NLTLs) sharpening of either the rising or the falling edge of a pulse has been demonstrated on a GaAs technology [73]. However, to the best of our knowledge, to this date there has been no demonstration of simultaneous reduction of both rise and fall times in an NLTL. Neither are we aware of any demonstration of such NLTLs in silicon-based CMOS process technologies. In the second part of this chapter, we demonstrate that using a favorable characteristic of MOS varactors, which leads to a different kind of non-linearity, we can improve both the rise and fall times, simultaneously. This is not possible with the nonlinear elements commonly used in the NLTLs (*e.g.*, reverse bias PN junctions). Neither can it be done using transistors, as they are limited by their unity gain frequency, f_T .

Here, we introduce two different types of non-linear transmission lines to generate narrow pulses and to sharpen pulse transitions, respectively, and we show the exper-

imental results verifying the agreement between the theory and the measurement.

6.1 Pulse Narrowing Non-Linear Transmission Line

As shown in equation 3.9, the traveling wave solution of NLTL with varactor model of $C(V) = C_0(1 - bV)$ equation can be written as:

$$V(x, t) = \frac{3(\nu^2 - \nu_0^2)}{b\nu^2} \operatorname{sech}^2 \left[\frac{\sqrt{3(\nu^2 - \nu_0^2)}}{\nu_0 h} (x - \nu t) \right]. \quad (6.1)$$

where ν is the propagation velocity of the pulse and $\nu_0 = 1/\sqrt{LC_0}$. In chapter 3, we proved mathematically that 6.1 is the only physically meaningful traveling wave solution that maintains its shape while propagating through NLTL. This solution is shown in Figure 6.1 for three different values of L and C, and hence different h . Note that this solution is not a function of the input waveform, and thus any arbitrary input will eventually turns into 6.1, if it goes through a line which is long enough.

As can be seen from 6.1, the peak amplitude is a function of the velocity. Defining an effective capacitance, C_{eff} , so that $\nu = 1/\sqrt{LC_{eff}}$, the pulse height is given by:

$$V_{max} = \frac{3}{b} \cdot \frac{\nu^2 - \nu_0^2}{\nu^2} = \frac{3}{b} \cdot \left(1 - \frac{C_{eff}}{C_0}\right) \quad (6.2)$$

Using 6.2, we can relate C_{eff} to an effective voltage V_{eff} . It is straightforward to show that

$$V_{eff} = \frac{V_{max}}{3} \quad (6.3)$$

So it is the capacitance at one-third the peak amplitude, that determines the effective propagation velocity. Using these relationships, we can easily calculate the half-height width of the pulse to be:

$$W \approx \frac{h}{\nu} \frac{\nu_0}{\sqrt{(\nu^2 - \nu_0^2)}} \quad (6.4)$$

A few important observations are:

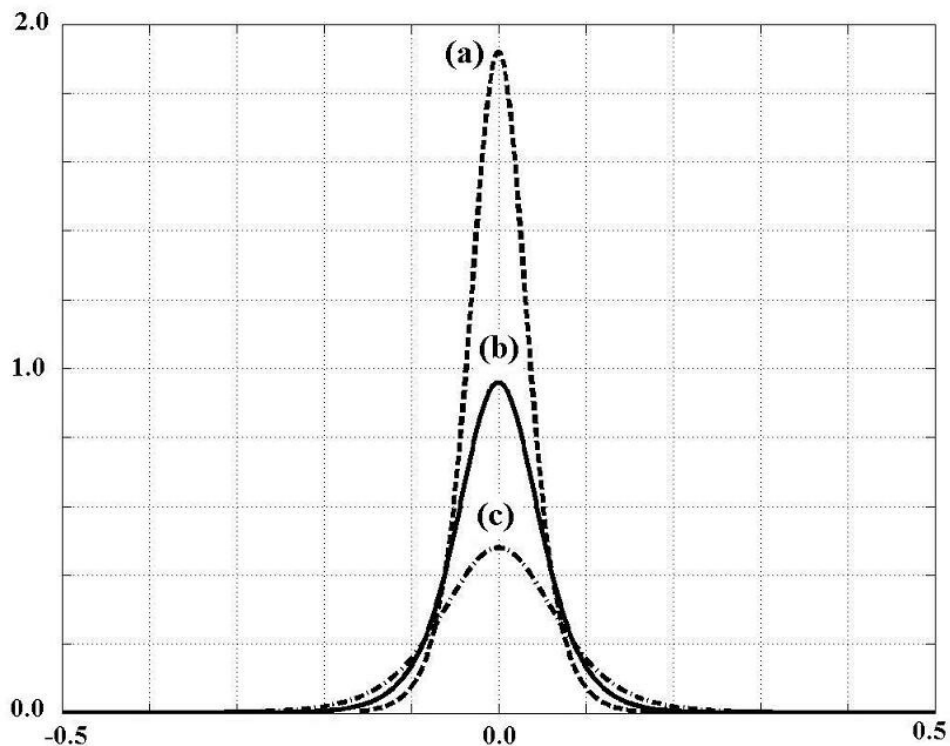


Figure 6.1: Three normalized soliton shapes for different values of L and C (a) $L=1\text{nH}$ and $C=1\text{nF}$ (b) $L=2\text{nH}$ and $C=2\text{nF}$ (c) $L=4\text{nH}$ and $C=4\text{nF}$

- the velocity of the solitary wave increases with its amplitude,
- pulse width decreases with increasing pulse velocity,
- the width shrinks for higher amplitudes,
- the sign of solution depends on the sign of non-linearity factor, b , *i.e.* for a capacitor with a positive voltage dependence (*e.g.*, an nMOS varactor in accumulation mode) we have:

$$C(V) = C_0(1 + bV) \quad (6.5)$$

resulting in upsidedown pulses.

Based on these results, to achieve large-amplitude narrow pulses, inductance and capacitance of the NLTL must be as small as possible, and non-linearity factor, b ,

should be large enough to compensate the dispersion of the line.

It is also important to know the characteristic impedance of these lines (for impedance matching, etc.). As in a NLTL, the capacitance is a function of voltage, we can only define an effective semi-empirical value for the characteristic impedance. Simulation results indicate that one can approximate Z_{eff} using the capacitance at V_{eff} defined in 6.3 , i.e.:

$$Z_{eff} = \sqrt{\frac{L}{C(V_{eff})}} \quad (6.6)$$

6.1.1 Intuitive Explanation

As can be seen, in a weakly dispersive and non-linear transmission line, the non-linearity can counteract the normally present dispersive properties of the line maintaining solitary waves that propagate without dispersion. This behavior can be explained using the following intuitive argument.

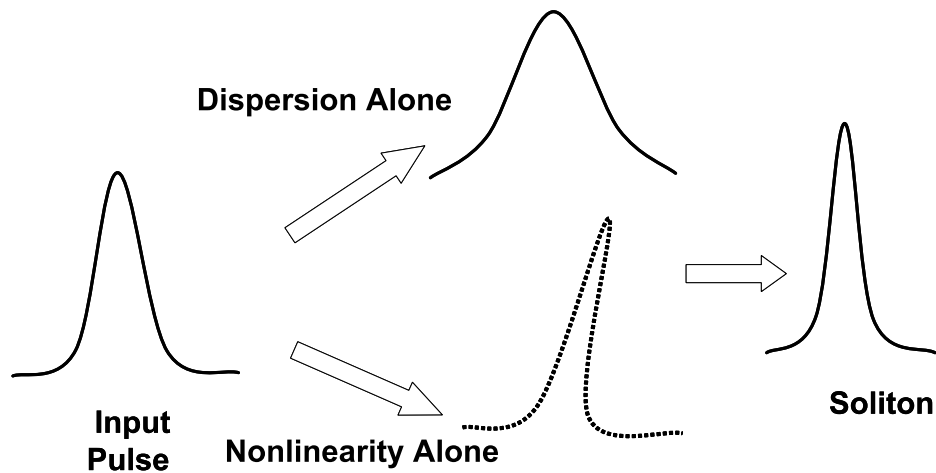


Figure 6.2: Dispersion and non-linear effects in the NLTL

The instantaneous propagation velocity at any given point in time and space is

given by $\nu = 1/\sqrt{LC}$. In the presence of a non-linear capacitor with a characteristic given by $C(V) = C_0(1 - bV)$, the instantaneous capacitance is smaller for higher voltages. Therefore, the points closer to the crest of the voltage waveform experience a faster propagation velocity and produce a shock-wave front, due to the nonlinearity, as shown symbolically in the upper part of Figure 6.2. Note that this is not a real waveform and more a fictitious representation of how each point on the curve tends to evolve. On the other hand, dispersion of the line causes the waveform to spread out, as shown in the lower half of Figure 6.2. For a proper non-linearity, these two effects can cancel each other out resulting in a pulse which can propagate without experiencing dispersion or nonlinearity.

6.1.2 Pulse Degeneration Problem

As mentioned in chapter 3, one problem in pulse narrowing NLTLs is that if the input pulse is wider than a certain minimum related to the natural pulse width of the line in 6.4, the line is incapable of concentrating all that energy into one pulse and instead the input pulse degenerates into multiple soliton pulses, as shown in the simulated upper waveforms of Figure 6.3. This is an undesirable effect that cannot be avoided in a standard line. We can solve this problem by using gradually scaled non-linear transmission lines [73].

We notice that the characteristic pulse width of the line is controlled by the node spacing, h , and the propagation velocity, ν , which is in turn controlled by L and C . Thus, we use a gradual line consisting of several segments that are gradually scaled to have smaller characteristic pulse width, as shown in Figure 6.4.

The first few segments have the widest characteristic pulse, meaning that their output is wider and has smaller amplitude. As a result, the input pulse will cause just one pulse at the output of these segments. The following segments have a narrower response and the last segment has the narrowest one. This will guarantee the gradual narrowing of the pulses and avoids degeneration. Each segment has to be long enough so that the pulse can reach the segment's steady-state response before entering the

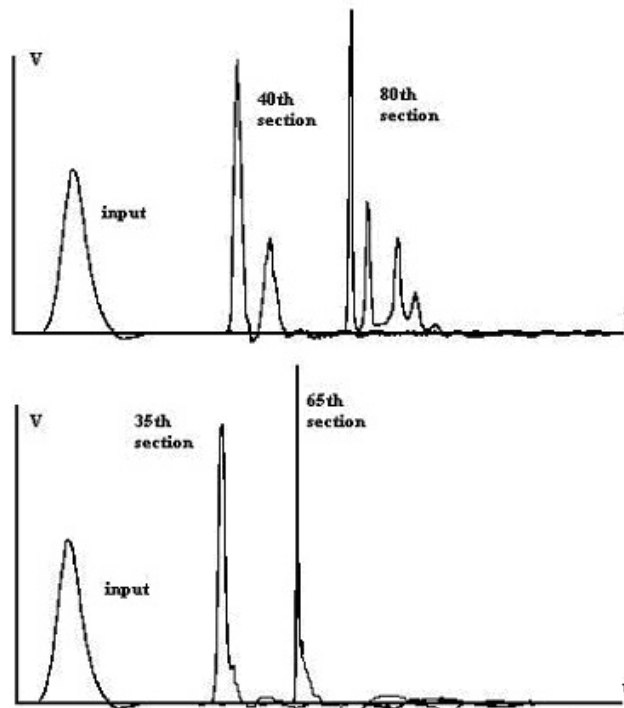


Figure 6.3: Output waveforms of the normal and gradual soliton line

next segment.

One design consideration is that the characteristic impedance of each segment matches those of the adjacent segments to avoid reflections. This requires the same scaling factor for both L and C , so that their ratio remains constant.

The mathematical treatment of this inhomogeneous nonlinear transmission line was studied in section . The waveforms of this gradually scaled NLTL are shown in the lower part of Figure 6.3, demonstrating the effectiveness of this technique.

6.2 Edge Sharpening Line

It is possible to design NLTLs to sharpen the pulse transitions. This is particularly useful for digital transmission such as non-return to zero (NRZ) data. Unfortunately,

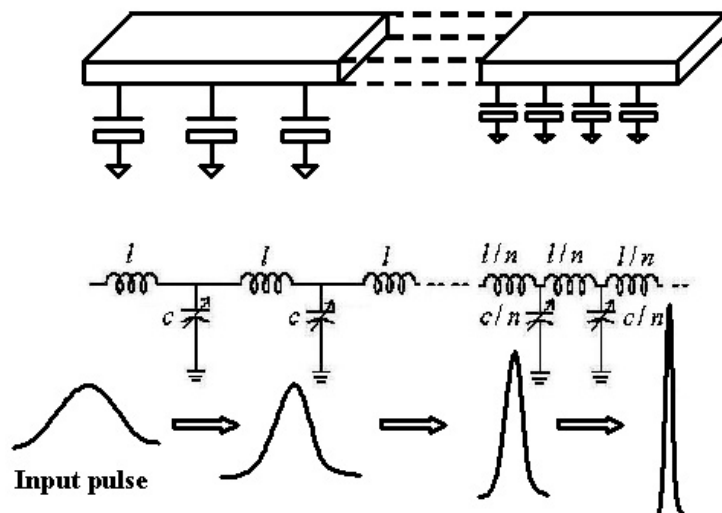


Figure 6.4: Schematic of the gradually scaled non-linear transmission line

all the efforts in the past [73] have resulted in sharpening of only one of the rising and falling edges. This, however, has very little practical value, as both transitions are equally important in common NRZ digital systems. This problem can be traced back to the monotonic dependence of the non-linear capacitive elements used in NLTL on the voltage (*e.g.*, reverse biased PN junction, or the ideal behavior of 6.5). Fortunately, CMOS processes offer different characteristics for non-linear capacitors that can be exploited to achieve simultaneous edge sharpening for both rising and falling edges. More specifically, accumulation mode MOS varactors (shown in Figure 6.5) (an nMOS capacitor in an n-well) [35] offer non-monotonic voltage dependence. Particularly, the secondary reduction of capacitance shown in Figure 6.6 due to poly-silicon depletion [36][37] and short-channel charge quantization [37] effects can be used for edge sharpening.

6.2.1 Intuitive Explanation

Figure 6.7 shows symbolically how one can use the behavior of Figure 6.6 to sharpen both edges.

First, let us focus on the rise-time reduction. Consider the rising edge shown in the

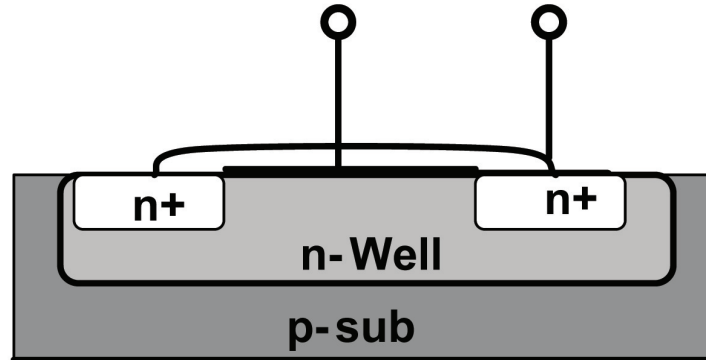


Figure 6.5: Schematic of an accumulation mode MOS varactor

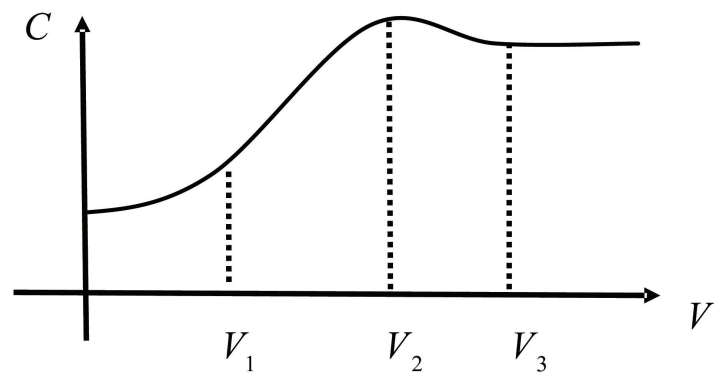


Figure 6.6: Capacitance versus voltage for a MOSVAR

upper part of Figure 6.7. Initially the voltage is low, which corresponds to a smaller capacitance per Figure 6.6, and hence a faster instantaneous propagation velocity for the lower end of the pulse. As the voltage goes up, the capacitance increases, resulting in a decrease in the instantaneous propagation velocity. This pushes the lower end of the transition forward in time and results in sharpening of the rising edge. This effect is symbolically shown in the fictitious middle waveform of Figure 6.7. The fall time reduction can be explained using the lower part of Figure 6.7. This is where the non-monotonic behavior of Figure 6.6 plays its role. The upper part of the transition (voltages above V_2) will be accelerated due to the reduction of the capacitance and will create an advancing front, as symbolically shown in the middle waveform of Figure 6.7. The lower capacitance at the very low voltages can generate a leading tail, which will be partially dissipated by the line. The weak reduction

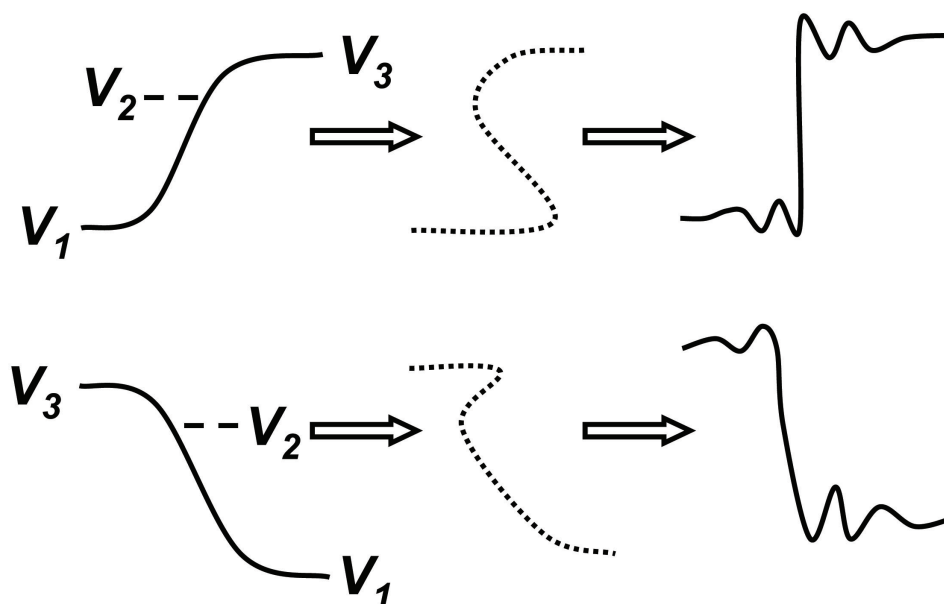


Figure 6.7: How rise and fall time vary within the NLTL

in capacitance from V_2 to V_3 versus reduction from V_1 to V_2 results in mismatched rise/fall time as can be seen in Figure 6.7.

While the above explanation based on a simplified memory-less description of the line provides a basic intuition for its operation, a complete description can only be obtained by solving the differential equation governing the line to account for the memory of the system *. Our numerical solution of this equation, also confirms that as long as the input voltage range exceeds voltages, V_1 and V_3 , for a range of L 's and C 's, the line sharpens both rising and falling edges, simultaneously.

It may also be possible to achieve a symmetrical wave form by:

- Using an n-type and a p-type MOSVAR in parallel to create a symmetrical $C(V)$ curve. The problem of this method is that a p-type MOSVAR is not as fast as n-type MOSVAR therefore the frequency response of the line would be limited to the frequency response of the p-type MOSVARs.

*We hypothesize that other dynamic effects in the MOS varactor may also help edge sharpening, e.g., the processes of charge being attracted from the n+ diffusions to the channel and repelling them are not exact inverses of each other over short time intervals. Some of the repelled accumulation charges will be absorbed inside the well. This changes the response time of the capacitor and keeps it higher for a longer period of time for the falling edge.

- Using two n-type MOSVAR at each node, as shown in Figure 6.8. This way, we can have a symmetrical $C(V)$ curve, however the capacitance of each node would be twice as large which limits the cut-off frequency of the line by a factor of $\sqrt{2}$. Another limitation of this method is the additional parasitic capacitance to the substrate that may lower the effective non-linearity factor, b , of the capacitors.

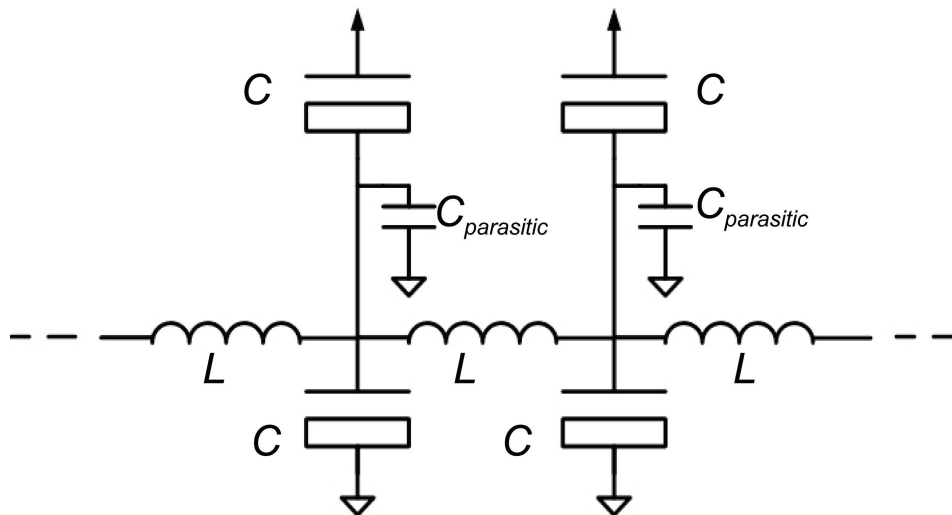


Figure 6.8: A proposed NLTL for symmetrical edge sharpening

In this work, the goal was to achieve the minimum rise time while decreasing the fall time at the same time, so we used a single capacitor at each node. For other applications with different objectives one of these alternative methods may be preferred.

6.3 The Effect of Loss

Figure 6.9 shows a simple model of a lossy non-linear transmission line.

By applying KCL at node n , whose voltage with respect to ground is V_n , and applying KVL across the two branches connected to this node, one can easily show that voltages of adjacent nodes on this NLTL are related via:

$$V_{n-1} - 2V_n + V_{n+1} = \ell \frac{d}{dt}(I_{n-1} - I_n) + r(I_{n-1} - I_n) \quad (6.7)$$

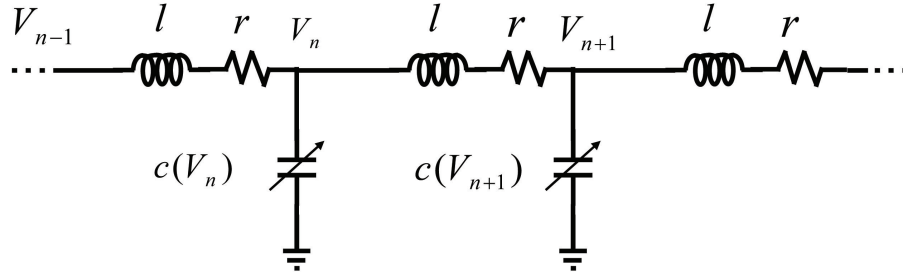


Figure 6.9: Simple model of a lossy non-linear transmission line with series resistor

where r is the series resistance of each section. Let $L = \ell/h$, $C(V) = c(V)/h$, and $R = r/h$ be, respectively, the inductance, capacitance, and resistance per unit length. By applying techniques shown in chapter 3, a continuous partial differential equation can be obtained from 6.7:

$$\frac{\partial^2 V}{\partial x^2} + \frac{h^2}{12} \frac{\partial^4 V}{\partial x^4} = L \frac{\partial}{\partial t} \left[C(V) \frac{\partial V}{\partial t} \right] + RC(V) \frac{\partial V}{\partial t} \quad (6.8)$$

Unfortunately, we could not find an analytical solution for 6.8 and had to use numerical methods to solve it.

Other model for the loss of the transmission line is shown in figure 6.10. In this case one can show that the governing equation of the line is:

$$\frac{\partial^2 V}{\partial t^2} - b \frac{\partial^2 V^2}{\partial t^2} = \nu_0^2 \left[\frac{\partial^2 V}{\partial x^2} + \frac{1}{12} \frac{\partial^4 V}{\partial x^4} \right] + \frac{R}{L} \left[\frac{\partial^2 V}{\partial x^2} - b \frac{\partial^2 V^2}{\partial x^2} \right] \quad (6.9)$$

which can be reduced to Burgers equation [74].

In both models, the numerical solution of the governing equations shows that loss has an effect similar to the dispersion, meaning that loss causes the waveform to spread out, so in order to have a soliton pulse in a lossy non-linear transmission line, non-linearity should be strong enough to cancel out both dispersion and loss.

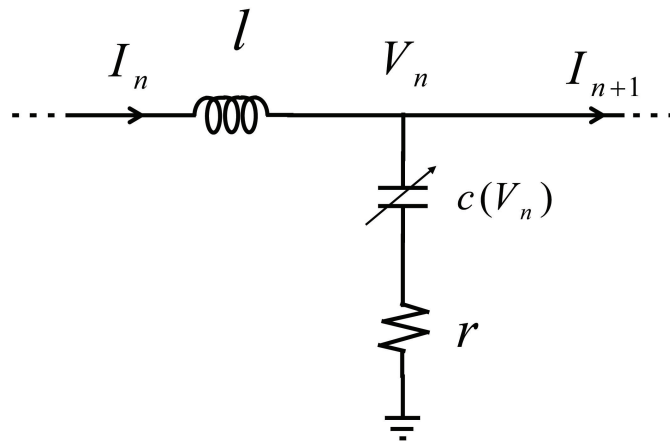


Figure 6.10: Simple model of a lossy non-linear transmission line with parallel resistor

6.4 Simulations

We have designed one edge sharpening and two pulse narrowing NLTLs with different tapering factors using the accumulation-mode MOS varactors and metal micro-strip transmission lines in a $0.18\ \mu\text{m}$ BiCMOS process. Figure 6.11 shows the measured characteristic of the accumulation-mode MOSVAR used in this design. All the capacitors have similar C-V characteristics; however, we used different capacitances along the line in order to build a gradually scaled NLTL.

To achieve the lowest pulse width in the pulse narrowing lines or the shortest rise and fall times in the edge sharpening line, it is necessary to carefully select the dc level and the voltage swing. In general, this may be an additional constraint in system design since it will require additional dc level shifting and amplification or attenuation to adjust the input levels. Nonetheless, this level of signal conditioning is easily achieved in today's integrated circuits. The dc level and the voltage swing for each application is mentioned in the following sections. All three lines consist of one hundred capacitors and one hundred inductors. We simulated the passive transmission lines in Sonnet [66] and the complete NLTL in ADS [67]. Next, we will discuss the details specific to each kind of lines separately.

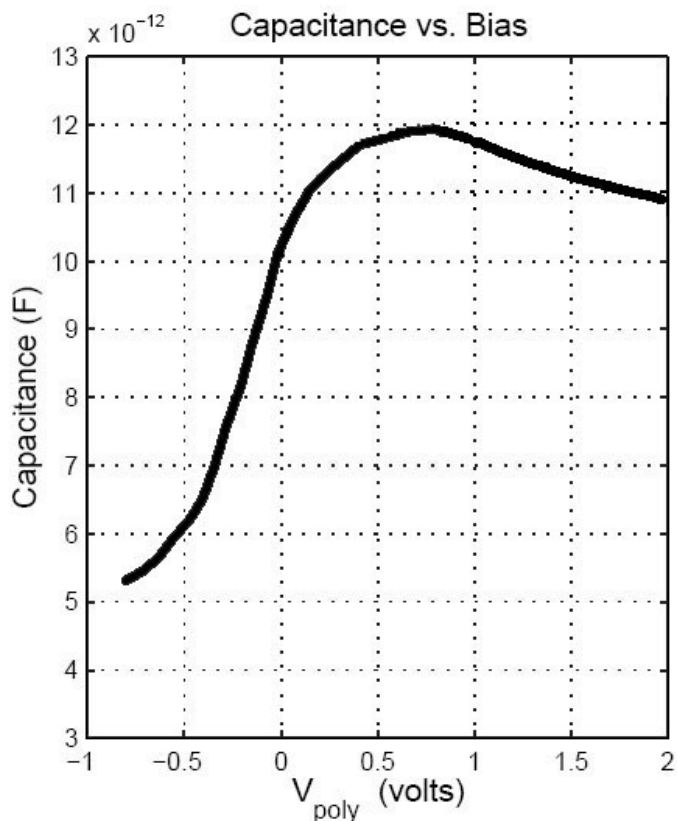


Figure 6.11: Measured characteristic of MOSVAR used in the line

6.4.1 Pulse Narrowing Line

For pulse narrowing lines, we would like to have the maximum change in the capacitance with voltage. Thus, we chose the baseline dc bias point at 0.8V which corresponds to the maximum capacitance point, and applied negative input pulses from this dc level. For a typical pulse amplitude of 1V, the effective non-linearity factor, b in $C(V) = C_0(1 - bV)$ is around $0.5V^{-1}$. As we explained in Section 6.1.2, the lines are not continuously scaled, but consist of several segments with constant values of inductors and capacitors within a segment. (However it turns out that a continuous scaling of the line is preferable because of internal reflections between different segments of the line due to mismatch). The inductances and capacitances within each segment are lower than those of the previous segment. One of the lines consists of three different segments and the other of four. The results reported in this

Section and Section 6.5 are those associated with the four-segment line which has a smaller output pulse width. The lines are designed in such a way that the characteristic pulse width of each segment (given by equation 6.4) is half that of the previous segment so the line can at least compress the input pulse by a factor of sixteen without degenerating into multiple pulses. The simulated output waveform of the line to a 65ps wide input pulse is shown in Figure 6.12. The simulation predicts that this silicon-based NLTL can produce negative pulses as narrow as 2.5ps (half amplitude width) with a 0.8V amplitude at the output. It is noteworthy that transistors in this process are incapable of producing pulses nearly as narrow as those generated by the NLTL.

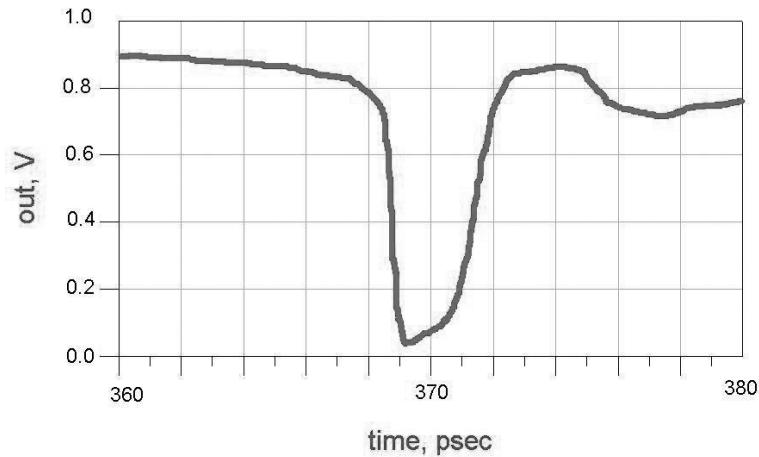


Figure 6.12: Simulated output waveform of the pulse narrowing line using ADS

6.4.2 Edge Sharpening Line

As we showed in the Section 6.2, to build an edge sharpening line we need take advantage of the non monotonic C-V behavior exemplified by the secondary reduction in the capacitance, as shown in Figure 6.11. Computer simulations show the best bias point and voltage swing are around -0.25V and 2V at the input, respectively. Although these levels led to the best achievable improvement in the rise and fall times,

the line still enhances the rising and falling edges for input signal voltage swings between 1.5V and 2V. Figure 6.13 shows the simulated input and output waveforms of this line. The output pulses exhibit reduced rise and fall times of 1.5ps and 20ps, respectively. The rise and fall times of the output pulses are different because of the asymmetrical behavior of the non-linear element for two different edges. We have also simulated this line with a pseudo-random data source and verified its edge sharpening functionality for any arbitrary data sequence [†].

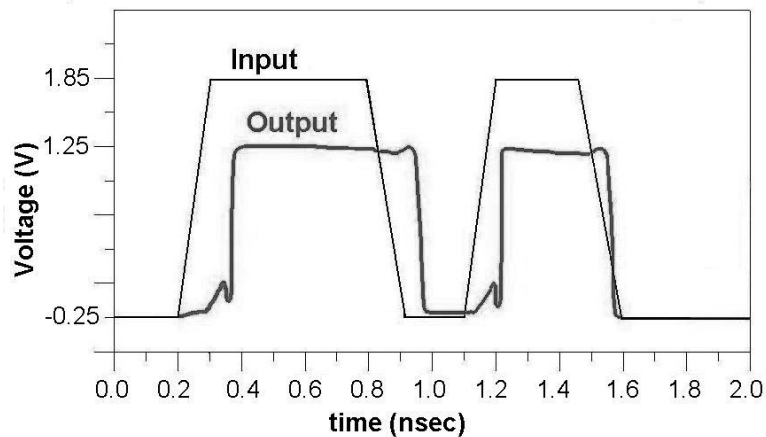


Figure 6.13: Simulated input and scaled output waveforms of the edge sharpening line using ADS

Unfortunately in this line, we cannot fully control the characteristic impedance of the lines because we have to pick the lowest capacitance and inductance -limited by the parasitic elements- to obtain that maximum improvement in the rise and fall times. This will allow us to maximize the cut-off frequency of the line. However, it is not possible to build very small non linear capacitors, because if we shrink the size of the accumulation-mode MOSVARs the effect of the parasitic capacitors becomes more important. These parasitic capacitors are voltage independent, hence linear, and will result in an effective reduction of the nonlinearity factor, b . In this design,

[†]There seems to be some data dependant delay due to the non-linear behavior of the lines in the simulations (See Fig. 13). This could have some implications for the data dependant jitter in the lines, which merits further studies.

the effective input impedance of the edge sharpening line is around 20Ω gradually scales to 50Ω at the output. So the input reflection coefficient of the line is roughly 0.4. We must take this effect into account to be able to match the simulation and the measurement results.

6.5 Experimental Results

All three lines were fabricated in a $0.18\mu\text{m}$ BiCMOS technology. Figure 6.14 shows a chip micro photograph. We use RF probes to apply input to the line and to measure its output waveform. A 50GHz sampling oscilloscope is used to measure the input and output waveforms. A k-connector system of probes, connectors, and cables with a bandwidth of approximately 40GHz is used to bring the data to the oscilloscope. The main challenge in this measurement is the low bandwidth of the measurement system compared to the signal bandwidth, so it is essential to carefully characterize the measurement setup.

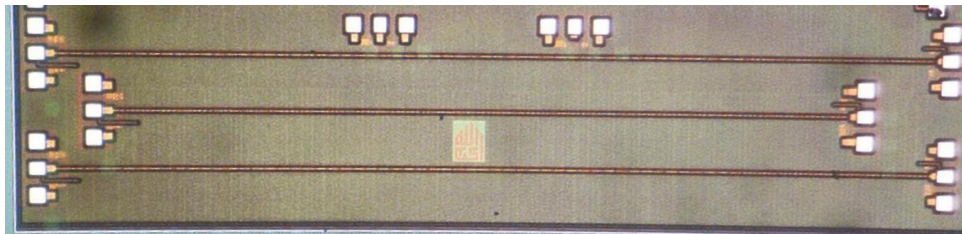


Figure 6.14: Chip micro photograph: the middle line is an edge sharpening line and the other two are pulse narrowing lines.

First the oscilloscope was characterized using a signal source. We swept the source frequency and measured the amplitude of the signal on the oscilloscope; then using the same signal source, cables, and connectors, we measured the signal amplitude using a wideband power meter. The ratio of these two values is the amplitude response of the oscilloscope. Figure 6.15 shows this response.

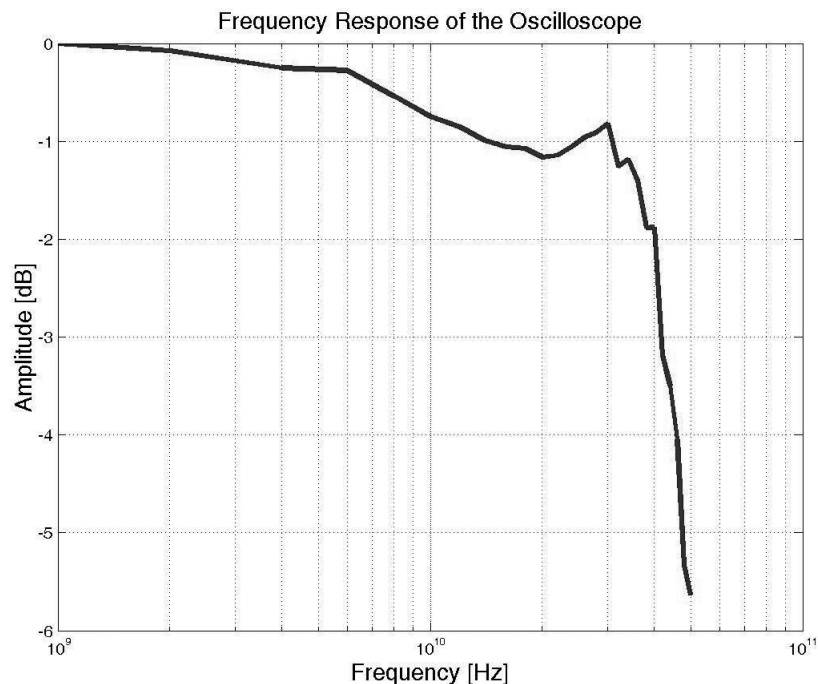


Figure 6.15: The frequency response of the oscilloscope

Then we characterize all other cables, connectors, probes, and bias tees using a 50GHz network analyzer. The response of these parts is shown in Figure 6.16. The amplitude response of the entire measurement setup is the product of Figure 6.15 and Figure 6.16. Using Matlab [75], one can show that the 10%-to-90% rise-time of such system is around 10.5ps, which indicates that it is not possible to resolve rise times lower than 10.5ps and pulse widths lower than 21ps.

Figure 6.17 shows the measured response of the pulse narrowing line to a 50ps input pulse. Based on response of the measurement setup (Figure 6.15 and Figure 6.16), the response of the measurement setup to a 2.5ps pulse is 21.5ps wide. The measured pulse width is 22ps, which is in good agreement with the simulation.

Matlab simulations show that if we have an ideal pulse with rise and fall times of 1.5ps and 20ps, we should expect rise and fall times of 10.5ps and 23ps, respectively with this measurement setup, as it is shown in Figure 9.15. The measured rise and fall times for this line are 11ps and 25ps, as shown in Figure 6.19. Also it is important

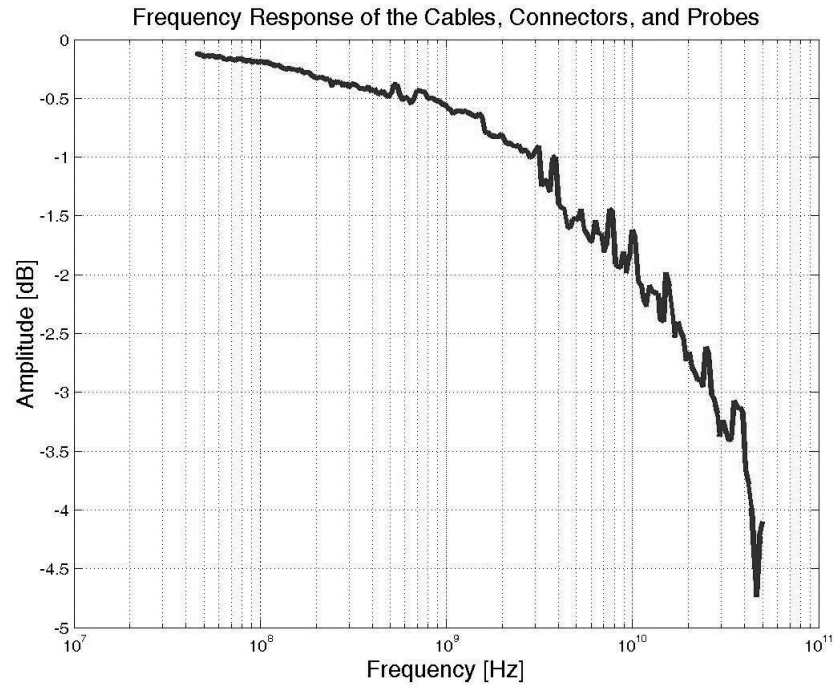


Figure 6.16: The frequency response of the cables, connectors, and probes

to note that the rise and fall times do not change with the input amplitude, as shown in Figure 6.20, which verifies the nonlinear behavior of the line.

In conclusion, in this chapter, We exploit the theory of pulse propagation through the NLTL and demonstrated a soliton line on a conventional silicon technology and a line capable of improving both the rise and fall times, simultaneously. Finally, we showed the experimental results verifying the agreement between the theory and the measurement.

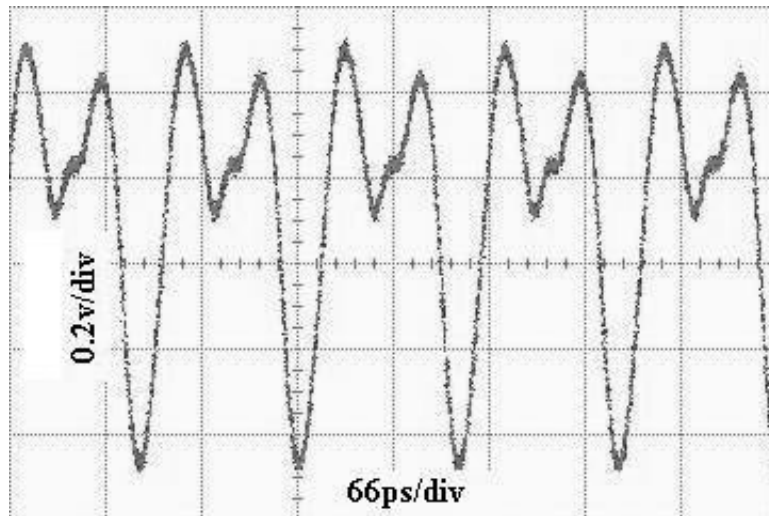


Figure 6.17: Input and output of pulse narrowing line

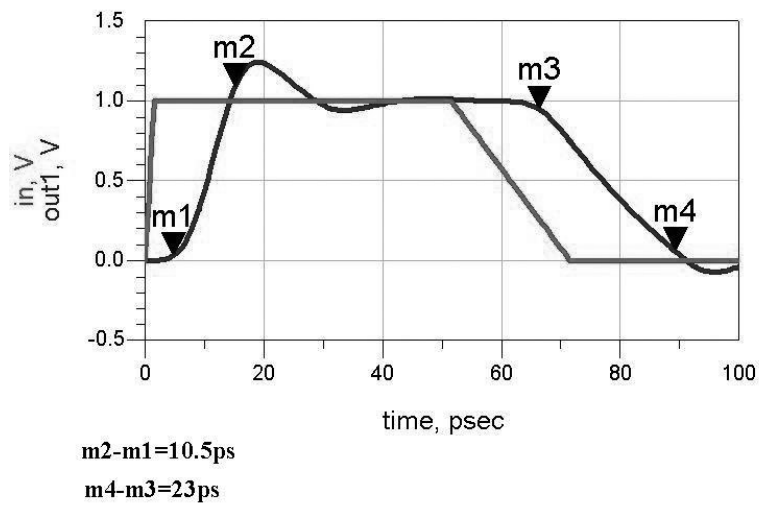


Figure 6.18: Response of the measurement setup to an ideal input

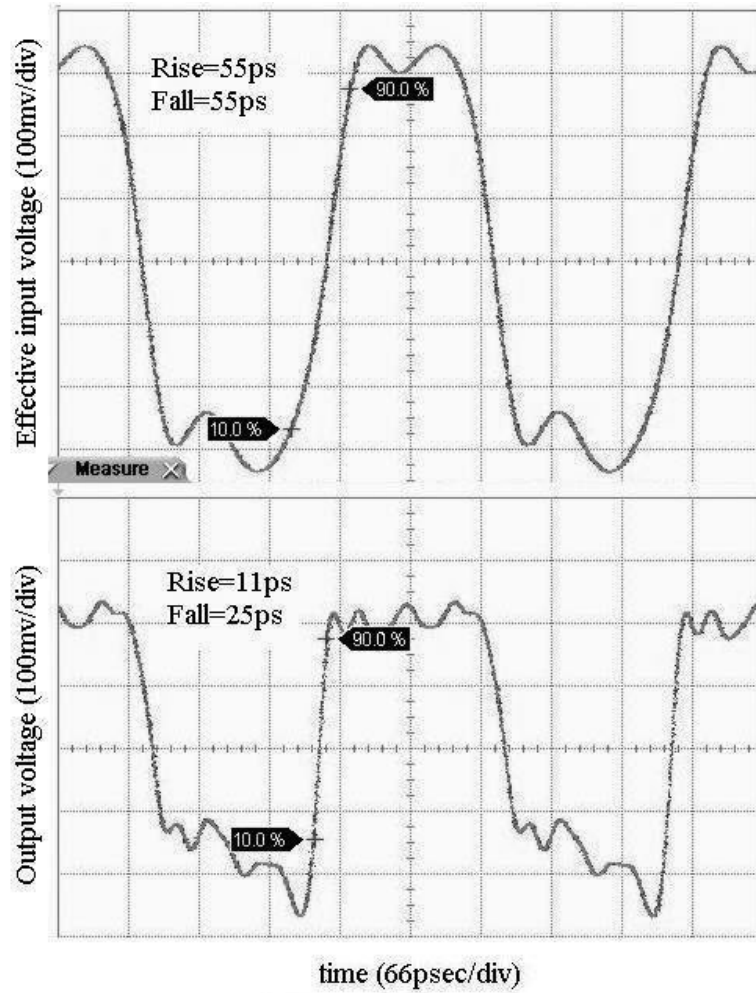


Figure 6.19: Input and output waveforms of the edge sharpening line

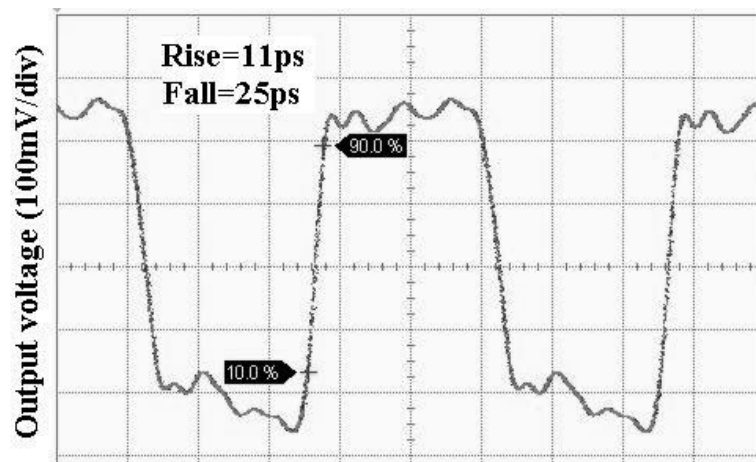


Figure 6.20: Output waveforms of the edge sharpening line with different amplitude verifying the nonlinear behavior of the line

Chapter 7

A Novel Broadband Power Generation Technique

7.1 Motivation

Recently, there has been growing interest in using silicon-based integrated circuits at high microwave and millimeter wave frequencies. The high level of integration offered by silicon enables numerous new topologies and architectures for low-cost reliable SoC applications at microwave and millimeter wave bands, such as broadband wireless access (*e.g.*, WiMax), vehicular radars at 24GHz and 77GHz citePfeiffer, short range communications at 24GHz and 60GHz, and ultra narrow pulse generation for UWB radar.

Power generation and amplification is one of the major challenges at millimeter wave frequencies. This is particularly critical in silicon integrated circuits due to the limited transistor gain, efficiency, and breakdown on the active side and lower quality factor of the passive components due to ohmic and substrate losses.

Efficient power combining is particularly useful in silicon where a large number of smaller power sources and/or amplifiers can generate large output power levels reliably. This would be most beneficial if the power combining function is merged with impedance transformation that will allow individual transistors to drive more current at lower voltage swings to avoid breakdown issues [77]. Most of the traditional power combining methods use either resonant circuits and are hence narrowband or

employ broadband, yet lossy, resistive networks [78].

In this chapter, we propose a general class of two-dimensional passive propagation media that can be used for power combining and impedance transformation among other things. These media take advantage of wave propagation in an inhomogeneous 2-D electrical lattice. Using this approach we show a power amplifier capable of generating 125mW at 85GHz in silicon [69].

7.2 A variation of Electrical Funnel

Chapter 4 covered the theory of wave propagation in 2D electrical lattices, also the concept of *electrical funnel* was introduced there. In this section, we offer a more intuitive explanation of how funnel works.

One-dimensional LC ladders have been extensively studied before. A homogeneous 1-D LC ladder consists of identical LC blocks repeated multiple times and can support wave propagation. It can also be used for broadband delay generation and low ripple filtering. An inhomogeneous linear 1-D line can be used to introduce controlled amount of dispersion to a signal.

A 1-D LC ladder can be generalized to a 2-D propagation medium by forming a lattice consisting of inductors (L) and capacitors (C). Figure 7.1 shows a square lattice. Generally, this lattice can be inhomogeneous where the L 's and C 's vary in space or nonlinear where they are current and/or voltage dependent. When the L 's and C 's do not change too abruptly, it is possible to define local propagation delay ($\alpha\sqrt{LC}$) and local characteristic impedances ($\alpha\sqrt{L/C}$) at each node. This allows us to define local impedance and velocity as functions of x and y , which can be engineered to achieve the desired propagation and reflection properties [68]. In this work, we show one application of these 2-D lattices as a means for simultaneous power combining and impedance transformation.

One way these surfaces can be engineered is by keeping the propagation velocity constant vertically (constant LC product for a given y), while increasing the characteristic impedance at the top and bottom of the lattice at a faster rate as we move

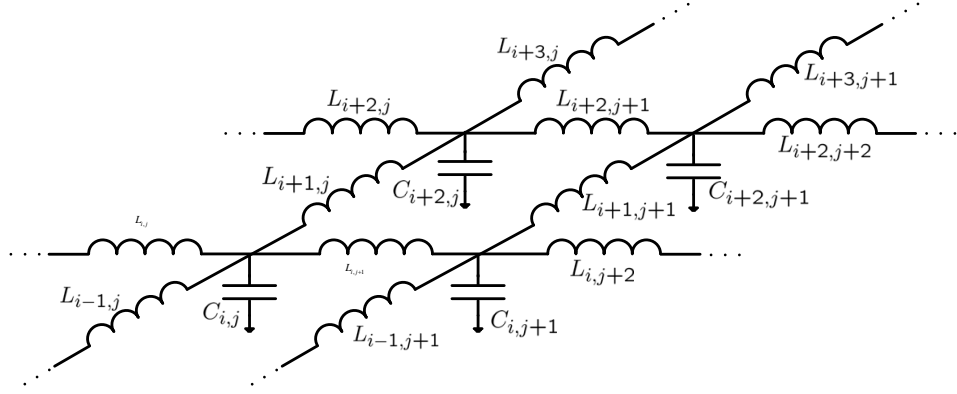


Figure 7.1: 2D square electrical lattice

along the x axis to the right, as illustrated in Figure 7.2. A planar wave propagating in the x direction from left to right gradually experiences higher impedances at the edges, creating a lower resistance path for the current in the middle; this funnels more power to the center as the wave propagates to the right, while we can perform a gradual impedance transformation from the left to the right. This is shown in the simulated voltage and current waveforms of Figure 7.3 (for more detail, see Chapter 4). By keeping the propagation velocity independent of y as we move along the x axis, we can maintain a plane wave keeping the lattice response frequency independent for the frequencies lower than its natural cut-off frequency [68]. We call this an *electrical funnel* due to the way it combines and channels the power to the center at the output.

Multiple synchronous signal sources driving the low-impedance left-hand side of the funnel can generate a planar wave-front moving along the x axis. The output node is at the center of the right boundary. The entire right boundary nodes are terminated with a resistor matched to the local impedance at that node. The up and down boundaries are kept open. Figure 7.3 shows simulated efficiency of one implementation vs. frequency demonstrating the broadband nature of the electrical funnel. Efficiency is defined by the ratio of the power at the output node to the sum of powers of inputs.

As mentioned in Chapter 4, there is a dual to the funnel where the local characteristic impedance is kept independent of y while the propagation velocity is modified

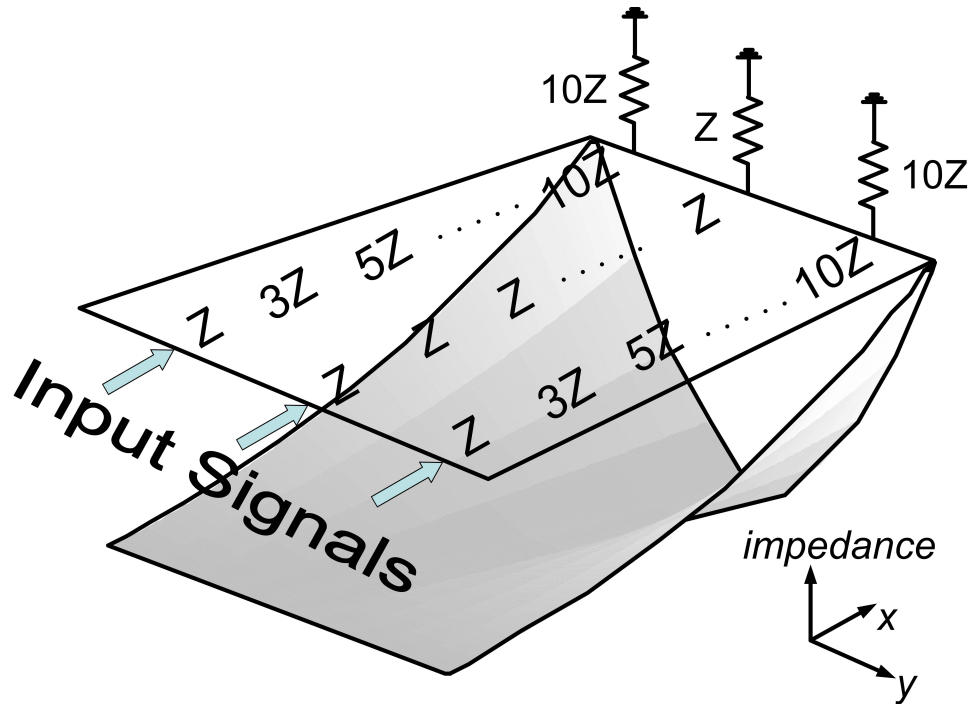


Figure 7.2: Basic idea of a funnel

to increase at the top and bottom of the combiner as the wave front moves to the right. The input sources on the left boundary add coherently at the focal point which should occur in middle of the right boundary where the output is taken. This resembles the behavior of an optical lens and is thus called an *electrical lens*, due to its focusing nature. However, this focusing behavior is frequency dependent and hence works perfectly only at one frequency. For other frequencies, the phase shift from the input to the output is different, resulting in a different focal length. For this reason, electrical lens might not be an ideal power combiner, however it could take spatial Fourier transform of the input signal. We will investigate this property in Chapter 9.

In practice, the characteristic impedance at the edges of the rectangular implementation keeps increasing and hence it is possible to discard the higher impedance parts of the mesh as we move to the right, effectively reducing it to a trapezoid. In a silicon process with multiple metals, we can use different metal layers as the ground plane at different points on the y axis. Our design uses four lower metal layers to form the variable depth ground plane. This leads to different capacitance per unit length

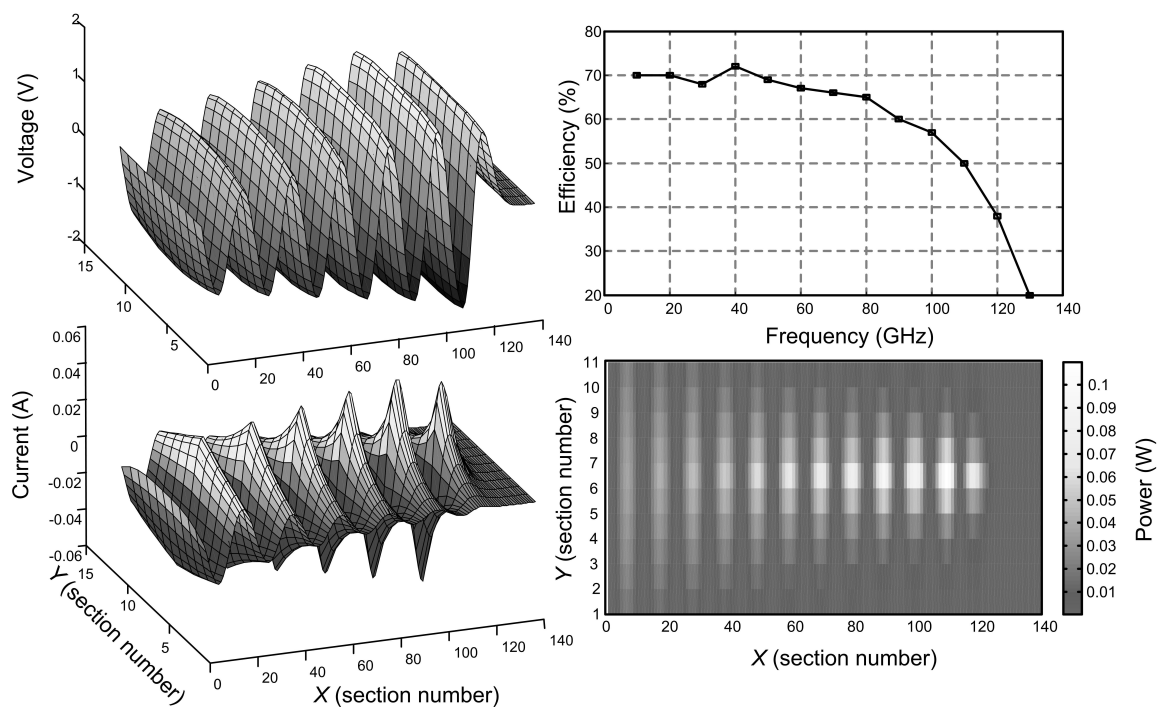


Figure 7.3: Simulation results of an ideal funnel with $30\text{pH} \leq L \leq 150\text{pH}$ and $30\text{fF} \leq C \leq 300\text{fF}$

that can be used to control the local characteristic impedance across the combiner, as shown in Figure 7.4. Since this does not change the inductance, the propagation delay is not constant vs. y , resulting in a band-pass response. The output is matched to 50Ω while each of the inputs is matched to around 15Ω . The difference between this structure and a standard tapered transmission line is a larger bandwidth (45% increase in this case) over a shorter distance (lower loss) due to the variable-depth ground plane. This has reduced the combiner's dimension to $410\mu\text{m}$ by $240\mu\text{m}$.

7.3 Power Amplifier Architecture

To verify the feasibility of this approach, we used this combiner to design a power amplifier in a $0.12\mu\text{m}$ SiGe BiCMOS with a bipolar cutoff frequency of 200GHz . Figure 7.5 shows the chip architecture.

Four power amplifier drive the power combiner to maximize the output power.

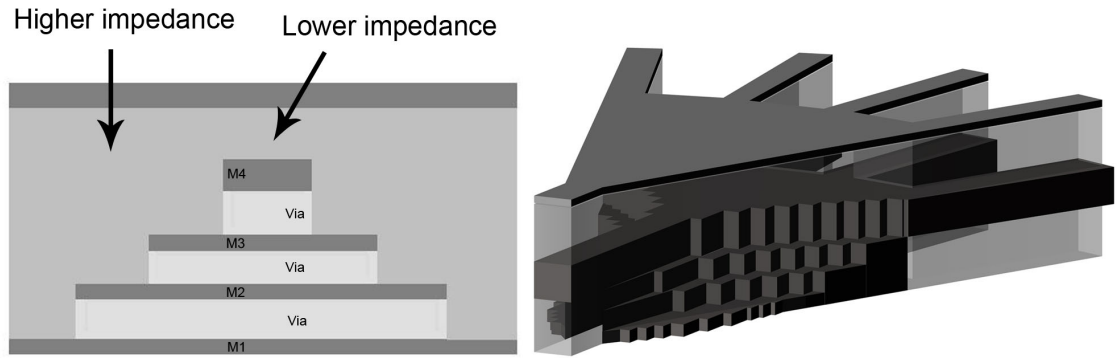


Figure 7.4: Combiner structure

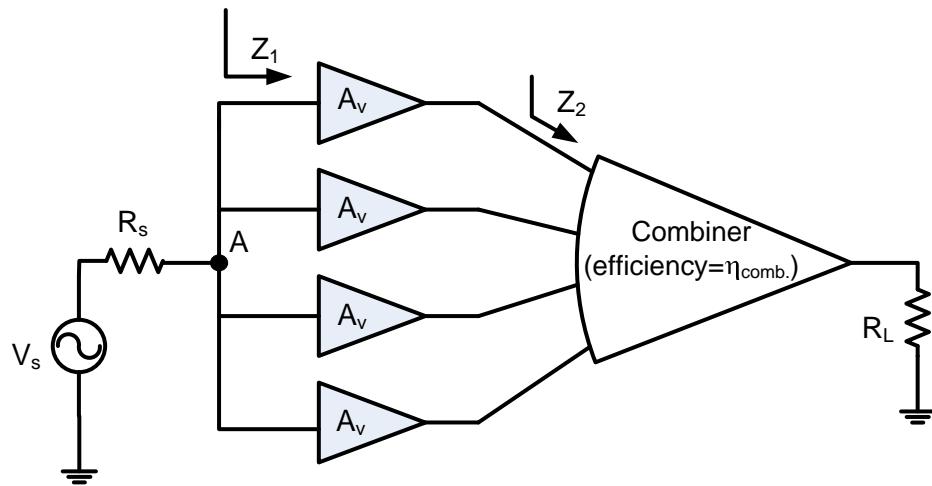


Figure 7.5: The architecture of power amplifier

Assume that the voltage at node A in Figure 7.5 is V_{in} , then we could write input and output power as:

$$P_{in} = n \cdot \frac{V_{in}^2}{2Z_1} \quad (7.1a)$$

$$P_{out} = n \cdot \frac{A_v^2 V_{in}^2}{2Z_2} \cdot \eta_{comb.} \quad (7.1b)$$

Where Z_1 and Z_2 are input and output impedance of each amplifier, A_v is its voltage gain, n is the number of amplifiers, and $\eta_{comb.}$ is the combining efficiency.

From input and output power, we can find the power gain of the amplifier, G , as:

$$G = \frac{P_{out}}{P_{in}} = A_v^2 \cdot \eta_{comb.} \cdot \frac{Z_1}{Z_2} \quad (7.2)$$

7.3.1 Driver Design

In order to obtain a wideband response, we use degenerate cascode distributed amplifiers with emitter degeneration as input drivers, shown in Figure 7.6. The main advantage of cascode stage over single transistor is its higher maximum stable power gain. As Figure 7.7 shows, a non-degenerate cascode amplifying stage in this process has a maximum stable power gain of 15dB at 80GHz, as opposed to 7dB for a standard common-emitter. The cascode stages are emitter degenerated to improve bandwidth and avoid thermal runaway.

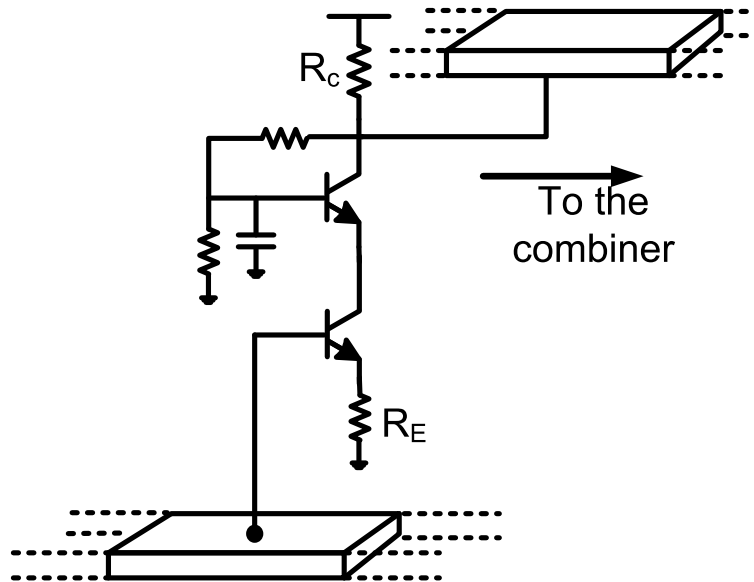


Figure 7.6: Cascode architecture

Each of the four distributed amplifiers consists of eight cascode stages driving the output transmission line, which drive the inputs of the combiner. Figure 7.8 shows the structure of each distributed amplifier.

Figure 7.9 shows the gain of each stand alone distributed amplifier. Using equation 7.2, for our amplifier, with $A_v \sim 1.8$, $\eta_{comb.} \sim 0.7$, and $Z_1 \sim 4Z_2$ the power gain in 84

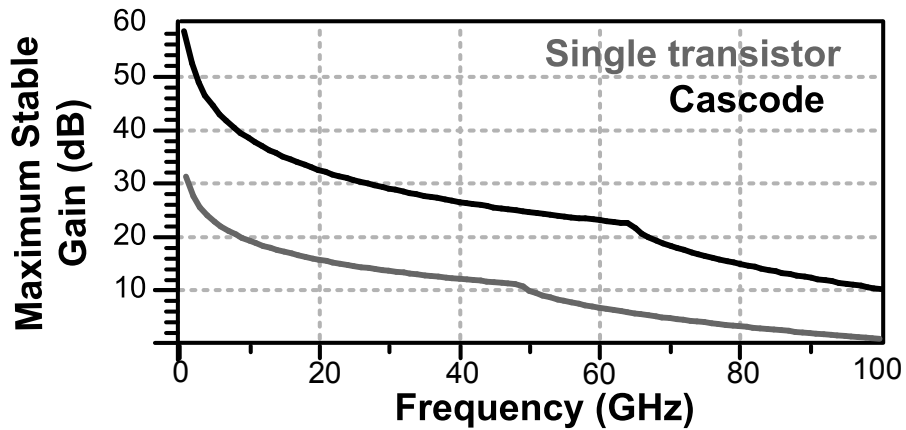


Figure 7.7: Maximum stable power gain of a cascode stage vs. a single transistor

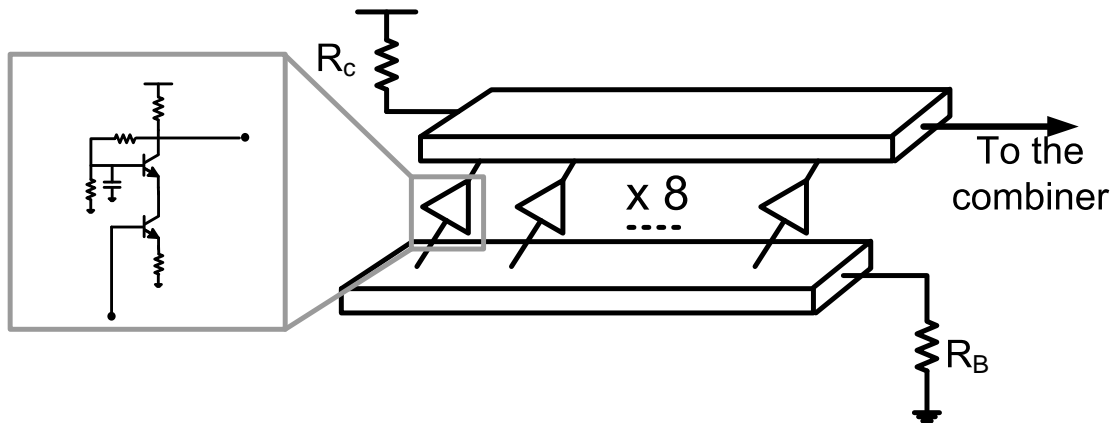


Figure 7.8: One stand alone distributed power amplifier

GHz should be around 9dB, which is close to the measured value of 8dB.

7.4 Implementation

Die photo of the amplifier is shown in Figure 7.10. Figure 7.11 shows the setup that we used to measure the characteristic of the power amplifier.

The chip is mounted on a brass substrate which is connected to ground. The input is provided by an HP 83650B signal generator and a Spacek frequency multiplier which could generate power from 60GHz to 90GHz. To be able to control input power, a variable attenuation is used before the RF probes. We probe input and output of our

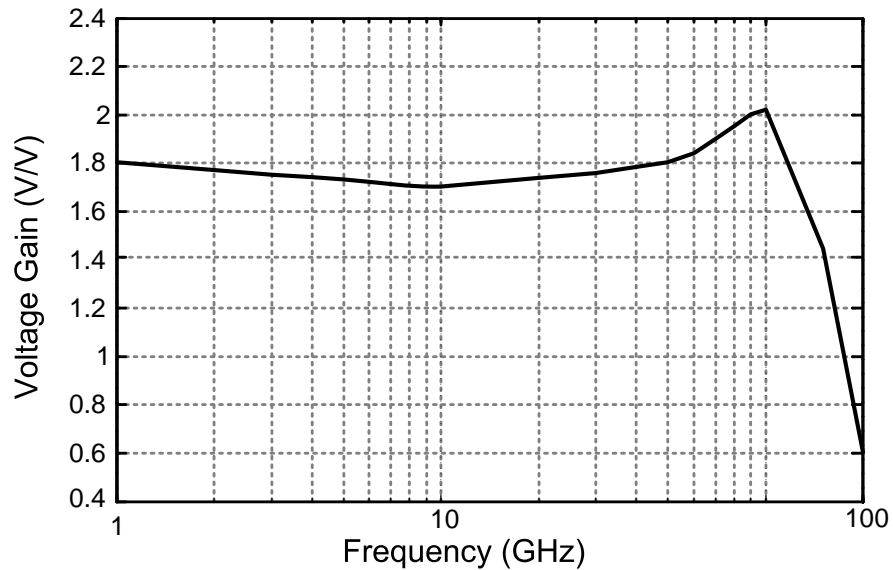


Figure 7.9: Simulated gain of each distributed amplifier

amplifier and measure the output power using a power-meter. Because the chip has two supplies (-2.5V and 0.8V), we can't directly connect the chip substrate (which is at -2.5V) to the brass. On the other hand it is critical to have a good heat sink for our chip. To solve this problem we use a thin low-cost CVD diamond [79] between our chip and brass. Diamond is a superior electrical insulator and is the best isotropic thermal conductor with thermal conductivity of around 10 W/cm/K. Figure 7.12 shows the chip under the test.

7.4.1 Measurement Results

The driver amplifiers have two power supplies of -2.5V and 0.8V and draws 750mA of current. Figure 7.13 and Figure 7.14 show the measured small signal gain and peak output power of the amplifier vs. frequency. The maximum output power was measured using two different signal sources: a backward wave oscillator (BWO) and a frequency multiplier. The overall small-signal gain is above 8dB at 85GHz where the peak power of 125mW is achieved. The lower measured maximum power in the multiplier measurement is due to its limited output power compared to BWO and the lower amplifier gain above 86GHz. At 85GHz, the output power and drain efficiency

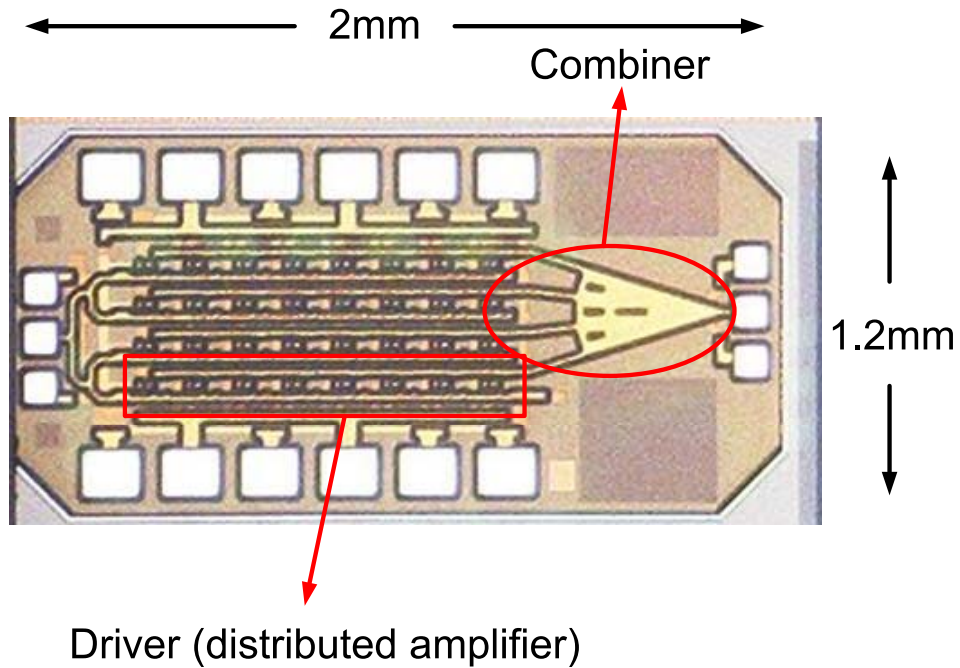


Figure 7.10: Chip micro photograph

as a function of input power are shown in Figure 7.15. At 85GHz, drain efficiency is more than 4% at 3dB gain compression. The amplifier has a 3dB power bandwidth of 24GHz (between 73GHz and 97GHz).

7.4.2 Comparison and Conclusion

A comparison of presented power amplifier with previous work on mm-wave power amplifiers (mostly in silicon) is summarized in table 7.1. Among other amplifiers on silicon substrate this work demonstrates the highest achieved center frequency of operation (85GHz) and the highest achieved power output (120mW) at this frequency. It is noteworthy that the relatively low efficiency of the amplifier is due to the low efficiency of the drivers as we used class A distributed amplifiers. The peak efficiency of the power combiner is around 70% and we could use different classes of drivers to increase the power efficiency by sacrificing some bandwidth.

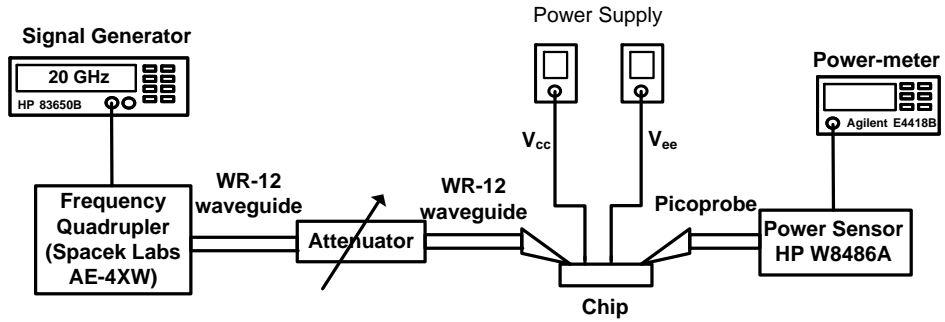


Figure 7.11: Measurement setup

<i>Freq.</i>	<i>Device</i>	$P_{out}(dBm)$	$PAE_{max}(\%)$	$Gain(dB)$	<i>Ref.</i>
85GHz	0.12 μ m SiGe HBT	20.8	4	8	This work
77GHz	0.12 μ m SiGe HBT	17.5	12.8	17	[80]
77GHz	0.12 μ m SiGe HBT	13	3.5	6.1	[76]
60GHz	0.12 μ m SiGe HBT	16	4.3	10.8	[81]
90GHz	0.12 μ m GaAs pHEMPT	21	8	19	[82]

Table 7.1: A comparison between this work and other designs

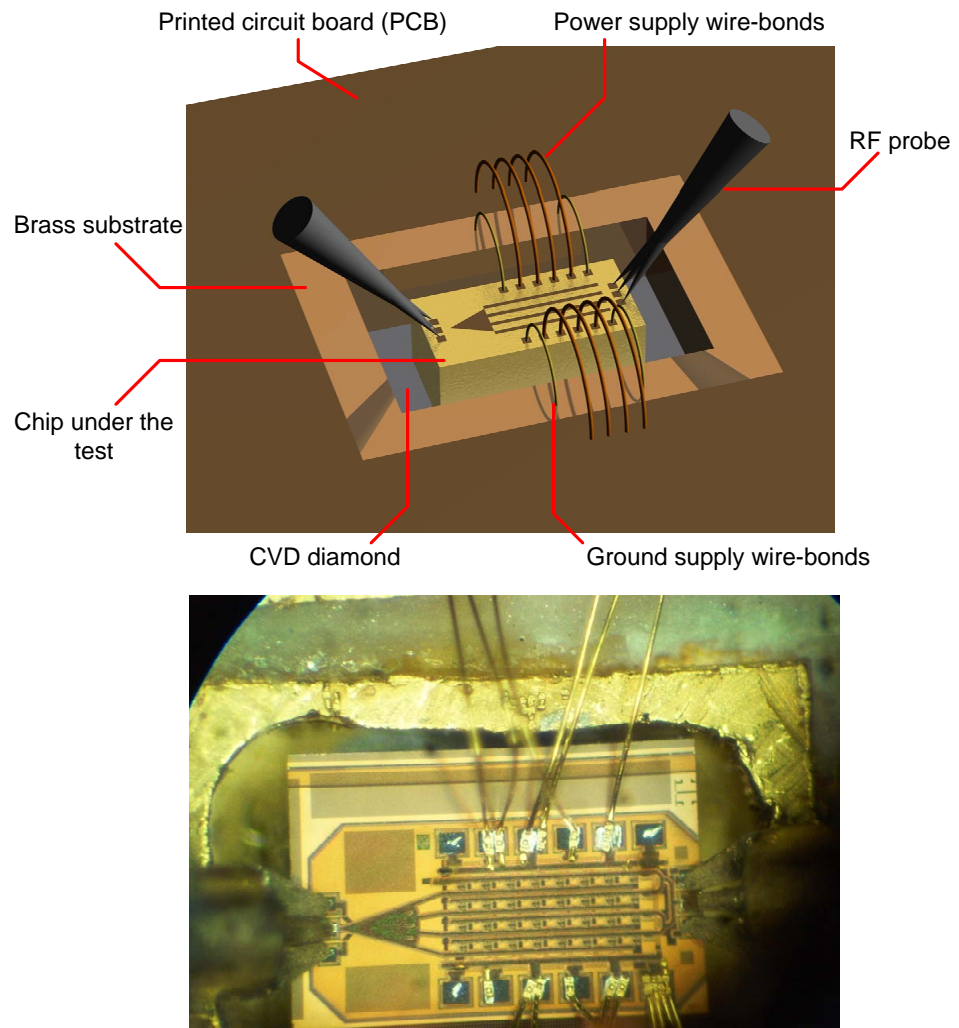


Figure 7.12: The power amplifier chip under test

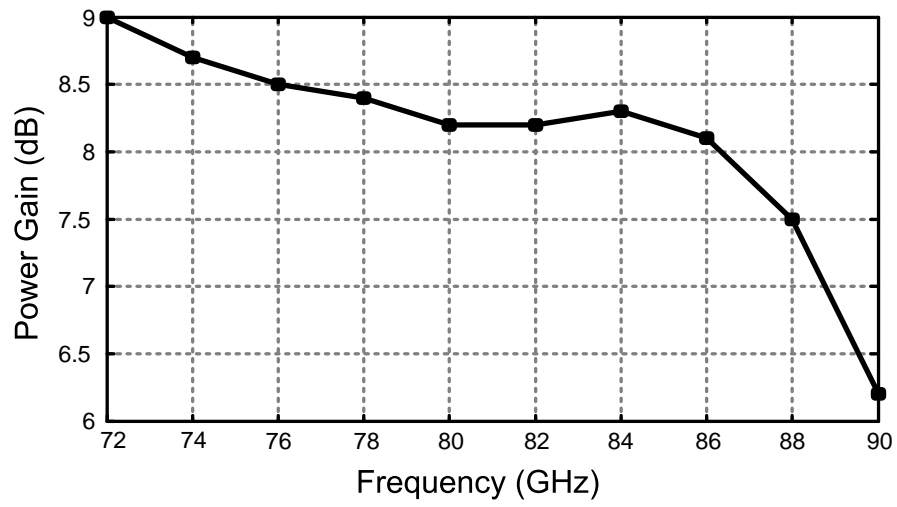


Figure 7.13: Measured small signal gain of the amplifier

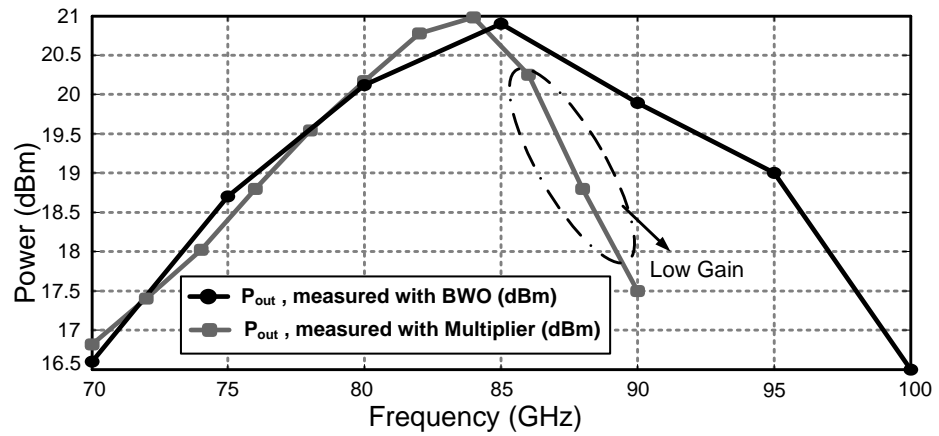


Figure 7.14: Measured peak output power of the amplifier

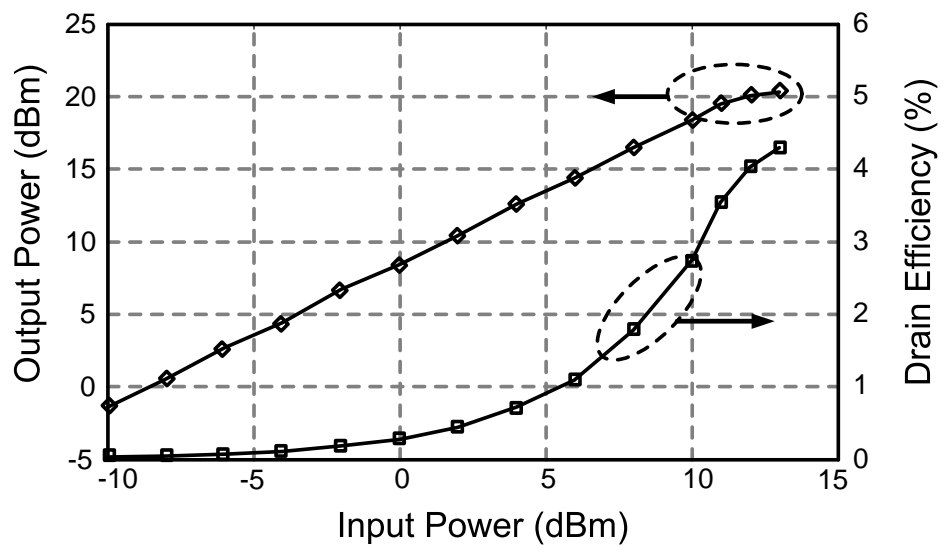


Figure 7.15: Large signal behavior of the amplifier at 85GHz

Chapter 8

Nonlinear Resonance in Two-Dimensional Electrical Lattices

8.1 Introduction

Consider an electrical lattice comprised of inductors and capacitors, as shown in Figure 8.1. Suppose that voltages are applied at the boundaries, producing two or more

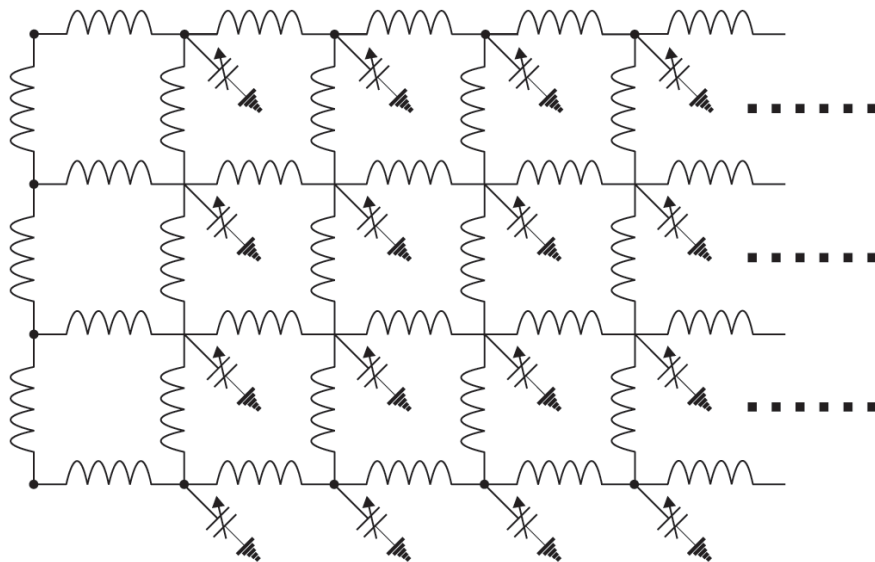


Figure 8.1: 2-D Nonlinear Transmission Lattice

wave fronts that propagate towards the center of the lattice. In this chapter, we show that for certain configurations of inductors and voltage-dependent capacitors, the incoming waves combine nonlinearly, producing a single outgoing wave with peak amplitude *greater* than the sum of the incoming waves' amplitudes. Through numerical experiments, we shall examine how this resonant wave interaction is affected by varying the incoming waves' amplitudes, phases, and frequency content. In all cases, we are concerned with the regime in which (1) the ratio of amplitude to wavelength is large and (2) the ratio of lattice spacing to wavelength is non-negligible.

The lattice in Figure 8.1 is the natural generalization to two spatial dimensions of the classical one-dimensional transmission line shown in Figure 8.2. It has been

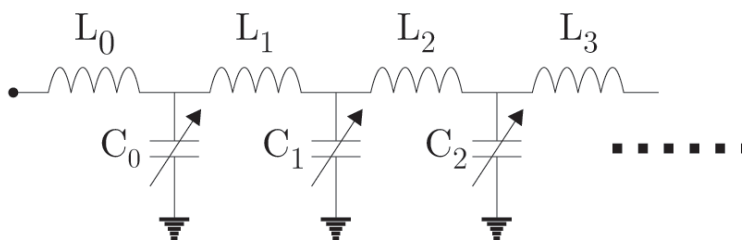


Figure 8.2: 1-D Nonlinear Transmission Line

known [38][39][40][4] since the 1960s that the presence of voltage-dependent capacitors in these one-dimensional structures leads to nonlinear wave phenomena, including the formation of solitons. As a result, nonlinear transmission lines (NLTs) have been studied by various groups [45][46][43][47][48] with a focus on solitonic generation of ultrashort, high-power, stable electrical pulses. Recent developments [56; 55] have demonstrated that NLTs are suitable for a variety of ultra-wideband pulse-shaping applications, and that they can be built inexpensively on silicon chips.

As early as the 1940's, Léon Brillouin analyzed wave propagation in two-dimensional *linear* lattices [33]. In contrast, two-dimensional nonlinear electrical lattices have not received as much attention, and we are aware of only three works on this subject other than our own. These papers were concerned with establishing that 2-D soliton formation was possible, either through experiments [83][84] or through weakly nonlinear asymptotics [50]. For the remainder of this chapter, we label inductors and capacitors in the 2-D lattice as shown in Figure 8.3. In [50], the authors assume a uniform, non-

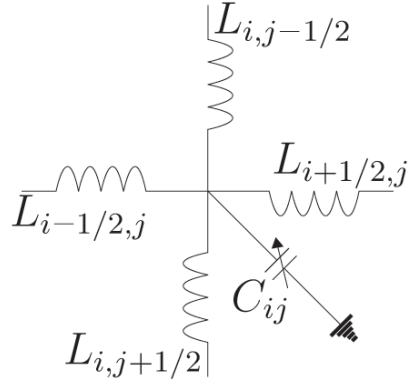


Figure 8.3: 2-D Nonlinear Lattice Block

linear 2-D lattice with $L_{ij} = L$ and $C_{ij}(V) = C(V)$ everywhere; they show that the Kadomtsev-Petviashvili (KP) equation describes weakly nonlinear wave propagation in such lattices. In [68], it is shown how to choose L_{ij} and C_{ij} nonuniformly in space, for both linear and nonlinear lattices, in order to design circuits that focus power from different input signals. Let us quickly review the mathematical modeling of these 2-D lattices; a detailed description of what follows may be found in [68].

Using Kirchoff's laws, one writes equations for the current I and voltage V in the lattice:

$$I_{i,j-1/2} + I_{i-1/2,j} - I_{i+1/2,j} - I_{i,j+1/2} = \frac{d}{dt} (C_{ij}(V_{ij})V_{ij}) \quad (8.1a)$$

$$V_{ij} - V_{i,j-1} = -L_{i,j-1/2} \frac{d}{dt} I_{i,j-1/2} \quad (8.1b)$$

$$V_{ij} - V_{i+1,j} = L_{i+1/2,j} \frac{d}{dt} I_{i+1/2,j} \quad (8.1c)$$

Here L_{ij} and C_{ij} are prescribed, while I_{ij} and V_{ij} are unknown functions of time only. System (8.1), with appropriate boundary conditions that we will make precise later, is what we solve numerically in order to study wave interactions in 2-D electrical lattices. In order to obtain analytical insight into the problem, we may examine various continuum limits of (8.1).

From the lattice equations to the KP equation. Starting from (8.1), we may outline one possible path to the KP equation. For now we take $L_{ij} = L$ and $C_{ij}(V) = C_0(1 - bV)$ everywhere, and consider a continuum model of (8.1) for the case of an *equispaced* lattice, where h is the distance between any two adjacent nodes. We switch from L and C to, respectively, the inductance and capacitance per unit length $L' = L/h$ and $C'_0 = C_0/h$. Next, we decouple (8.1) and obtain a single second-order equation for the unknown V_{ij} :

$$\frac{1}{h^2} (V_{i,j-1} - 2V_{ij} + V_{i,j+1} + V_{i-1,j} - 2V_{ij} + V_{i+1,j}) = L'C'_0 \left[(1 - bV_{ij}) \frac{d^2 V_{ij}}{dt^2} - b \left(\frac{dV_{ij}}{dt} \right)^2 \right]. \quad (8.2)$$

Standard Taylor series * then allows us to approximate the discrete function $V_{ij}(t)$ by a smooth function $V(x, y, t)$, and then rewrite the left-hand side of (8.2) as follows:

$$\nabla^2 V + \frac{h^2}{12} (V_{xxxx} + V_{yyyy}) = L'C'_0 [(1 - bV)V_{tt} - b(V_t)^2]. \quad (8.3)$$

Here and in what follows, subscripts denote partial derivatives. Starting from the continuum model (8.3), we now seek an equation that describes, asymptotically, small-amplitude two-dimensional long waves propagating through the lattice. To derive such an equation, we set $\nu_0 = (L'C'_0)^{-1/2}$ and introduce scaled variables

$$\xi = \varepsilon^{1/2}(x - \nu_0 t), \quad \eta = \varepsilon y, \quad T = \frac{1}{2}\nu_0 \varepsilon^{3/2} t. \quad (8.4)$$

*Inherent in this application of Taylor series is the assumption that h/λ is sufficiently small, where λ is a characteristic wavelength.

We insert (8.4) into (8.3), expand $V = \varepsilon V_1 + \varepsilon^2 V_2 + \dots$, and drop all terms except those of lowest order in ε . The scaling (8.4) selects certain waves; specifically those that propagate mainly in the x -direction with the y -direction treated as a perturbation. The expansion/truncation of V is valid only if A/λ , the ratio of amplitude to wavelength, is sufficiently small. The result of this procedure will be the Kadomtsev-Petviashvili (KP) equation [†]:

$$\left[(V_1)_t + V_1 (V_1)_x + (V_1)_{xxx} \right]_x + (V_1)_{yy} = 0. \quad (8.5)$$

Equation (8.5) is a weakly nonlinear limit of the continuum lattice model (8.3). For more details, please consult [68].

Remark. Starting from (8.1), suppose we choose L_{ij} and C_{ij} such that they are not constant functions of i and j . Following the same procedure as outlined above, the final equation will be KP plus two extra terms that involve the spatial derivatives L_x and L_y ; again, see [68] for full details.

8.1.1 KP Resonance

In prior work on nonlinear resonant wave interaction, the KP equation is often the starting point. One reason is that the KP equation is rather special: it is completely integrable by the inverse scattering method [85]. Related to its integrability is the fact that KP possesses exact soliton solutions. Prior studies of nonlinear wave interaction in the KP system, originating from the works of J. W. Miles [86; 87], have yielded a wealth of information regarding collisions of two or more KP solitons. Let us review what is known about the most basic resonant interactions possible in KP, interactions that involve two incoming solitons merging together to form one outgoing soliton. In what follows, (\mathbf{k}_i, ω_i) denotes the wave vector and angular frequency of each soliton,

[†]Equation (8.5) as we have written it is actually the “negative–dispersion KP” or “KP-II” equation. Flipping the sign on the ϕ_{yy} term yields the “positive–dispersion KP” or “KP-I” equation. As we are concerned with resonant wave interactions, which are impossible for KP-I (see Fig. 7.3 in [8]), we will consider only KP-II and refer to it as simply “KP” for the remainder of this work.

with $i = 1, 2$ denoting incoming solitons and $i = 3$ denoting the outgoing soliton.

1. In a resonant collision of solitons, the outgoing wave vector and frequency are the sums of the incoming wave vectors and frequencies, respectively:

$$\mathbf{k}_3 = \mathbf{k}_1 + \mathbf{k}_2 \quad (8.6)$$

$$\omega_3 = \omega_1 + \omega_2. \quad (8.7)$$

2. As established rigorously in [88], resonance occurs when the incoming solitons interact at an angle ψ that belongs to a certain range $[\psi_{c_1}, \psi_{c_2}]$. The interaction angle is defined by

$$\psi = \psi_2 - \psi_1,$$

where each ψ_i is defined via $\mathbf{k}_i = k(\cos \psi_i, \sin \psi_i)$.

3. If the incoming solitons have the same amplitude A , the outgoing soliton can have an amplitude of at most $4A$. As pointed out in [89], this is a simple consequence of (8.6) and the fact that, for a soliton, the amplitude and wavenumber are tied together via

$$A_j \approx Mk_j^2$$

where M is a constant independent of j .

Prior studies of KP resonance typically focus on the interaction of solitons only, not general nonlinear waves. The focus on soliton interactions means that very little is known about the interactions of more general waves in the KP system. Let us also mention that the soliton solutions of KP are themselves special, requiring an infinite domain and decaying boundary data. Finally, little is known about whether resonance is possible in systems described by an equation consisting of KP plus extra terms (perturbations), as would arise when we introduce inhomogeneities into the L_{ij} and C_{ij} matrices for our 2-D lattice.

8.1.2 Resonance in Electrical Lattices

In the present work, we demonstrate that a KP-like resonance is possible in two-dimensional, bounded, nonlinear electrical lattices. Such lattices can be built on chip and the resonance phenomena can be used for a variety of applications. The applications we have in mind involve input signals with frequency content that exceeds the cut-off frequency of the fastest active components (e.g., transistors). Hence we consider lattices with passive components only. Of course, even a lattice with only passive components has a natural cut-off frequency. We can see this most concretely in the case of a linear, homogeneous lattice, which is modeled by (8.2) with $b = 0$:

$$V_{i,j-1} - 2V_{i,j} + V_{i,j+1} + V_{i-1,j} - 2V_{i,j} + V_{i+1,j} = LC \frac{d^2}{dt^2} V_{i,j}. \quad (8.8)$$

By considering plane wave propagation with wave vector $\mathbf{k} = (k_x, k_y)$, and frequency f , one finds the dispersion relation

$$4\pi^2 f^2 = \frac{2}{LC} [2 - (\cos k_x + \cos k_y)]. \quad (8.9)$$

Clearly the maximum value of f occurs when $k_x = k_y = \pm\pi$. In this case,

$$f_M = \frac{1}{2\pi} \sqrt{\frac{8}{LC}}. \quad (8.10)$$

With today's state of the art integrated circuit technologies, on a silicon substrate, the minimum possible integrated inductance and capacitance are, approximately, $L_M = 30$ pH and $C_M = 5$ fF. Below these values, the parasitic inductance and capacitance would be dominant. Using these values in (8.10), we find that the maximum frequency for plane wave propagation on a 2-D silicon transmission lattice is $f_M \approx 1.16$ THz. In the present work, our working values of L and C will be

$$C = 1.0 \times 10^{-12} \text{ F} = 1.0 \text{ pF} \quad (8.11a)$$

$$L = 1.0 \times 10^{-9} \text{ H} = 1.0 \text{ nH}. \quad (8.11b)$$

Suppose we wish to determine, for such a lattice, how many lattice points are needed to describe one wavelength of a 10 GHz plane wave. We use (8.11), $k_y = 0$, and $f = 10^{10}$ in the dispersion relation (8.9), and find that $k_x \approx 2.91 < \pi$, which corresponds to $\lambda_x \approx 2.16h$, where h is the lattice spacing.

Recall that for a lattice with spacing h , the *minimum* wavelength is $2h$. Moreover, for the lattices we consider, the lattice spacing h is on the order of microns. Though the preceding analysis is exact only for linear lattices, it is clear that general gigahertz-range circuits will involve waves where the A/λ ratio is large and the λ/h ratio is small. This is a regime where the asymptotics described earlier, and therefore the KP equation itself, does not apply. Therefore, in our analysis, we work with the lattice ODE equations (8.1) directly, rather than with the KP equation or with any other continuum model.

8.1.3 Main Results

By solving (8.1) numerically, we demonstrate that KP-like nonlinear resonant combining of input signals is possible in electrical lattices. Moreover, we demonstrate that the resonance is in some cases *enhanced* by working in the strongly nonlinear, highly discrete regime where the two ratios h/λ and A/λ are not small. In this regime, the KP equation and other perturbative approaches to the lattice dynamics are invalid. We further demonstrate that the resonance is robust with respect to unequal input signal amplitudes as well as mismatched input phases. Finally, we study multiple resonance effects as well as resonant combining of non-sinusoidal waves.

Outline. This chapter is organized as follows. In Section 8.2, we provide details regarding the system of differential equations we solve, as well as their initial and boundary conditions. Basic results on resonance phenomena, including the effects of unequal input amplitudes and varying interaction angles, are presented in Section 8.3. Finally, in Section 8.4, we provide further results showing various ways by which one can enhance the resonance phenomena.

8.2 Numerical Setup

Our study of resonance in 2-D electrical lattices proceeds by systematically carrying out numerical experiments on system (8.1). Unless other dimensions are explicitly given, we assume we are working with a square 80×80 lattice. This lattice contains capacitors C_{ij} at all nodes except for those on the left boundary, as shown in Figure 1. Linear capacitors correspond to $\partial C_{ij}/\partial V_{ij} = 0$; in the present work, we consider nonlinear capacitors that have the following piecewise-linear dependence on voltage:

$$C_{ij}(V_{ij}) = \begin{cases} (C_0)_{ij} & V_{ij} < 0 \\ (C_0)_{ij} (1 - bV_{ij}) & 0 \leq V_{ij} \leq V_M \\ (C_0)_{ij} (1 - bV_M) & V_{ij} > V_M \end{cases} \quad (8.12)$$

Precise values of b and V_M will be specified for each numerical run. Typically we will consider homogeneous lattices with parameters $(C_0)_{ij} = C$ and $L_{ij} = L$, where L and C were given in (8.11).

Unlike what is shown in Figure 8.1, our lattice is bounded on the right, as shown in Figure 8.4. In practical applications, we choose this value so as to minimize reflection of incident wave energy. For the simulations presented here, we stop running before the signal reaches the right boundary; hence the exact value of the right boundary resistance does not affect the results we report. In future work, we will examine the scattering problem that arises when nonlinear lattice waves hit the right boundary.

For each simulation, we assume that the interior of the lattice is initially free of current and voltage, i.e., $V_{ij}(t = 0) = 0$ for all i and all $j > 0$, and $I_{i\pm 1/2,j}(t = 0) = I_{i,j\pm 1/2}(t = 0) = 0$ for all i and all j . In most of the experiments, we consider sinusoidal forcing of amplitudes A_L and A_B applied to, respectively, the left and bottom boundaries of the lattice. We use the convention that the left boundary corresponds to $(i, j) = (1, j)$ and the bottom boundary corresponds to $(i, j) = (i, 1)$,

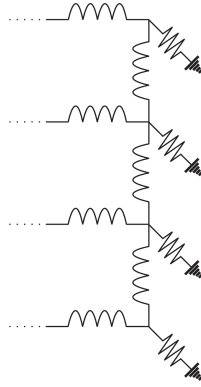


Figure 8.4: Right boundary of the 2-D electrical lattice, showing the resistive termination.

so

$$V_{1,j}(t) = A_L \sin(2\pi ft + \phi_j) \quad (8.13a)$$

$$V_{i,1}(t) = A_B \sin(2\pi ft + \phi_i), \quad (8.13b)$$

with $f = 10$ GHz, $1 \leq i \leq 40$, and $1 \leq j \leq 40$. In case $A_L \neq A_B$, we use A_B for the corner node $(1, 1)$. Occasionally we consider different types of forcing applied to the same or different boundaries of the lattice; when we do so, we shall mention it explicitly.

With the initial and boundary conditions as specified, we solve (8.1) numerically. In each numerical experiment, waves introduced into the lattice through boundary forcing interact, producing outgoing waves. In what follows, we record and discuss numerical observations of these outgoing waves. We focus on the amplitudes of the outgoing waves, as a function of the amplitudes/angles of the incoming waves.

8.3 Results of Numerical Experiments

8.3.1 Equal amplitude and in-phase.

First we examine the case where both incoming waves have equal amplitude and are in phase. Along the left and bottom boundaries, we stipulate that the voltages are

given by

$$V_{1,j}(t) = A \sin(2\pi ft) \quad (8.14a)$$

$$V_{i,1}(t) = A \sin(2\pi ft) \quad (8.14b)$$

For this experiment, we use nonlinear capacitors modeled by 8.12 with parameters $b = 0.5$ and $V_M = 1.9$. Then, with the numerical setup given in Section 8.2, we find that the two incoming waves collide to produce one single outgoing wave of amplitude A_R . By repeating the experiment with different values of A , we study the dependence of the resonance amplitude A_R on the incoming amplitude A . The resulting data is shown in Figure 8.5.

Based on this data, we make the following observations:

1. The ratio A_R/A measures the efficiency of the combining; for linear combining, the output amplitude $A_R = 2A$ always. Since our lattice itself was nonlinear, we expected all incoming waves to combine nonlinearly, regardless of their amplitude A . In our experiments, we found $A_R/A > 2$ always, confirming this expectation.
2. When the voltages in the lattice are small (much less than unity), we may be in the KP regime, but when $A_R \geq 1V$, it is clear that the weakly nonlinear KP theory no longer applies. At $A = 0.3V$, for example, we are able to produce an output signal that has more than six times the amplitude ($A_R > 6A$) of the input. Note that for a range of inputs, $0.25V < A < 0.4V$, the discrete resonance exceeds the $A_R = 4A$ bound established for the KP equation.
3. We also expected a saturation effect due to the form of nonlinearity we assumed in the capacitor model (8.12). For $V > V_M$, the capacitance of each C_{ij} is independent of V . A signal for which $V > V_M$ everywhere in space (e.g., a DC biased signal) would not see the nonlinearity of the lattice at all; for such a signal, linear dynamics prevail. However, the signals we deal with in this chapter, do not have any DC bias—they oscillate about zero with some

amplitude A . If $A > V_M$, then some portion of the signal will experience only linear dynamics.

For this experiment in particular, $V_M = 1.9$, so we do not expect nonlinear combination to work as efficiently when $A_R \approx 1.9$. This explains the drop in the ratio A_R/A as A increases beyond $A = 0.3$. For $A = 0.4$, we are already producing an output signal with $A_R = 1.92$. Increasing the input voltage to $A = 0.5$ has no effect on the output voltage—at this point, the nonlinearity of the capacitors has been saturated. In Figure 8.5, this corresponds to the part of the graph that is relatively flat.

The net effect of this circuit is to combine and convert the sinusoidal inputs into a soliton-like pulse, as shown in Figure 8.6.

We did not record in Figure 8.5 the wave vectors of the output signals. It is clear that the input signals have wave vectors $\mathbf{k}_1 = (1, 0)$ and $\mathbf{k}_2 = (0, 1)$. Recall from (8.6) that for KP soliton interactions, input signals with these wave vectors would combine to form an output signal with wave vector $\mathbf{k}_3 = (1, 1)$, which is precisely what we observed in all of the experiments we performed to generate Figure 8.5.

8.3.2 Unequal Amplitude and In-Phase

Next we consider the effect of varying the amplitude of the input signals, while keeping these signals in phase. Along the left and bottom boundaries, we prescribe:

$$V_{1,j}(t) = A_L \sin(2\pi ft) \quad (8.15a)$$

$$V_{i,1}(t) = A_B \sin(2\pi ft). \quad (8.15b)$$

Just as for the equal amplitude case, the capacitor model is (8.12) with $b = 0.5$ and $V_M = 1.9$. All other parameters are given in Section 8.2. Using repeated numerical simulations, we compute the amplitude of the output signal A_R for various cases of input signal amplitudes A_L and A_B . The data is recorded in Table 8.1.

Homogeneity of the lattice (8.11) ensures that the table is symmetric across its

	0.4	0.3	0.25	0.2	0.15	0.1
0.4	1.92	1.90	1.90	1.89	1.78	1.73
0.3		1.85	1.39	1.11	0.930	0.799
0.25			1.02	0.845	0.713	0.599
0.2				0.690	0.563	0.467
0.15					0.460	0.368
0.1						0.280

Table 8.1: Amplitude A_R of the outgoing resonant pulse that forms from two incoming sinusoids of amplitude A_L and A_B . All amplitudes are in Volts.

	0.4	0.3	0.25	0.2	0.15	0.1
0.4	2.40	2.71	2.92	3.15	3.24	3.45
0.3		3.08	2.53	2.23	2.07	2.00
0.25			2.04	1.88	1.78	1.71
0.2				1.73	1.61	1.56
0.15					1.53	1.47
0.1						1.40

Table 8.2: Efficiency $A_R/(A_L + A_B)$ (or the ratio of outgoing amplitude to the sum of incoming amplitudes) as a function of A_L and A_B . All amplitudes are in Volts.

diagonal, so only half the entries are shown. In all cases, it is clear that the efficiency ratio $A_R/(A_L + A_B) > 1$, so the wave interaction is always nonlinear, just as in the equal-amplitude case. However, a closer inspection of this ratio, as shown in Table 8.2, reveals an interesting effect. When $A_L < 0.4$, the efficiency increases as A_B increases. However, when $A_L = 0.4$, the efficiency increases as A_B *decreases*. In future work, we shall investigate theoretically the source of this phenomenon.

Other features of the unequal-amplitude case are the same as the equal-amplitude case. Let us specifically mention that input signals colliding at a right angle yield an output pulse that travels at a 45-degree angle. The net effect of the circuit is to generate concentrated soliton-like pulses from sinusoidal inputs.

8.3.3 Equal amplitude but out-of-phase

Finally we consider the effect of varying the interaction angle of the two inputs, while keeping their amplitudes fixed and equal:

$$V_{1,j}(t) = 0.25 \sin(2\pi ft + j\Delta\varphi) \quad (8.16a)$$

$$V_{i,1}(t) = 0.25 \sin(2\pi ft). \quad (8.16b)$$

Each choice of the phase shift $\Delta\varphi$ corresponds to a certain interaction angle θ between the two incoming waves. As an example, the trivial choice of $\Delta\varphi = 0$ corresponds to an interaction angle of $\theta = \pi/2$. In general,

$$\cos \theta = \frac{\lambda \Delta\varphi}{h 2\pi}, \quad (8.17)$$

where h is the distance between two nodes $(i, 1)$ and $(i + 1, 1)$ and λ is the wavelength of the incoming signal. In practice [‡], for an input frequency of 10 GHz, the nonlinear lattice described in Section 8.2 has a ratio $\lambda/h \sim 22.4$. We consider the collision at an angle θ of two waves that begin as sinusoidal forcing (8.16) with phase shift $\Delta\varphi$. From each collision, a resonant outgoing wave with amplitude A_R results. We plot the outgoing amplitude A_R as a function of θ in Figure 8.7.

Note that the efficiency ratio in this case is simply $A_R/(0.25 + 0.25) = 2A_R$. Therefore, it is clear that the resonant collision of maximum efficiency occurs when the interaction angle is 90 degrees. However, if the interaction angle is decreased to 82 degrees, the amplitude of the output signal is decreased only by 7%. For practical applications, even if the interaction angle is not precisely 90 degrees, we still see nonlinear resonant combining.

[‡]The ratio $\lambda/h \sim 22.4$ was established through direct numerical simulation of the nonlinear lattice.

8.4 Practical Considerations

8.4.1 Double resonance.

Of course, there is nothing stopping us from designing circuits that feature multiple resonant interactions. We have numerically simulated such a circuit, based on a 80×40 lattice, i.e., $M = 80$ and $N = 40$, with capacitor model (8.12) and parameters $b = 0.25$, $V_M = 3$. Here the boundary forcing is

$$V_{i,1}(t) = 0.5 \sin(2\pi ft) \quad (8.18a)$$

$$V_{1,j}(t) = 0.5 \sin(2\pi ft) \quad (8.18b)$$

$$V_{i,N}(t) = 0.5 \sin(2\pi ft), \quad (8.18c)$$

where $1 \leq i \leq 20$ and $1 \leq j \leq 40$. With this choice of boundary forcing, three resonant interactions occur. The first two interactions are simultaneous: the wave originating from the bottom $(i, 1)$ boundary nodes collides with the wave originating from the left $(1, j)$ nodes, and at the same time, the wave originating at the top (i, N) collides with the $(1, j)$ wave. The resulting waves have wave vectors of $(1, -1)$ and $(1, 1)$ respectively. These waves then collide at an angle of 90 degrees for a third resonant interaction, producing a single outgoing pulse with wave vector $(1, 0)$. The voltage and power profiles of this pulse are shown in Figure 8.8.

Indeed, this process may be continued, and we may envision a circuit in which numerous input signals are combined nonlinearly to produce a single pulse.

8.4.2 Non-sinusoidal inputs

So far, our study has focused only on input signals which consist of single-frequency sinusoids. The question remains as to whether nonlinear combination is possible given

A (V)	A_R (V)	A_R/A
0.1	0.25	2.50
0.15	0.38	2.53
0.2	0.54	2.70
0.25	0.71	2.84
0.3	0.92	3.07
0.35	1.2	3.49
0.4	1.8	4.50

Table 8.3: Output amplitude A_R (in Volts) and efficiency A_R/A for nonlinear resonance involving two square waves inputs each of amplitude A (in Volts).

input signals with more complicated frequency content, such as

$$V_{1,j}(t) = A \text{sq}(2\pi ft) \quad (8.19a)$$

$$V_{i,1}(t) = A \text{sq}(2\pi ft), \quad (8.19b)$$

where $\text{sq } t$ is a square wave with period 2π :

$$\text{sq } t = \begin{cases} 1 & 0 \leq t < \pi \\ -1 & \pi \leq t < 2\pi \end{cases} \quad (8.20)$$

and $\text{sq}(t + 2\pi K) = \text{sq } t$ for any integer K . Using nonlinear capacitors modeled by (8.12) with $b = 0.5$ and $V_M = 1.9$, we repeatedly simulate the lattice. We find that the lattice combines and converts the two incoming square waves into a single nonlinear pulse. The data, showing the relationship between input and output amplitudes, is given in Table 8.3. Comparison with Figure 8.5 shows that the resonance output amplitude A_R is smaller for square wave inputs than it is for sinusoidal inputs. The reason is that the square wave inputs, unlike the sinusoidal inputs we considered earlier, have their energy spread across the entire Fourier spectrum. The lattice ignores frequencies higher than its own cut-off frequency f_M . Hence a portion of the square wave input signals' energy does not find its way into the output signal, and this is realized as a smaller amplitude A_R than we would have expected for sinusoidal inputs.

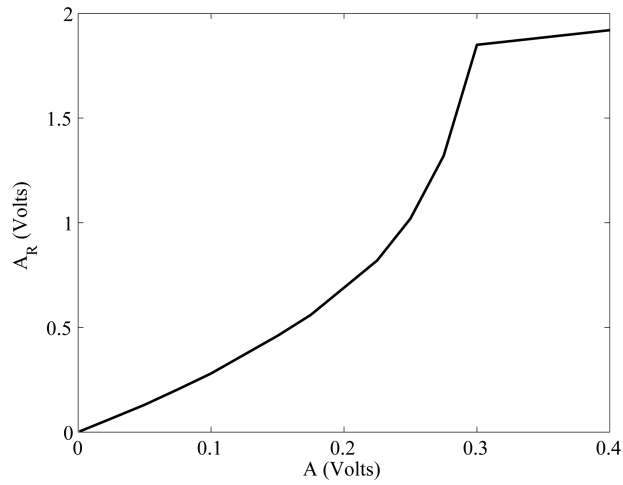
Still, the efficiency ratio of 4.50 seen in the last line of Table 8.3 is twice the ratio of vanilla linear combining in which $A_R = 2A$. We expect that the nonlinear resonance phenomena can be made practical even for extremely wideband signals whose frequency content is in the range of DC to 100 GHz.

8.5 Discussion

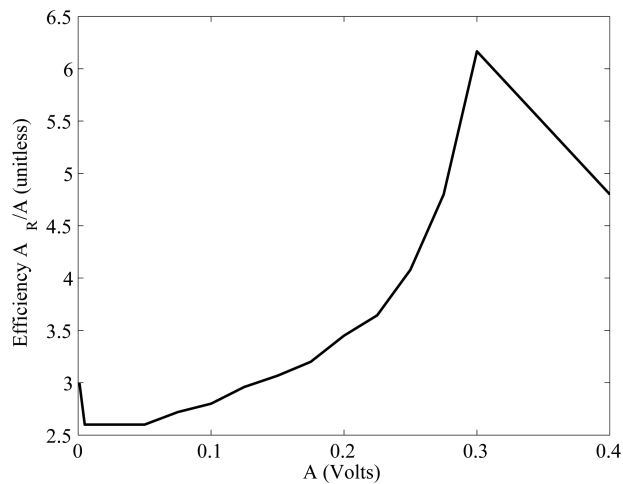
We have provided numerical evidence that KP-like soliton production and nonlinear resonance are possible in a 2-D nonlinear LC lattice. This is true even in the regime where the ratio of amplitude to wavelength may be large. Similar studies have been carried out in other physical contexts, and it is worthwhile to briefly examine the connections.

The infinite 1-D Fermi-Pasta-Ulam (FPU) lattice is one of the most studied nonlinear lattices. It has been known for some time that weakly nonlinear waves in the FPU lattice are governed, in a formal continuum limit, by the Korteweg-de Vries (KdV) equation. More recently, it was shown [70] that sufficiently high-speed pulses in the FPU lattice converge uniformly to KdV solitons, on all length and time scales, not just the ones suggested by weakly nonlinear asymptotics. Might it also be true that pulses in the 2-D nonlinear electrical lattice converge to KP solitons on all length and time scales? It has already been demonstrated that KP-like resonance is possible in the completely integrable 2-D Toda lattice and its discretizations [71].

Both the FPU and Toda lattices are completely integrable dynamical systems; while we do not expect the finite 2-D electrical lattice to be integrable, it would be of considerable interest to determine its higher symmetries. This, along with further exploration of the relationship between nonlinear lattices and continuum models away from the weakly nonlinear regime, will be the subject of future work.



(a) Resonance amplitude



(b) Efficiency ratio

Figure 8.5: Resonance amplitude A_R and efficiency A_R/A as a function of incoming amplitude A , for the case of in-phase, equal amplitude incoming waves, showing (1) the robustness of nonlinear combining ($A_R > 2A$) in all cases; (2) the heightened efficiency for certain input voltages, i.e. two signals of amplitude $A = 0.3V$ combine nonlinearly to produce an $A_R > 6A$ output pulse; and (3) the saturation of output amplitude A_R for high input voltages A .

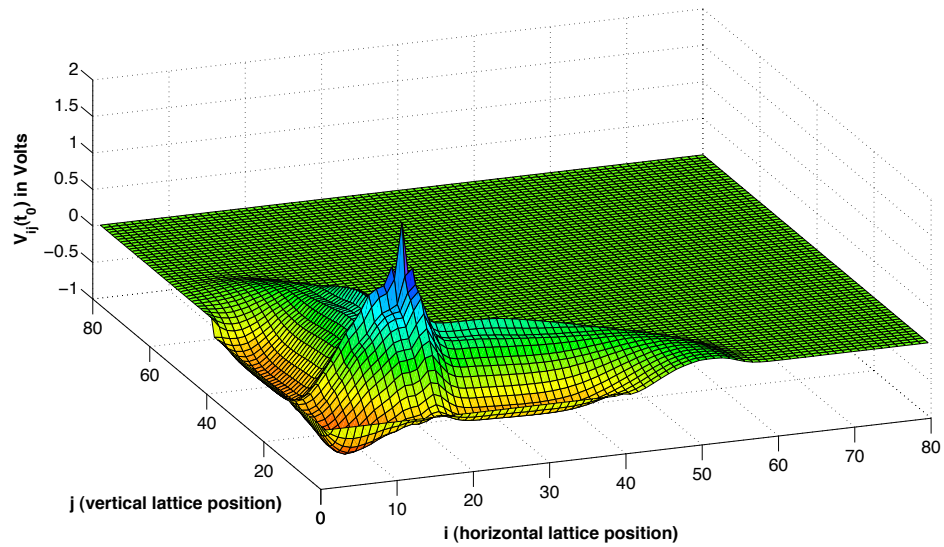


Figure 8.6: Plot of $V_{ij}(t_0)$ for a particular instant of time $t_0 > 0$, showing the generation of a sharp soliton-like nonlinear pulse. The solution shown is for an 80×80 lattice, assuming left- and bottom-boundary input signals (8.14) with equal amplitudes $A_L = A_B = 0.5$. The capacitor model is given by (8.12) with parameters $b = 0.5$ and $V_M = 1.9$.

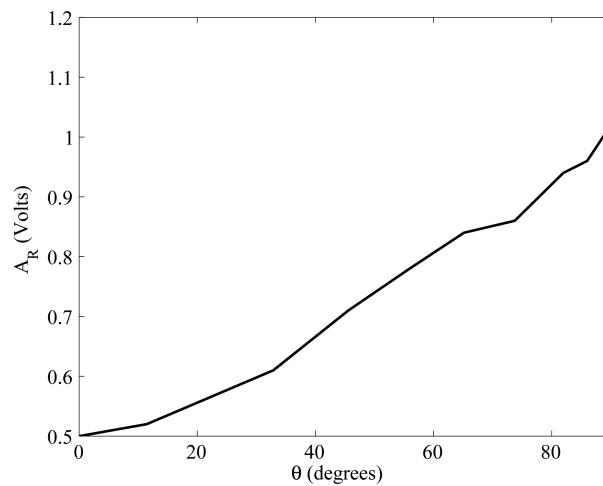


Figure 8.7: Resonance amplitude A_R as a function of interaction angle θ , for the case of incoming waves with equal amplitude $0.25V$.

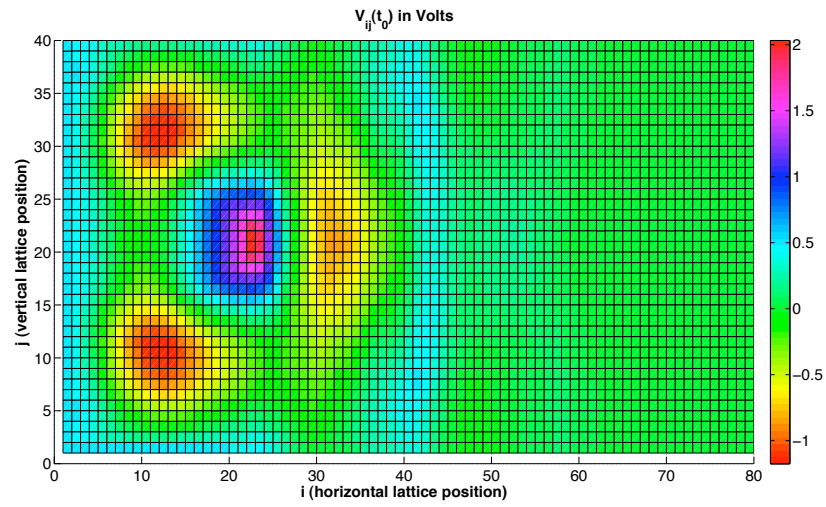
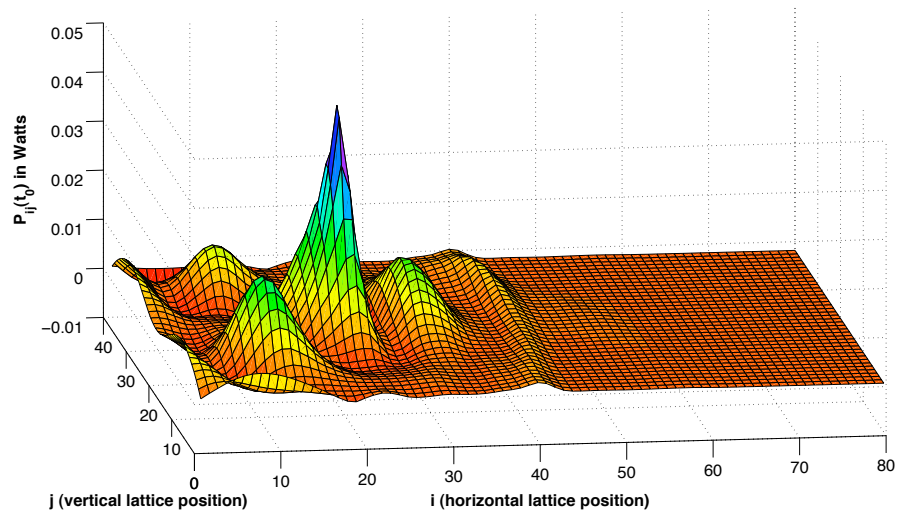
(a) Voltage profile $V_{ij}(t_0)$ (b) Power profile $P_{ij}(t_0)$

Figure 8.8: Voltage $V_{ij}(t_0)$ (in Volts) and power $P_{ij}(t_0) = V_{ij}(t_0)I_{i+1/2,j}(t_0)$ (in Watts) at a particular instant of time $t_0 > 0$ after three nonlinear interactions have occurred, producing a large nonlinear pulse propagating horizontally to the right.

Chapter 9

Optotronics

9.1 Introduction

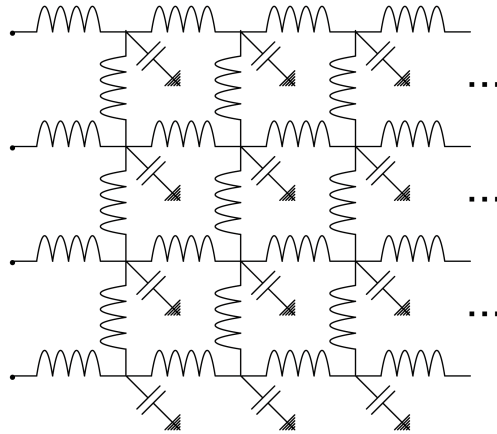


Figure 9.1: Two-dimensional lattice of inductors and capacitors (2-D LC lattice)

Two-dimensional lattices of inductors and capacitors (2-D LC lattices), an example of which is diagrammed in Figure 9.1, are a natural generalization of one-dimensional transmission lines. In a recent investigation [68], both linear and non-linear versions of 2-D LC lattices were proposed for the solution of signal-shaping problems in the frequency range of DC to 100 GHz. One reason for favoring LC lattices is that they are composed only of passive devices, which as compared with active devices do not suffer from limited gain, efficiency, and breakdown voltage. Furthermore, the quality factor for passive components is reasonable enough to allow a

cut-off frequency of approximately 300 GHz, which is difficult to achieve using active device solutions. Hence 2-D LC lattices are reasonable candidates to introduce into high microwave and millimeter-wave integrated circuit design.

In previous chapters, general models for 2-D LC lattices were derived, starting from Kirchhoff's laws of voltage and current. These models consist of partial differential equations (PDE) arising from continuum and quasi-continuum limits, which are valid for signals with frequency content below a certain threshold value. The quasi-continuum models consist of the continuum models plus higher-order dispersive corrections designed to take into account lattice discreteness. Based on the PDE models and numerical simulations, it was found that a 2-D LC lattice could be used to combine the power from various input signals. Such a lattice has been designed and fabricated on chip [69] in a $0.13\mu\text{m}$ SiGe BiCMOS process, where it has been used to implement a power amplifier that generates 125mW at 85 GHz.

Here we apply our continuum model to demonstrate that 2-D LC lattices can, if configured in a certain way, generate approximate Fourier transforms of input signals. Let us be more specific about this claim. Suppose we are given an input vector of length M , denoted by $\mathbf{x} \in \mathbb{R}^M$. In this case, we work with a 2-D LC lattice that has N nodes in the horizontal direction and M nodes in the vertical direction. For definiteness, in this work we use $(1, 1)$ and (N, M) to denote, respectively, the lower-left and upper-right corners of the lattice. We drive the left boundary of the lattice with the voltage

$$V_{1,j}(t) = \alpha_1 x_j \sin(2\pi\omega t), \quad 1 \leq j \leq M,$$

where α_1 is an appropriate scaling factor, x_j is the j -th component of the input vector \mathbf{x} , and ω is an appropriate carrier frequency. Later in this chapter we describe how to choose the lattice inductances L_{ij} and capacitances C_{ij} in a certain way, to take advantage of electrical analogues of optical phenomena such as refraction and diffraction. Our claim is that in such a lattice, the voltage at the right boundary will take the form

$$V_{N,j}(t) = \alpha_2 y_j \sin(2\pi\omega t), \quad 1 \leq j \leq M.$$

Here α_2 is an appropriate scaling factor, y_j is the j -th component of the output vector \mathbf{y} , and

$$\mathbf{y} \approx \hat{\mathbf{x}},$$

where $\hat{\mathbf{x}}$ is the exact discrete Fourier transform of \mathbf{x} . We may think of \mathbf{y} and $\hat{\mathbf{x}}$ as M -vectors of phasors, or, equivalently, as elements of the complex vector space \mathbb{C}^M .

9.2 Methodology and Merits

As mentioned, our solution takes advantage of the connection between 2-D LC lattices in optics. For waves with sufficiently large wavelength, Kirchhoff's laws of voltage and current for a 2-D LC lattice can be approximated very well by a continuum model consisting of the scalar wave equation. The same PDE arises in the context of optics; starting from this PDE, the theories of Kirchhoff, Sommerfeld, Fresnel, and Huygens show that a thin-slit diffraction aperture can be used to generate an analog Fourier transform of an image. Such theories assume, typically, that light propagates in a 3-D continuum such as air. In this chapter, we present analytical and numerical results for thin-slit diffraction in a 2-D LC lattice. Together, these results indicate that by choosing lattice capacitance/inductance, lattice size, and input carrier frequency in a careful way, we can design 2-D LC lattices that generate analog Fourier transforms in the same way as a thin-slit diffraction aperture for 3-D optics.

This is almost the entire solution. Our analysis also indicates that, by itself, the output through a 2-D thin-slit diffraction suffers a phase shift that can be corrected using a lens. We show through numerical simulations that a 2-D LC lattice can be used to refract incoming waves, and therefore that such a lattice can be used as a lens. Our Fourier transform device, therefore, is effectively the superposition of a diffractive lattice with a lattice-based lens. The combination of these effects yields an in-phase analog Fourier transform.

Using a 2-D LC lattice as an approximate Fourier transform device has three distinct features. First, the latency of the device, defined as the time required for the

input signal to propagate from the left to the right boundary, can be extremely small. The latency is computed by multiplying the characteristic delay of the lattice, τ , by the number of nodes in the horizontal direction. The delay τ can be as low as 1 psec for today's Silicon processes. As a rule of thumb, we find that to transform a vector with M components requires a lattice with roughly $N = (5/4)M$ nodes in the horizontal direction. As a function of M , the latency is $(5/4)M\tau$. Using a 2-D LC lattice, a vector of length 1024 could be transformed in less than 0.2 ns. Note that the latency is independent of the carrier frequency ω , and that it grows linearly in the size of the input vector M .

Second, the device throughput can be extremely high. One does not need to wait for an input signal to propagate all the way from the left boundary to the right boundary of the lattice before injecting a new, different input signal. Inputs could be stacked in time, and multiple Fourier transforms could be computed without waiting. Preliminary simulations indicate that the throughput of the lattice can reach 10 Gbits/sec.

Finally, in a 2-D LC lattice, we are able to vary both inductance and capacitance independently, enabling us to create lattices that have large changes in the delay (refraction index) while keeping impedance constant, or vice versa. Let us remark that engineering LC lattices is easier and less expensive than engineering optical materials with similar properties.

9.3 Historical Remarks

Classic texts [90][91], on wave and Fourier optics concentrate their efforts on three-dimensional media, ostensibly because most experimental diffraction setups involve light propagation in three spatial dimensions. However, the propagation of light in two-dimensional media has been considered before. Diffraction integrals for a two-dimensional dispersion-free continuum were almost surely known to Sommerfeld—see, for example, equations (2.23)-(2.26) of Bouwkamp's survey article[92] and references therein. Recent work in this area is due to J. J. Stamnes [93][94][95][96][97], who

has derived exact, approximate, and numerical results for focusing and diffraction of two-dimensional waves. Stamnes' results stop short of showing that even for 2-D waves, a standard Fourier transform integral can be derived. Furthermore, Stamnes' work deals exclusively with waves propagating through a dispersionless continuum, which describes our discrete 2-D LC lattice only approximately, and only in certain frequency regimes. Other papers on 2-D diffraction [98][99] do not differ in this regard.

Our work owes a great deal to the classical approaches of Sommerfeld and Kirchhoff, also employed by Stamnes. Their approach for single-slit diffraction problems consists primarily in using one of Green's identities to express the diffracted field at a point P_0 in terms of a particular integral around a curve centered at P_0 . Denote this integral by $I(P_0)$. Next, assume that the spatial part of the diffracted field is a solution of the Helmholtz equation

$$(\nabla^2 + k^2) \psi = 0. \tag{9.1}$$

Knowledge of the radially symmetric solutions of (9.1), together with a choice of boundary conditions for the field and its normal derivative on the aperture of the slit, enables us to pass from the integral $I(P_0)$ to a diffraction integral. In the present work, we validate our numerical results on diffraction using this classical approach.

The main alternative to the Kirchhoff-Sommerfeld approach outlined above is the geometric or ray theory of diffraction due to Keller[100; 101] and his collaborators. Application of Keller's elegant methods to the context of 2-D LC lattices shall have to wait until a future publication.

Finally, let us note that the classical work [33] of Brillouin on crystal lattices makes explicit the analogy between crystal lattices, mass-spring models, and LC lattices in one, two, and three spatial dimensions. Brillouin's primary focus in this work was the development of band-gap theories for lattices with periodic inhomogeneities. The lattice inhomogeneities we consider are of an entirely different type.

9.4 Lattice Equations and PDE Models

9.4.1 Kirchhoff's Laws

For a two-dimensional LC lattice that extends infinitely in both directions, Kirchhoff's laws of voltage and current read:

$$I_{i,j-1/2} + I_{i-1/2,j} - I_{i+1/2,j} - I_{i,j+1/2} = C_{ij} \frac{d}{dt} V_{ij}, \quad (9.2a)$$

$$V_{i,j-1} - V_{ij} = L_{i,j-1/2} \frac{d}{dt} I_{i,j-1/2}, \quad (9.2b)$$

$$V_{ij} - V_{i+1,j} = L_{i+1/2,j} \frac{d}{dt} I_{i+1/2,j}. \quad (9.2c)$$

Here we have assumed that the capacitances C_{ij} and the inductances $L_{\alpha\beta}$ stay fixed as a function of time. Otherwise the right-hand sides of (9.2) would have to be modified, and the dynamics of the lattice would be nonlinear. In contrast, system (9.2) is linear.

9.4.2 Continuum Limit

In [68], the continuum limit of (9.3) was derived using standard Taylor series arguments. In the case of a uniform lattice, one can arrive at a continuum limit simply by examining the dispersion relation, a procedure we now describe. Take $C_{ij} = C$ and $L_{\alpha,\beta} = L$ everywhere, differentiate (9.2a) with respect to time, and then substitute (9.2b-9.2c) to derive the single second-order equation for lattice voltage:

$$(V_{i-1,j} - 2V_{i,j} + V_{i+1,j} + V_{i,j-1} - 2V_{i,j} + V_{i,j+1}) = LC\ddot{V}_{ij}. \quad (9.3)$$

Assume that the spacing between lattice elements is the same in both x and y direction, and denote this constant lattice spacing by d . Then making the ansatz

$$V_{i+1,j}(t) = e^{ik_x d} V_{i,j}(t), \quad V_{i,j+1}(t) = e^{ik_y d} V_{i,j}(t), \quad V_{i,j}(t) = e^{-i\omega t},$$

one derives the dispersion relation

$$\omega = \frac{2}{\sqrt{LC}} \left[\sin^2 \frac{k_x d}{2} + \sin^2 \frac{k_y d}{2} \right]^{1/2}. \quad (9.4)$$

When $\theta \ll 1$, we may approximate $\sin \theta \approx \theta$. Therefore, when $k_x d \ll 1$ and $k_y d \ll 1$, the dispersion relation may be approximated by

$$\omega = \frac{d}{\sqrt{LC}} [k_x^2 + k_y^2]^{1/2}. \quad (9.5)$$

Replace L by $d\ell$ and C by dc , where ℓ and c are, respectively, inductance and capacitance per unit length. Assuming that ℓ and c stay constant in the $d \rightarrow 0$ limit, we arrive at the *continuum* dispersion relation

$$\omega = \frac{1}{\sqrt{\ell c}} [k_x^2 + k_y^2]^{1/2}, \quad (9.6)$$

which is the exact dispersion relation for the scalar wave equation

$$\nabla^2 v = \ell c \frac{\partial^2 v}{\partial t^2}. \quad (9.7)$$

In previous derivations[68], we started with (9.3), then posited a continuous function $v(x, y, t)$ such that $v(id, jd, t) \approx V_{ij}(t)$, expanded $V_{i+\sigma, j}$ and $V_{i, j+\sigma}$ in Taylor series about $V_{i, j}$, and thereby derived precisely the same PDE model (9.7). The derivation of (9.7) as a continuum model of (9.3) on the basis of exact/approximate dispersion relations has its own utility, as we now show.

9.4.3 Range of Validity

One wants to understand, quantitatively, where the continuum model (9.7), is valid. First off, one can easily determine that the relative error in the approximation $\sin^2 \theta \approx \theta^2$ is less than 2.5% for $|\theta| < 1/4$. Hence we want $k_x d < 1/4$ and $k_y d < 1/4$. Because

wavelength is related to wave number by $\lambda = 2\pi/k$, the conditions on k_x and k_y imply

$$\frac{\lambda_x}{d}, \frac{\lambda_y}{d} > \frac{2\pi}{1/4} \approx 25.$$

As long as one wavelength of the lattice wave occupies more than 25 lattice spacings, the continuum dispersion relation (9.6) and PDE (9.7) is a decent approximation to the fully discrete dispersion relation (9.4) and differential equation (9.3).

We may go further. For the sake of illustration, let us fix the inductance and capacitance to be, respectively, $L = 30\text{pH}$ and $C = 20\text{fF}$. Inductors and capacitors with these values (and somewhat smaller values) can be fabricated in today's Silicon processes; at values that are much smaller, parasitic effects become an issue. Suppose waves of frequency ω propagate through such a lattice, in the x direction only. In this case $k_y = 0$. The dispersion relation (9.4) may now be used to determine that, with these parameters,

$$k_x d = 2 \sin^{-1} \frac{\omega}{2.6 \times 10^{12}}.$$

Then $k_x d < 1/4$ as long as $\omega < 52\text{GHz}$, the cut-off frequency for validity of the continuum model of the 2-D LC lattice. Note also that is easy to read off the cut-off frequency ω_M for the lattice itself from the above calculation:

$$\omega_M \approx 2.6 \times 10^{12} \text{sec}^{-1} \approx 410\text{GHz}.$$

9.4.4 Dispersive Correction

If one seeks a PDE model for (9.3) with an extended range of validity, one way to proceed is to use higher-order terms when approximating \sin in (9.4). That is, starting with (9.4), we use a two-term Taylor series approximation for $\sin \theta$, resulting in

$$\sin^2 \theta \approx \theta^2 - \frac{\theta^4}{3}. \quad (9.8)$$

The resulting approximate dispersion relation is

$$\omega = \frac{d}{\sqrt{\ell c}} \left[k_x^2 + k_y^2 - \frac{d^2}{12} (k_x^4 + k_y^4) \right]^{1/2}. \quad (9.9)$$

This dispersion relation is the exact dispersion relation for the scalar PDE

$$\nabla^2 v + \frac{d^2}{12} \nabla^4 v = \ell c \frac{\partial^2 v}{\partial t^2}, \quad (9.10)$$

where ∇^4 is the bilaplacian operator

$$\nabla^4 = \frac{\partial^4}{\partial x^4} + \frac{\partial^4}{\partial y^4}. \quad (9.11)$$

Equation (9.10), derived previously[68] using Taylor series approximations, is a quasi-continuum model for the discrete equation (9.3). To evaluate where this model is valid, consider that the relative error in the approximation (9.8) is now less than 2.5% for $|x| < 1$. Repeating the above calculation in this case, we obtain the conditions

$$\frac{\lambda_x}{d}, \frac{\lambda_y}{d} > 2\pi \approx 6.$$

As long as lattice waves occupy at least 7 lattice spacings, the dispersion relation (9.9) closely matches the true dispersion relation (9.4). Using the full dispersion relation (9.4), we determine that this condition holds for plane waves moving in the x direction when $\omega < 198\text{GHz}$, assuming as before a uniform lattice with inductance $L = 30\text{pH}$ and $C = 20\text{fF}$.

9.4.5 Effect of Boundaries

Of course, experimentally realizable lattices must be of finite extent. Furthermore, when we numerically simulate the lattice equations, we must take into account appropriate boundary conditions that arise due to finiteness of the lattice. For these reasons we give a few details regarding Kirchhoff's laws on the boundaries.

For a finite lattice with M nodes in the x direction and N nodes in the y direction,

we see that

Equation (9.2a) holds for $2 \leq i \leq M, 2 \leq j \leq N$,

Equation (9.2b) holds for $1 \leq i \leq M, 2 \leq j \leq N$, and

Equation (9.2c) holds for $1 \leq i \leq M - 1, 1 \leq j \leq N$.

Equations (9.2b-9.2c) already take into account contributions due to voltage nodes on the boundary and need not be modified. Meanwhile, equation (9.2a) for $i = 1$, $i = M$, $j = 1$, and $j = N$ must be corrected by deleting those terms on the left-hand side corresponding to edges outside the lattice. Furthermore, we assume the right boundary of the lattice is resistively terminated with resistors obeying Ohm's law, so that the equations for $i = M$ read:

$$C_{M,j} \frac{d}{dt} V_{M,j} = \begin{cases} I_{M-1/2,j} - I_{M,j+1/2} - V_{M,j} R_j^{-1} & j = 1 \\ I_{M,j-1/2} + I_{M-1/2,j} - I_{M+1/2,j} - V_{M,j} R_j^{-1} & 2 \leq j \leq N - 1 \\ I_{M,j-1/2} + I_{M-1/2,j} - V_{M,j} R_j^{-1} & j = N. \end{cases}$$

The resistances R_j are chosen to minimize the reflection coefficient for waves incident on the right boundary. This is a basic impedance matching problem, and for a uniform medium the solution is given by choosing $R = \sqrt{L/C}$ everywhere along the right boundary.

9.5 Refraction

9.5.1 Snell's law

Figure (9.2) shows the simplest scenario: a 2-D LC lattice with a jump in the delay, $\tau = \sqrt{LC}$, along a horizontal interface. That is to say, above the interface, the delay equals $\tau_1 = \sqrt{L_1 C_1}$, while below the interface, the delay equals $\tau_2 = \sqrt{L_2 C_2}$. The incident wave arrives at the interface (from above) at an angle θ^I and is partly

reflected at an angle θ^R , and partly transmitted at an angle θ^T .

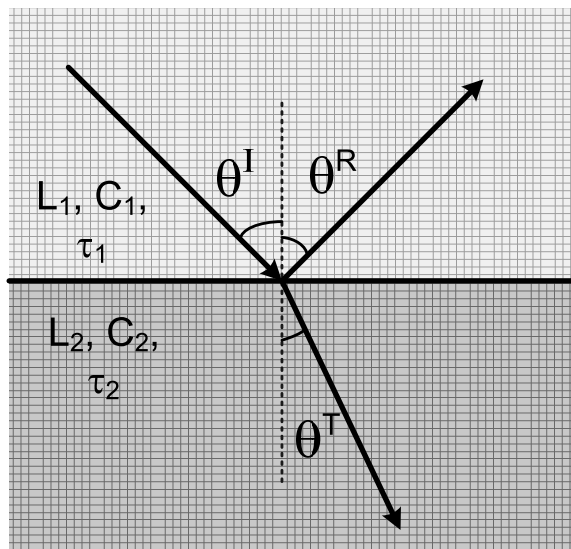


Figure 9.2: Incident, reflected, and transmitted waves in a simple refraction problem

The continuum model for the lattice is given by (9.7), repeated here:

$$\nabla^2 V = \tau^2 \frac{\partial^2 V}{\partial t^2} \quad (9.12)$$

where V is the voltage and $\tau = \sqrt{LC}$. By assuming that the incident, reflected, and transmitted waves are plane wave solutions of (9.12), propagating with the appropriate dispersion relation depending on whether they are in the upper or lower halves of the lattice, one can apply standard arguments to derive $\theta^I = \theta^R$, as well as Snell's law:

$$\frac{\sin \theta^T}{\sin \theta^I} = \frac{\tau_1}{\tau_2}. \quad (9.13)$$

The derivation of (9.13) starting from (9.12) is completely standard[90; 91] and we shall not repeat it here. Instead, let us examine the effect of discreteness on the simple refraction problem—more specifically, let us derive a version of Snell's law that accounts (to lowest order) for the dispersion induced by discreteness. Suppose that the incident, reflected, and transmitted waves are solutions of the dispersive,

quasi-continuum model

$$\nabla^2 V + \frac{h^2}{12} \nabla^4 V = \tau^2 \frac{\partial^2 V}{\partial t^2}, \quad (9.14)$$

where ∇^4 is the bilaplacian defined in (9.11). This equation has plane wave solutions of the form

$$V = \exp(i(\mathbf{k} \cdot \mathbf{x} - \omega t))$$

as long as frequency ω and wave number \mathbf{k} are related by the dispersion relation

$$\omega^2 = \frac{1}{\tau^2} \left[\|\mathbf{k}\|^2 - \frac{h^2}{12} (k_x^4 + k_y^4) \right].$$

With this dispersion relation, we consider the standard refraction problem, and assume plane wave forms

$$\begin{aligned} V^I &= \exp(i(\mathbf{k}^I \cdot \mathbf{x} - \omega^I t)) \\ V^R &= R \exp(i(\mathbf{k}^R \cdot \mathbf{x} - \omega^R t)) \\ V^T &= T \exp(i(\mathbf{k}^T \cdot \mathbf{x} - \omega^T t)) \end{aligned}$$

for incident, reflected, and transmitted voltage. By matching voltages at the interface $y = 0$, we obtain

$$\exp i(k_x^I x - \omega^I t) + R \exp i(k_x^R x + \omega^R t) = T \exp i(k_x^T x - \omega^T t), \quad (9.15)$$

which must be true for all x and all t . Therefore, we must have the following equalities:

$$k_x^R = k_x^T = k_x^I \quad (9.16)$$

$$\omega^R = \omega^T = \omega^I \quad (9.17)$$

These equalities are quite useful in the following derivation. The derivation of a dispersively corrected version of Snell's law begins by noticing from the geometry of the problem that

$$\frac{\sin \theta^T}{\sin \theta^I} = \frac{\|\mathbf{k}^I\|}{\|\mathbf{k}^T\|}. \quad (9.18)$$

The procedure from here onwards consists of using equalities (9.16-9.17) together with the dispersion relations in the $y < 0$ and $y > 0$ half-planes to try and express the right-hand side of (9.18) in terms of incident wave number \mathbf{k}^I , the lattice spacing h , and the delays τ_1 and τ_2 . Assuming we have done that, we can expand the right-hand side in powers of h . At order h^0 we expect to recover the non-dispersive Snell's law (9.13).

We begin by rearranging the dispersion relation in the $y < 0$ half-plane to write

$$\|\mathbf{k}^T\| = \sqrt{\tau_2^2 \omega^2 + \frac{h^2}{12} [k_x^{T4} + k_y^{T4}]},$$

which we then substitute into the denominator of (9.18), producing

$$\frac{\sin \theta^T}{\sin \theta^I} = \sqrt{\frac{k_x^{I2} + k_y^{I2}}{\tau_2^2 \omega^2 + \frac{h^2}{12} [k_x^{I4} + k_y^{I4}]}}. \quad (9.19)$$

Here we have used $k_x^T = k_x^I$. The dispersion relation for ω^I reads

$$\omega^2 = \frac{1}{\tau_1^2} \left[\|\mathbf{k}^I\|^2 - \frac{h^2}{12} (k_x^{I4} + k_y^{I4}) \right].$$

Substituting this into (9.19) and squaring both sides gives

$$\left(\frac{\sin \theta^T}{\sin \theta^I} \right)^2 = \frac{k_x^{I2} + k_y^{I2}}{\tau_2^2 \tau_1^{-2} [k_x^{I2} + k_y^{I2} - \frac{h^2}{12} (k_x^{I4} + k_y^{I4})] + \frac{h^2}{12} [k_x^{I4} + k_y^{I4}]}, \quad (9.20)$$

As regards the y -component of the outgoing wave vector, k_y^T , using $\omega^T = \omega^I$ and the dispersion relation, we write

$$\frac{1}{\tau_1^2} \left[\|\mathbf{k}^I\|^2 - \frac{h^2}{12} (k_x^{I4} + k_y^{I4}) \right] = \frac{1}{\tau_2^2} \left[\|\mathbf{k}^T\|^2 - \frac{h^2}{12} (k_x^{T4} + k_y^{T4}) \right]. \quad (9.21)$$

After substituting $k_x^T = k_x^I$, we use the quadratic formula to solve for k_y^{T2} as a function

of \mathbf{k}^I . The result is

$$k_y^{T2} = \frac{6\tau_1^2 \mp \sqrt{(-h^4 k_x^{I4} + 12h^2 k_x^{I2} + 36) \tau_1^4 + h^2 (h^2 k_x^{I4} - 12k_x^{I2} + h^2 k_y^{I4} - 12k_y^{I2}) \tau_2^2 \tau_1^2}}{h^2 \tau_1^2}, \quad (9.22)$$

and we choose the root with a negative sign, because its $h \rightarrow 0$ limit reproduces the non-dispersive relationship

$$k_y^{T2} = \frac{\tau_2^2}{\tau_1^2} (k_x^{I2} + k_y^{I2}) - k_x^{I2}.$$

Finally, we substitute (9.22) in (9.20) and obtain a lengthy expression that depends only on τ_1 , τ_2 , h , and \mathbf{k}^I . Taylor expansion of this expression in powers of h gives a dispersive $O(h^2)$ correction to Snell's law:

$$\left(\frac{\sin \theta^T}{\sin \theta^I} \right)^2 = \frac{\tau_1^2}{\tau_2^2} + h^2 \left[\frac{(1 - \tau_1^2/\tau_2^2) (2k_x^{I4} \tau_1^2/\tau_2^2 - \|\mathbf{k}^I\|^4)}{6 \|\mathbf{k}^I\|^2} \right] + O(h^4). \quad (9.23)$$

Note that the dispersive correction depends on τ_1 and τ_2 only through the ratio τ_1/τ_2 . Note also that when $\tau_1 = \tau_2$, the $O(h^2)$ term vanishes and we recover $\sin \theta^T = \sin \theta^I$.

Let us rewrite (9.23) slightly by factoring out $\|\mathbf{k}^I\|^2$ from the $O(h^2)$ term:

$$\left(\frac{\sin \theta^T}{\sin \theta^I} \right)^2 = \frac{\tau_1^2}{\tau_2^2} + \frac{h^2 \|\mathbf{k}^I\|^2}{6} \left(1 - \frac{\tau_1^2}{\tau_2^2} \right) \left(2 \frac{k_x^{I4}}{\|\mathbf{k}^I\|^4} \frac{\tau_1^2}{\tau_2^2} - 1 \right) + O(h^4).$$

Note that

$$\frac{k_x^{I4}}{\|\mathbf{k}^I\|^4} = \sin^4 \theta^I.$$

Next, assuming $h\|\mathbf{k}^I\|$ is small, we may use $\sqrt{\alpha^2 + \phi} \approx \alpha + \phi/(2\alpha)$ to write

$$\frac{\sin \theta^T}{\sin \theta^I} = \frac{\tau_1}{\tau_2} + \frac{h^2 \|\mathbf{k}^I\|^2}{12} \left(1 - \frac{\tau_1^2}{\tau_2^2} \right) \left(2 \sin^4 \theta^I \frac{\tau_1^2}{\tau_2^2} - 1 \right) \frac{\tau_2}{\tau_1} + O(h^4). \quad (9.24)$$

Given θ^I , h , and τ_1/τ_2 , it is easy to evaluate this formula to obtain the refracted angle θ^T .

9.5.2 Thick Parabolic Lens

Suppose we have a parabolic lens described by $F(x, y) = 0$ where

$$F(x, y) = x - \frac{\alpha}{2}y^2.$$

The curve $F(x, y) = 0$ is the left boundary of the lens. The right boundary of the lens is taken to be a vertical line as in Figure 9.3.

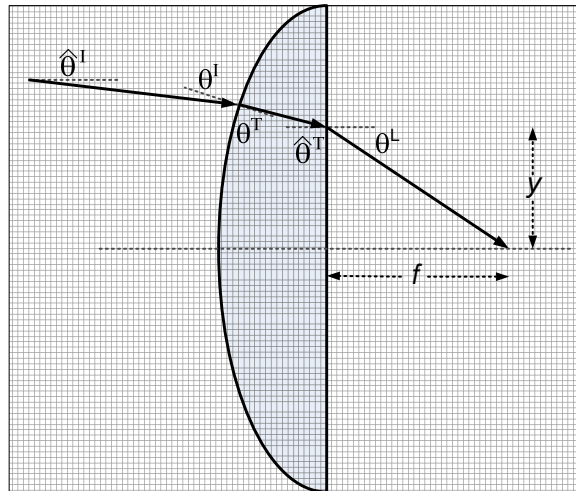


Figure 9.3: Refraction problem for thick parabolic lens

Suppose we have a wave front propagating from left to right at angle $\hat{\theta}^I$, incident on the left boundary of the lens. The wave front's angle from the normal is given by

$$\theta^I = \hat{\theta}^I + \tan^{-1}(\alpha y).$$

We use Snell's law to compute the angle of the transmitted wave:

$$\sin \theta^T = \frac{\tau_1}{\tau_2} \sin \theta^I = \frac{\tau_1}{\tau_2} \sin \left(\hat{\theta}^I + \tan^{-1}(\alpha y) \right).$$

Of course, θ^T is the angle the transmitted wave front makes with the normal to the

curved part of the lens. Subtracting off the contribution of this normal, we obtain

$$\begin{aligned}\hat{\theta}^T &= \theta^T - \tan^{-1}(\alpha y) \\ &= \sin^{-1} \left[\frac{\tau_1}{\tau_2} \sin \left(\hat{\theta}^I + \tan^{-1}(\alpha y) \right) \right] - \tan^{-1}(\alpha y)\end{aligned}$$

The angle $\hat{\theta}^T$ is the angle of incidence for the refraction problem at the right boundary of the lens. This is a simple consequence of the fact that the right boundary of the lens is vertical. We apply Snell's law again to determine the angle of the outgoing wave that is transmitted through the right boundary of the lens:

$$\begin{aligned}\sin \theta^L &= \sin \hat{\theta}^T \frac{\tau_2}{\tau_1} \\ &= \sin \left\{ \sin^{-1} \left[\frac{\tau_1}{\tau_2} \sin \left(\hat{\theta}^I + \tan^{-1}(\alpha y) \right) \right] - \tan^{-1}(\alpha y) \right\} \frac{\tau_2}{\tau_1}\end{aligned}$$

Simple geometry shows that

$$\frac{y}{f} = \tan \theta^L,$$

where f is the focal distance. This implies that

$$f = \frac{y}{\tan \theta^L} = y \left[\tan \sin^{-1} \left(\sin \left\{ \sin^{-1} \left[\frac{\tau_1}{\tau_2} \sin \left(\hat{\theta}^I + \tan^{-1}(\alpha y) \right) \right] - \tan^{-1}(\alpha y) \right\} \frac{\tau_2}{\tau_1} \right) \right]^{-1}.$$

9.5.3 Paraxial Approximation

Note that we can easily recover the paraxial approximation from the above formula for f . First set $\hat{\theta}^I = 0$. Next assume $\alpha \ll 1$, which in essence converts all of the nonlinear functions \tan and \sin to the identity, i.e., if $q = O(\alpha)$, then

$$\tan q \approx q, \quad \sin q \approx q,$$

and likewise for the inverse functions. One obtains for the denominator of f the approximation

$$\begin{aligned} \tan \sin^{-1} \left(\sin \left\{ \sin^{-1} \left[\frac{\tau_1}{\tau_2} \sin \left(\hat{\theta}^I + \tan^{-1}(\alpha y) \right) \right] - \tan^{-1}(\alpha y) \right\} \frac{\tau_2}{\tau_1} \right) &\approx \left\{ \frac{\tau_1}{\tau_2} \alpha y - \alpha y \right\} \frac{\tau_2}{\tau_1} \\ &\approx \left(1 - \frac{\tau_2}{\tau_1} \right) \alpha y. \end{aligned}$$

Therefore f can be approximated by

$$f \approx \frac{y}{\left(1 - \frac{\tau_2}{\tau_1} \right) \alpha y} = \frac{1}{\alpha \left(1 - \frac{\tau_2}{\tau_1} \right)}.$$

9.5.4 Numerics

We simulate the lattice by solving Kirchoff's laws (9.2) for an 80×80 lattice with boundary conditions given in Section 9.4.4 of this work. For these simulations, we have one (or more) vertical interface separating two (or more) sections of the lattice. In certain sections of the lattice, we have $L_1 = 1\text{nH}$ and $C_1 = 1\text{pF}$, while in other sections, we have

$$L_2 = L_1/\sqrt{10}, \quad C_2 = C_1/\sqrt{10}.$$

For the purposes of the following discussion, we define the following lattice delay constants:

$$\begin{aligned} \tau_1 &= \sqrt{L_1 C_1} = 10^{-10.5} \text{sec}^{-1} \\ \tau_2 &= \sqrt{L_2 C_2} = 10^{-11} \text{sec}^{-1}. \end{aligned}$$

In all simulations that follow, the frequency in time of the boundary forcing is $\omega = 1\text{G rad/sec}$.

Snell's law. For the first simulation, we take the lattice to have a single interface at $i = 30$. For $i < 30$, the delay is τ_1 , while for $i > 30$, the delay is τ_2 . Hence the effective index of refraction is $\tau_1/\tau_2 = \sqrt{10}$. The incident angle, for the wave propagating from

the left boundary towards the interface, is approximately

$$\theta^I \approx 0.149 \text{ rad},$$

and based on Snell's law we predict a transmitted angle

$$\theta^T \approx 0.488 \text{ rad},$$

which is exactly what we see in the numerical simulation results displayed in Figure 9.4. The black lines are drawn to match the incident and refracted wave vectors, as

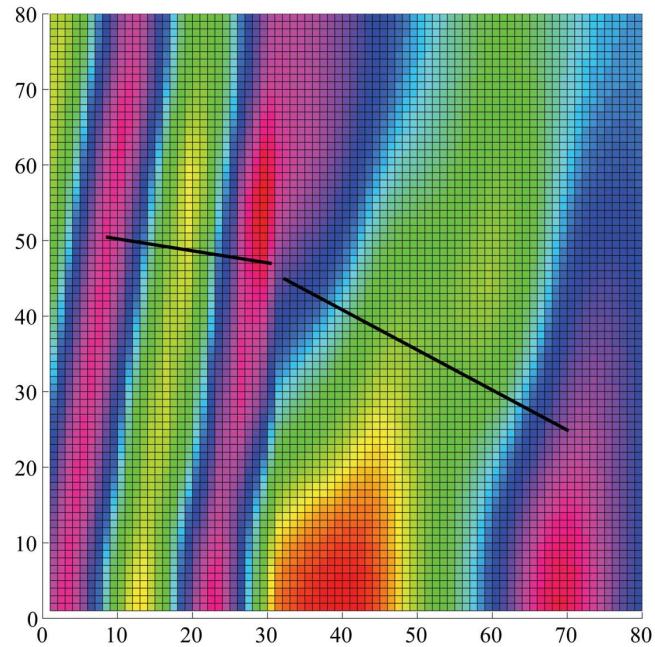


Figure 9.4: Refraction in a 2-D LC lattice, showing the validity of Snell's law. The black lines show incident and refracted wave vectors predicted by Snell's law. Colors correspond to level sets of the voltage $V_{ij}(t)$, at a particular instant of time $t > 0$. At $t = 0$, voltage forcing is switched on along the left boundary; resulting waves propagate at an angle, towards the interface at $i = 30$, where they are refracted, causing a change in the direction and wavelength of the wave. For $i < 30$, the lattice delay equals τ_1 , while for $i > 30$, the lattice delay equals τ_2 .

predicted by Snell's law. Note that the black line in the $i > 30$ region is orthogonal

to the numerically generated wavefronts. This implies that, in the direct numerical simulation, the angle that the refracted waves make with the normal to the interface is given quite accurately by Snell's law.

Plane waves refracted by a slab. Next we examine a section of lattice with delay τ_2 sandwiched between two sections with delay τ_1 . Here we take the incident angle to be zero, and note the change in wavelength of the wave as it propagates in the τ_2 section—see Figure 9.5. Here the delay is τ_1 for $i < 20$ and $i > 70$, and the delay is τ_2

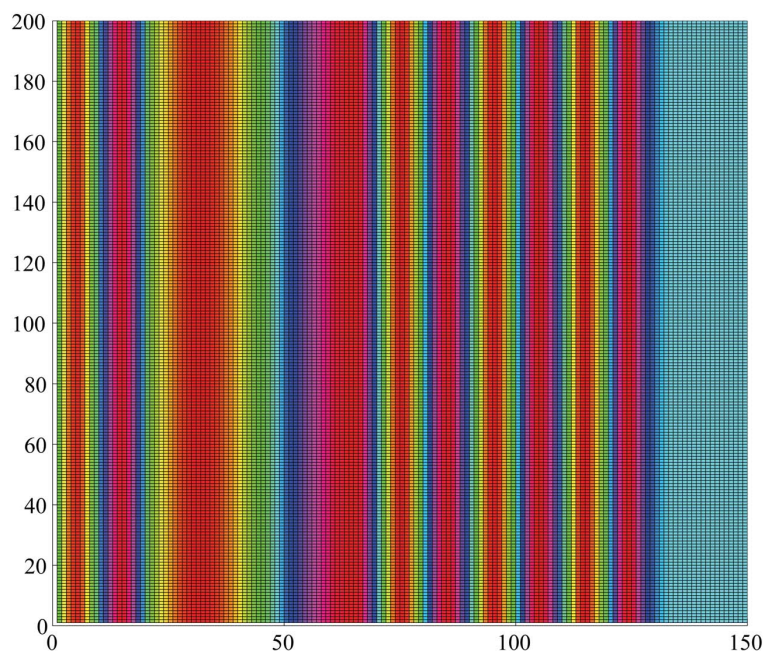


Figure 9.5: Plane slab showing pure transmission and wavelength expansion in the $20 \leq i \leq 70$ section. Colors correspond to level sets of the voltage $V_{ij}(t)$, at a particular instant of time $t > 0$. At $t = 0$, voltage forcing is switched on along the left boundary; resulting waves propagate to the right, towards the interface at $i = 20$, where they are refracted, causing a change in wavelength. At $i = 70$, the wave encounters a second interface and is refracted again, causing the wavelength to return to its original value. The lattice delay equals τ_1 except inside the $20 \leq i \leq 70$ section, where the delay equals τ_2 .

for $20 \leq i \leq 70$. Waves propagate from the left boundary towards the first interface at $i = 20$, undergo refraction and a change in wavelength, and continue propagating

to the right until they are refracted again at the $i = 70$ interface, at which point their wavelength increases back to its original value. Impedance is matched at both interfaces so there is no reflection, i.e., there is no wave propagating from right to left from the interface back towards the left boundary.

Total internal reflection. Finally we present simulation results showing total internal reflection. Here the wave is launched from the left boundary and, more specifically, from the lower-left corner of the lattice consisting of the first 20 nodes $1 \leq j \leq 20$ on the left boundary. The nodes on the left boundary with $j > 20$ are left open, meaning that waves will reflect perfectly off those nodes. The wave propagates at an angle of roughly 56 degrees and hits the interface, located at $i = 20$. Because the effective index of refraction is $\sqrt{10}$, the critical angle for total internal reflection is approximately 18.5 degrees, so our incident angle is well beyond that. Figure 9.6 shows clearly the wave bouncing off the $i = 20$ boundary at approximately $j = 30$, then propagating back towards the left $i = 0$ boundary, and then continuing to bounce off different boundaries as it propagates towards $j = 100$.

9.6 Diffraction

The lattices we just simulated were all finite in extent. Let us turn our attention to waves with wavelength sufficiently large so that only a few wavelengths fit in the finite lattice. In this situation, we claim that the lattice acts as a diffraction slit. To give a definite example, consider a 100×80 lattice where we drive the left boundary as follows:

$$V_{1,j}(t) = 0.5 \sin(\beta j) \sin(2\pi\omega t). \quad (9.25)$$

Take the lattice parameters to be $L = 30\text{pH}$ and $C = 20\text{fF}$, and take the driving frequency to be $\omega = 60\text{GHz}$. Then the dispersion relation for the lattice tells us that waves propagating in the x -direction only have the following ratio of wavelength to

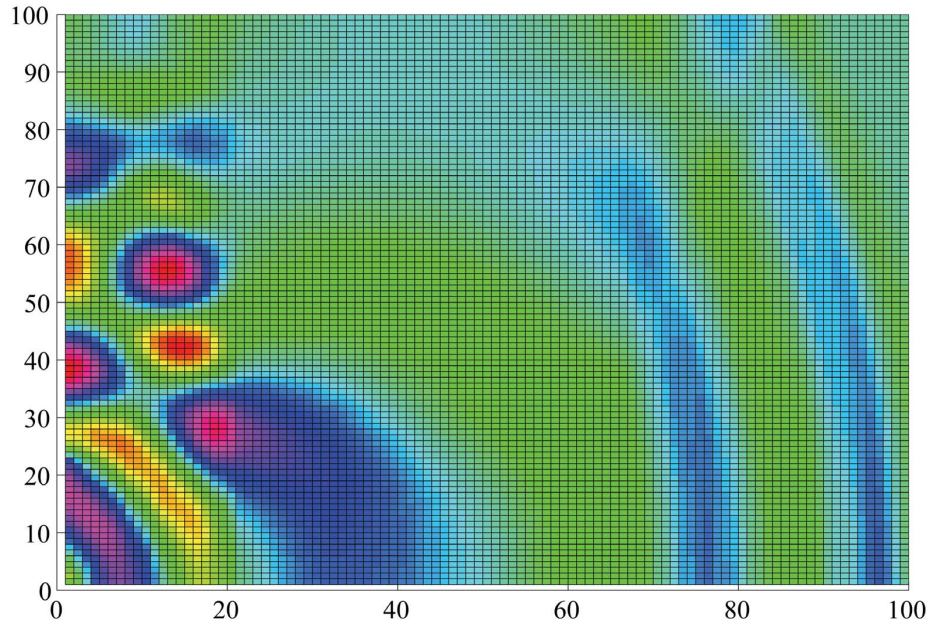


Figure 9.6: Total internal reflection. Colors correspond to level sets of the voltage $V_{ij}(t)$, at a particular instant of time $t > 0$. At $t = 0$, voltage forcing is switched on along the left boundary at nodes $1 \leq j \leq 20$; resulting waves propagate at a sharp angle towards the interface at $i = 20$, where they undergo total internal reflection and are sent back towards the boundary at $i = 0$. The waves bounce repeatedly off the effective boundaries at $i = 0$ and $i = 20$ as they propagate upwards towards $j = 100$. The lattice delay equals τ_1 for $i < 20$ and equals τ_2 for $i > 20$. In this simulation, unlike the previous two, we used a 100×100 lattice.

lattice spacing:

$$\frac{\lambda}{d} = \frac{\pi}{\sin^{-1}(\omega\sqrt{LC}/2)} \approx 21.4.$$

In other words, there are only about 4 or 5 wavelengths of the wave that can fit inside the 100×80 lattice. Moreover, if the forcing is of the form (9.25), then the wave will *not* propagate in the x -direction only. Parts of the wave will reflect off the top and bottom boundaries of the lattice in ostensibly complicated ways, and we would not expect the outgoing signal, $V_{100,j}(t)$, to look anything like the original input signal.

The problem of squeezing a long wave through a narrow opening is really just a thin-slit diffraction problem. We are about to consider the problem of two uniform 2-D

continuous media separated by a thin one-dimensional slit, where the slit is just a few wavelengths wide. Waves propagating from left to right through the slit are diffracted, and one can develop a Huygens-Fresnel type theory to predict the illumination far to the right of the aperture, due to a source to the left of the aperture. Roughly speaking, the illumination will be a phase-shifted Fourier transform of the source.

Going back to the 100×80 lattice with the above choice of parameters and the sinusoidal forcing (9.25), Figure 9.7 shows what we see from a numerical simulation of the 2-D LC lattice equations (9.2).

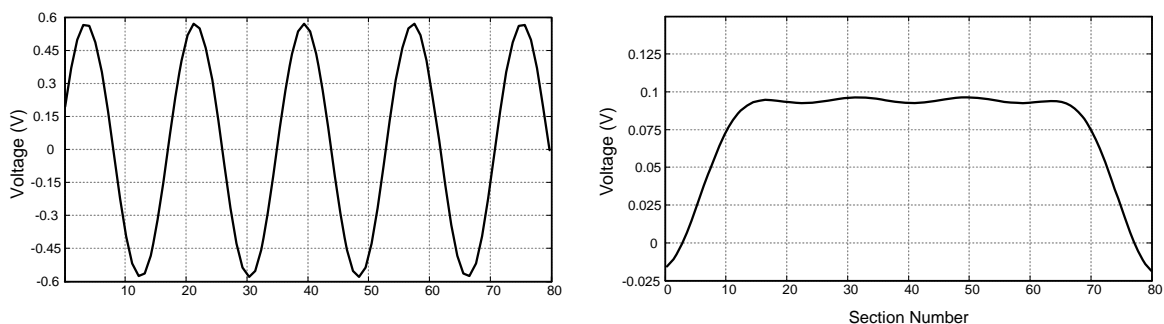


Figure 9.7: Simulation of a uniform 2-D LC lattice showing diffractive effects. The input signal is our choice of forcing function at the left boundary of the lattice, and the output signal is the signal at the right boundary of the lattice. The forcing is sinusoidal and given by (9.25), with $\omega = 60\text{GHz}$. Lattice inductances are $L = 30\text{pH}$ and lattice capacitances are $C = 20\text{fF}$.

The input is a sinusoidal function of the vertical coordinate j , and the output is clearly a different sort of function altogether. It turns out that the output is a phase-shifted or “blurry” version of the 1-D Fourier transform of the input. Eventually we will show simulations of a lattice with the same parameters, except inside a lens-shaped region in the lattice interior. The lens will cancel out the phase shift and bring the Fourier transform into focus.

Before discussing these simulations, let us take a moment to develop the elementary theory of scalar diffraction for 2-D waves. Though derivations of Kirchhoff and Rayleigh-Sommerfeld diffraction integrals have appeared in the literature before, we offer our own derivations here. This is in part because diffraction of 2-D waves has not attracted much attention in the literature, and the reader may not be fully aware

of the near- and far-field Hankel function asymptotics necessary to proceed in this case. Also, we believe our derivations, which follow the models set before by Born, Wolf, Goodman, and Stamnes[90; 91; 94], have their own advantages.

We begin by proving a Green's identity that forms the cornerstone of the 2-D wave theory of diffraction. Suppose we have a 2-D domain Ω , as in Figure 9.8.

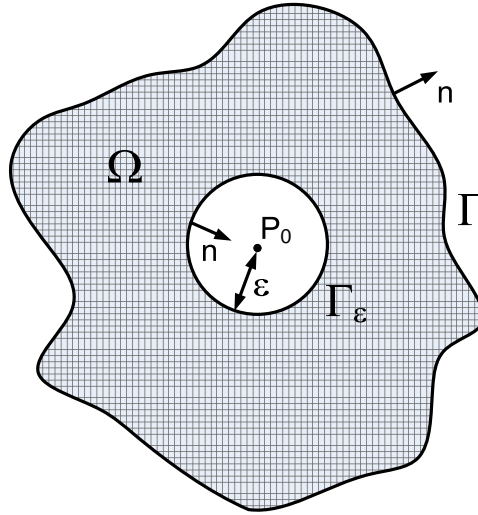


Figure 9.8: Setup for deriving Green's function representation of $U(P_0)$.

Assume that U is a scalar field that satisfies the Helmholtz equation

$$(\nabla^2 + k^2)U = 0$$

Given a point $P_0 \in \Omega$, we want to relate $U(P_0)$ to the values of U on the boundary of Ω , which we label as $\partial\Omega$. Use Green's Theorem (with U, G as solutions of the Helmholtz equation) which says

$$\iint_{\Omega} U \nabla^2 G - G \nabla^2 U \, ds = \iint_{\partial\Omega} U \frac{\partial G}{\partial n} - G \frac{\partial U}{\partial n} \, dl.$$

Because $\nabla^2 G = -k^2 G$ and $\nabla^2 U = -k^2 U$, the left-hand side of the above equation is zero, i.e.,

$$\iint_{\Omega} U(-k^2 G) - G(-k^2 U) \, ds = 0.$$

The boundary of Ω is the sum of two curves Γ and Γ_ϵ . The outer curve Γ is smooth but otherwise arbitrary. The inner curve Γ_ϵ is a circle of radius ϵ with center P_0 . Green's Theorem says

$$0 = \int_{\partial\Omega} U \frac{\partial G}{\partial n} - G \frac{\partial U}{\partial n} dl,$$

and because

$$\partial\Omega = \Gamma + \Gamma_\epsilon,$$

this implies

$$- \int_{\Gamma_\epsilon} U \frac{\partial G}{\partial n} - G \frac{\partial U}{\partial n} dl = \int_{\Gamma} U \frac{\partial G}{\partial n} - G \frac{\partial U}{\partial n} dl. \quad (9.26)$$

We evaluate the left integral, using the fact that on the curve Γ_ϵ , we have $dl = \epsilon d\theta$.

We set $G(r)$ equal to the radially symmetric solutions of the 2D Helmholtz equation.

These are solutions of the equation

$$\frac{1}{r} \frac{\partial}{\partial r} \left(r \frac{\partial G}{\partial r} \right) + k^2 G = 0,$$

which is in fact Bessel's equation. Solutions of Bessel's equation are Hankel functions, i.e.,

$$G(r) = H_0(kr) = J_0(kr) + iY_0(kr),$$

where J_0 is a Bessel function of the first kind and Y_0 is a Bessel function of the second kind. Then

$$\begin{aligned} - \int_{\Gamma_\epsilon} U \frac{\partial G}{\partial n} - G \frac{\partial U}{\partial n} dl &= -2\pi\epsilon \left(-kU(P_0 + \epsilon) \frac{\partial H_0}{\partial r}(k\epsilon) - H_0(k\epsilon) \frac{\partial U}{\partial n} \right) \\ &\approx -2\pi\epsilon \left(-kU(P_0) \left(-\frac{k\epsilon}{4} + i\frac{2}{\pi} \frac{1}{k\epsilon} \right) - \left(1 + i\frac{2}{\pi} \log \left(\frac{k\epsilon}{2} \right) \right) \right), \end{aligned} \quad (9.27)$$

where we have made the approximations

$$H_0(k\epsilon) \approx 1 + i\frac{2}{\pi} \log\left(\frac{k\epsilon}{2}\right)$$

$$\frac{\partial}{\partial r} H_0(k\epsilon) \approx -\frac{k\epsilon}{4} + i\frac{2}{\pi} \frac{1}{k\epsilon}.$$

These approximations are valid for $\epsilon \ll 1$, and the right- and left-hand sides of (9.27) have the same asymptotic behavior in the $\epsilon \rightarrow 0$ limit. However, the $\epsilon \rightarrow 0$ limit of the right-hand side of (9.27) is easily computable, leading to the result

$$\lim_{\epsilon \rightarrow 0} \left[- \int_{\Gamma_\epsilon} U \frac{\partial G}{\partial n} - G \frac{\partial U}{\partial n} dl \right] = 4iU(P_0).$$

Using this result in (9.26), we write

$$U(P_0) = \frac{1}{4i} \int_{\Gamma} U \frac{\partial G}{\partial n} - G \frac{\partial U}{\partial n} dl. \quad (9.28)$$

9.6.1 Kirchhoff

Consider diffraction in 2D from a screen with aperture Σ as in Figure 9.9.

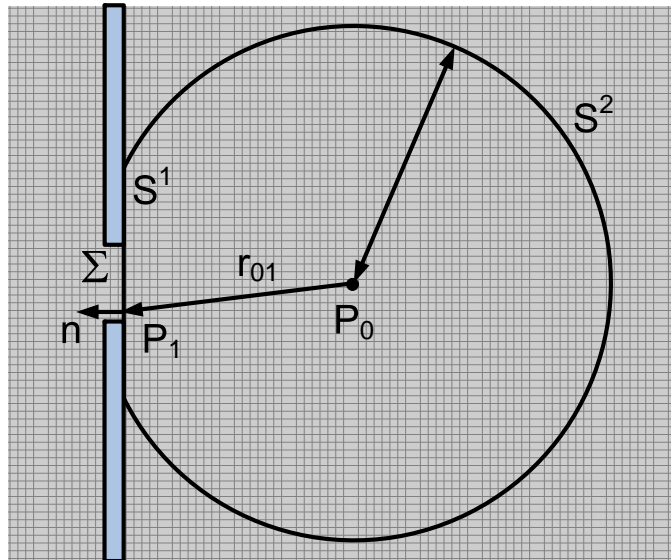


Figure 9.9: Setup for deriving Kirchhoff diffraction integral.

We now use the integral formula (9.28) to compute $U(P_0)$ with $\Gamma = S^1 + S^2$. We break the integral over Γ into two pieces, i.e.,

$$U(P_0) = \frac{1}{4i} \int_{S^1} U \frac{\partial G}{\partial n} - G \frac{\partial U}{\partial n} dl + \frac{1}{4i} \int_{S^2} U \frac{\partial G}{\partial n} - G \frac{\partial U}{\partial n} dl. \quad (9.29)$$

First let's do the integral over S^2 and show that it vanishes.

$$\begin{aligned} \int_{S^2} U \frac{\partial G}{\partial n} - G \frac{\partial U}{\partial n} dl &= \int_{S^2} U k \sqrt{\frac{2}{\pi k R}} i \exp[i(kr - \pi/4)] - \sqrt{\frac{2}{\pi k R}} \exp[i(kR - \pi/4)] \frac{\partial U}{\partial n} dl \\ &= \sqrt{\frac{2}{\pi k}} \int \sqrt{R} \left(ikU - \frac{\partial U}{\partial n} \right) \exp[i(kR - \pi/4)] d\theta, \end{aligned}$$

where we use the following approximations, valid for $R \gg 1$:

$$\begin{aligned} G(R) &= H_0(kR) \approx \sqrt{\frac{2}{\pi k R}} \exp[i(kR - \pi/4)] \\ \frac{\partial G}{\partial R} &= k \frac{\partial}{\partial r} H_0(kR) \approx k \sqrt{\frac{2}{\pi k R}} i \exp[i(kr - \pi/4)]. \end{aligned}$$

Therefore, we have the following condition: if, for all θ ,

$$\lim_{R \rightarrow \infty} \left[\sqrt{R} \left(ikU - \frac{\partial U}{\partial n} \right) \right] = 0,$$

then the S^2 integral vanishes. This condition is the 2D analogue of the Sommerfeld outgoing radiation condition. Assuming that the condition holds, the only contribution to the integral comes from S^1 , i.e., formula (9.29) reduces to

$$U(P_0) = \frac{1}{4i} \int_{S^1} U \frac{\partial G}{\partial n} - G \frac{\partial U}{\partial n} dl.$$

If we now make the Kirchhoff assumptions, then both U and $\partial U/\partial n$ are zero everywhere on S^1 *except* inside Σ . Take $P_1 \in \Sigma$ and define \mathbf{r}_{01} as the vector from P_0 to P_1 . Here and in what follows, we use r_{01} to denote the magnitude of the vector \mathbf{r}_{01} . Then

$$U(P_0) = \frac{1}{4i} \int_{\Sigma} U \frac{\partial}{\partial n} H_0(kr_{01}) - H_0(kr_{01}) \frac{\partial U}{\partial n} dl.$$

The Kirchhoff assumptions continue: assume that, inside Σ , both U and $\partial U/\partial n$ are the same as if there is no screen. That is to say, assume that $U(P_1)$ is the field due to a radially symmetric point source located at P_2 , where P_2 is a point to the left of the screen, as in Figure 9.10.

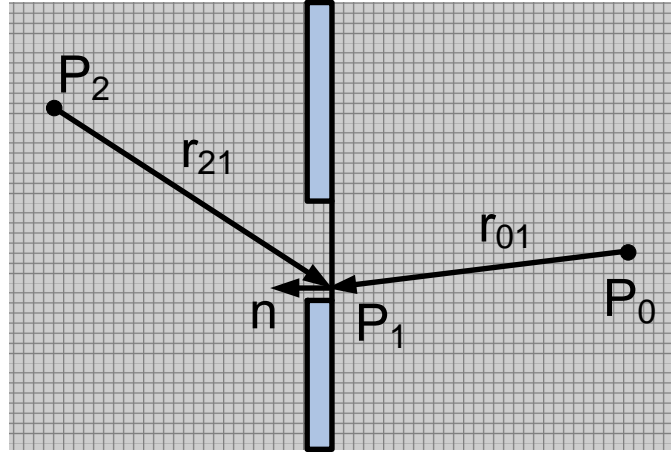


Figure 9.10: Illumination by point source in Kirchhoff diffraction integral.

Then, if \mathbf{r}_{21} is the vector joining P_1 to P_2 , we have

$$U(P_1) = AH_0(kr_{21}).$$

Using this in the above integral yields

$$\begin{aligned} U(P_0) &= \frac{1}{4i} \int_{\Sigma} AH_0(kr_{21}) \frac{\partial}{\partial n} H_0(kr_{01}) - H_0(kr_{01}) \frac{\partial}{\partial n} AH_0(kr_{21}) dl \\ &= \frac{A}{4i} \int_{\Sigma} H_0(kr_{21}) \frac{\partial}{\partial r} H_0(kr_{01}) \cos(\mathbf{n}, \mathbf{r}_{01}) - H_0(kr_{01}) \frac{\partial}{\partial r} H_0(kr_{21}) \cos(\mathbf{n}, \mathbf{r}_{21}) dl \\ &= \frac{Ak}{4i} \int_{\Sigma} -H_0(kr_{21}) H_1(kr_{01}) \cos(\mathbf{n}, \mathbf{r}_{01}) + H_0(kr_{01}) H_1(kr_{21}) \cos(\mathbf{n}, \mathbf{r}_{21}) dl. \end{aligned}$$

This is the Kirchhoff diffraction integral.

9.6.2 Rayleigh-Sommerfeld

There are inconsistencies in the Kirchhoff boundary conditions. If U and $\partial U/\partial n$ are *both* zero everywhere on a part of S^1 , and if U satisfies the Helmholtz equation in the domain contained by $\Gamma = S^1 + S^2$, then one can prove that U must be zero everywhere inside the curve Γ . To remedy this condition, we choose different Green's functions so that we have to enforce only *one* of the two conditions $U = 0$ or $\partial U/\partial n = 0$ on the part of S^1 that does include the aperture Σ .

In what follows, G_- will be the Green's function that corresponds to taking $\partial U/\partial n = 0$ on S^1 not including Σ . We could also evaluate the integral using G_+ , the Green's function that corresponds to taking $U = 0$ on S^1 not including Σ . Using G_- or G_+ to deriving, respectively, the first and second Rayleigh-Sommerfeld diffraction integrals. Here we pursue the calculation for G_- only.

The picture here is that P_0 is a point to the right of the screen, $P_1 \in \Sigma$ is a point inside the aperture, and \tilde{P}_0 is a point to the left of the screen that “mirrors” P_0 . This means that \mathbf{r}_{01} is the reflection of $\tilde{\mathbf{r}}_{01}$. The outward unit normal n points to the left from Σ , as in Figure 9.11.

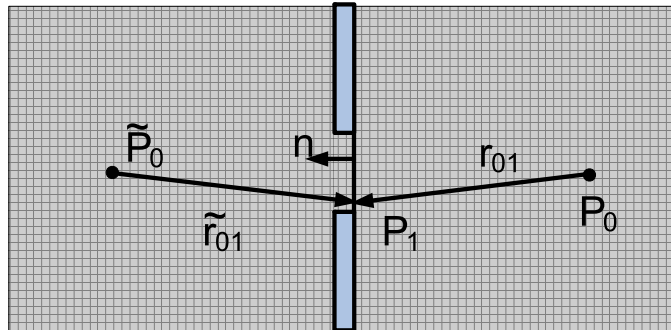


Figure 9.11: Setup for Sommerfeld Green's function

Using G_- in (9.28) gives

$$U_I(P_0) = \frac{1}{4i} \int_{\Sigma} U \frac{\partial G_-}{\partial n} dl.$$

Note that

$$\begin{aligned}\frac{\partial G_-}{\partial n} &= k \frac{\partial}{\partial r} H_0(kr_{01}) \cos(\mathbf{n}, \mathbf{r}_{01}) - k \frac{\partial}{\partial r} H_0(k\tilde{r}_{01}) \cos(\mathbf{n}, \tilde{\mathbf{r}}_{01}) \\ &= -kH_1(kr_{01}) \cos(\mathbf{n}, \mathbf{r}_{01}) + kH_1(k\tilde{r}_{01}) \cos(\mathbf{n}, \tilde{\mathbf{r}}_{01}).\end{aligned}$$

On Σ , we know that $\cos(\mathbf{n}, \tilde{\mathbf{r}}_{01}) = -\cos(\mathbf{n}, \mathbf{r}_{01})$ and that $r_{01} = \tilde{r}_{01}$. Therefore,

$$\frac{\partial G_-}{\partial n} = -2k \cos(\mathbf{n}, \mathbf{r}_{01}) H_1(kr_{01}).$$

This implies

$$U_I(P_0) = -\frac{k}{2i} \int_{\Sigma} U \cos(\mathbf{n}, \mathbf{r}_{01}) H_1(kr_{01}) dl. \quad (9.30)$$

This is the 2-D version of the first Rayleigh-Sommerfeld diffraction integral.

We could of course specialize this integral to the case where P_1 is illuminated by a radially symmetric point source located at P_2 , an arbitrary point to the left of the screen. This means that $U(P_1) = AH_0(kr_{21})$, which can be substituted into (9.30) to produce

$$U_I(P_0) = -\frac{kA}{2i} \int_{\Sigma} H_0(kr_{21}) H_1(kr_{01}) \cos(\mathbf{n}, \mathbf{r}_{01}) dl. \quad (9.31)$$

Let $\lambda = 2\pi/k$. For $r_{01} \gg \lambda$, $r_{21} \gg \lambda$, we obtain

$$\begin{aligned}U_I(P_0) &= \frac{-kA}{2i} \int_{\Sigma} \left(\sqrt{\frac{2}{\pi kr_{21}}} \exp[ikr_{21} - i\pi/4] \right) \\ &\quad \times \left[\sqrt{\frac{2}{\pi kr_{01}}} \exp[ikr_{01} - i\pi/4] \cdot (-i) \right] \cos(\mathbf{n}, \mathbf{r}_{01}) dl,\end{aligned}$$

where the term in parentheses is the large r approximation of $H_0(kr_{21})$ and the term in square brackets is the large r approximation of $H_1(kr_{01})$. Using these approximations, we have

$$U_I(P_0) = \frac{A}{\pi} \int_{\Sigma} \frac{1}{\sqrt{r_{21}r_{01}}} \exp[ik(r_{01} + r_{21})] (-i) \cos(\mathbf{n}, \mathbf{r}_{01}) dl.$$

9.6.3 Huygens-Fresnel

Our goal here is to determine the illumination onto a plane screen located several wavelengths away from the aperture. For diffraction problems in two spatial dimensions, we do not believe this calculation has appeared previously in the literature. The picture is given in Figure 9.12.

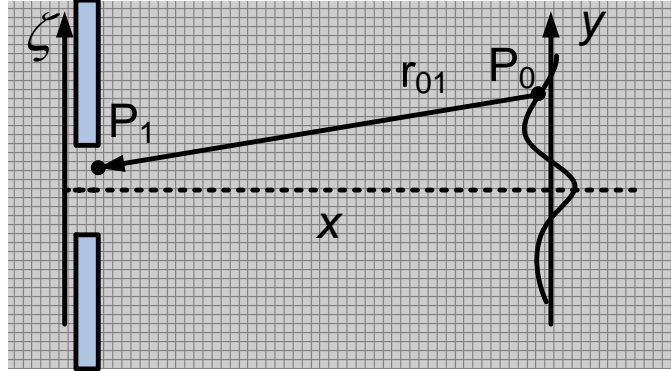


Figure 9.12: Huygens-Fresnel picture showing illumination on a line several wavelengths away from the thin slit diffraction aperture.

We start with the Rayleigh-Sommerfeld diffraction integral (9.30), which we repeat here:

$$U_I(P_0) = \frac{-k}{2i} \int_{\Sigma} U \cos(\mathbf{n}, \mathbf{r}_{01}) H_1(kr_{01}) dl.$$

Inside the aperture Σ , we have $\cos \theta = x/r_{01}$, which gives

$$U_I(y) = -\frac{kx}{2i} \int_{\Sigma} U(\xi) \frac{H_1(kr_{01})}{r_{01}} d\xi.$$

We use $r_{01}^2 = x^2 + (y - \xi)^2$ and approximate

$$r_{01} = x \sqrt{1 + \left(\frac{y - \xi}{x}\right)^2} \approx x \left(1 + \frac{1}{2} \left(\frac{y - \xi}{x}\right)^2\right) = x + \frac{1}{2} \frac{(y - \xi)^2}{x}.$$

The same approximation strategy gives

$$\frac{1}{r_{01}} \approx \frac{1}{x} \frac{1}{1 + (y - \xi)^2/(2x^2)} \approx \frac{1}{x} \left(1 - \frac{1}{2} \frac{(y - \xi)^2}{x^2}\right) = \frac{1}{x} - \frac{1}{2} \frac{(y - \xi)^2}{x^3}.$$

The difference between the approximations of r_{01} and r_{01}^{-1} is that the $O(y - \xi)^2$ term appears in r_{01}^{-1} with an extra factor of x^{-2} . Since x is assumed large compared with the wavelength, we keep the $O(y - \xi)^2$ term only when r_{01} appears in the numerator, and drop it whenever r_{01} appears in the denominator. This gives

$$U_I(y) = \frac{-k}{2i} \int_{\Sigma} U(\xi) H_1 \left[kx \left(1 + \left(\frac{y - \xi}{x} \right)^2 \right) \right] d\xi.$$

Now we use the far-field asymptotics of the Hankel function to approximate

$$\begin{aligned} H_1 \left[kx \left(1 + \left(\frac{y - \xi}{x} \right)^2 \right) \right] &\approx \sqrt{\frac{2}{\pi kx \left(1 + \left(\frac{y - \xi}{x} \right)^2 \right)}} \exp \left[i \left(kx + \frac{k}{x} (y - \xi)^2 - \pi/4 \right) \right] \\ &\approx \sqrt{\frac{2}{\pi}} \frac{e^{ikx}}{\sqrt{xk}} \exp \left[\frac{ik}{x} (y - \xi)^2 - i\pi/4 \right]. \end{aligned}$$

Inserting this approximation into the integral we have

$$\begin{aligned} U_I(y) &\approx -\frac{k}{2i} \sqrt{\frac{2}{\pi}} \frac{e^{ikx} e^{-i\pi/4}}{\sqrt{kx}} \int_{\Sigma} U(\xi) \exp \left[\frac{ik}{x} (y - \xi)^2 \right] d\xi \\ &= -\frac{e^{i\pi/4} \sqrt{2}}{2i\sqrt{\pi}} \sqrt{k} \frac{e^{ikx}}{\sqrt{x}} \int_{\Sigma} U(\xi) \exp \left[\frac{ik}{x} (y^2 - 2y\xi + \xi^2) \right] d\xi \\ &= C \sqrt{k} \frac{e^{ikx}}{\sqrt{x}} e^{\frac{ik}{x} y^2} \int_{-\infty}^{+\infty} \left\{ U(\xi) e^{\frac{ik}{x} \xi^2} \right\} e^{-\left(\frac{2ik}{x}\right) y \xi} d\xi, \end{aligned} \quad (9.32)$$

where $U(\xi) = 0$ when $\xi \notin \Sigma$, and where the constant C is given by

$$C = -\frac{e^{i\pi/4} \sqrt{2}}{2i\sqrt{\pi}}.$$

Note that this last integral (9.32) is the Fourier integral with phase shift. If we can design a lens that cancels out the phase shift $e^{\frac{ik}{x} \xi^2}$, then we have designed a 2-D LC lattice that takes the spatial Fourier transform of an input signal.

9.7 Applications

9.7.1 Comments on the Implementation

It is feasible to make this lattice on a semiconductor substrate. Here we assume a Silicon substrate that is more popular in today's Silicon technology. We use pieces of metal as our inductor and metal-to-metal capacitance as the capacitor.

From the lattice dispersion relation (9.4), we know that in order to maximize the lattice cut-off frequency, we need to minimize the values of inductors and capacitors in each section. However, we cannot arbitrarily shrink the capacitances of each section, because at some point, parasitic capacitance becomes comparable with our lumped capacitance. In today's typical Silicon processes, we can have inductances as low as 30pH and capacitances as small as 5fF before the parasitic factors become an issue. The quality factor for these elements is around 20, giving us a lattice cut-off frequency of around 300GHz.

One important issue is ohmic loss of the Silicon substrate. To address this problem, we need to use a ground plane beneath our inductors to shield the Silicon substrate. By adding this layer, we could achieve higher quality factors in our inductors. To find the exact value of inductance and capacitance as well as loss in each section, we use an E/M simulator such as Ansoft HFSS[72].

Another issue that has an effect on the performance of the structure is magnetic coupling of the inductors. Adjacent inductors induce current in each other; to model this accurately requires additional terms in our circuit model (9.2). Fortunately, with typical values of inductors and capacitors, this mutual inductance is not that large: a careful E/M simulation shows that the coupling coefficient of adjacent inductors is less than 0.1. In our numerical analysis, we take this effect into account, but because of complexity we neglected this effect in our mathematical analysis.

Using the exact circuit models, we have simulated this structure and are in the process of fabricating the Fourier transform circuit in a SiGe BiCMOS process.

Figure 9.13 clearly shows the architecture of the circuit, with a lens-shaped region in the interior designed to cancel out the phase shift in the Huygens-Fresnel integral

(9.32).

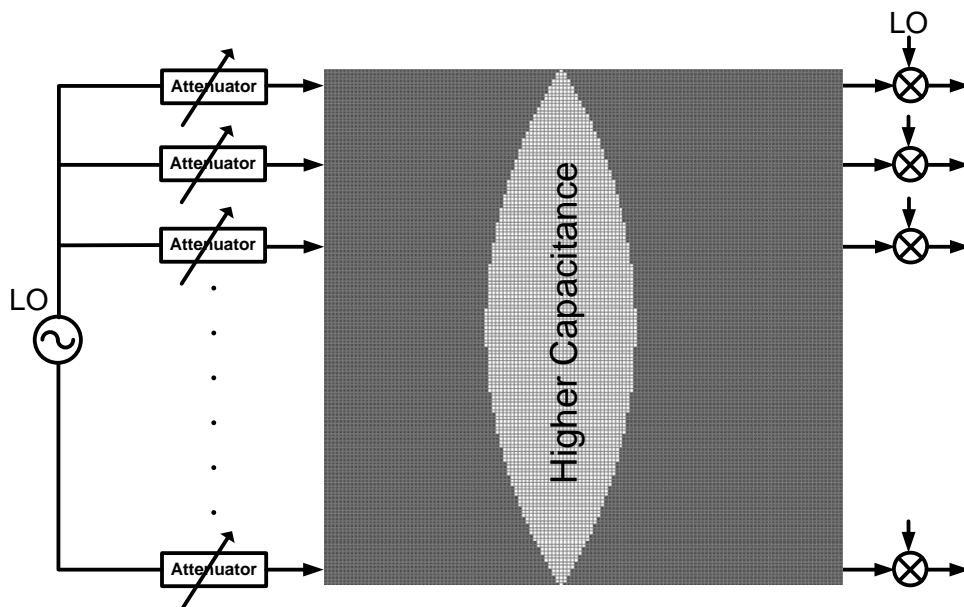


Figure 9.13: Architecture

9.7.2 Fourier Transform

Direct numerical simulations show quite clearly the Fourier transform capabilities of the 2-D LC lattice. By this we mean that if the forcing of the lattice's left boundary is given by

$$V_{1,j}(t) = p_j \sin(2\pi\omega t), \quad (9.33)$$

then the signal at the right boundary will consist of an approximate, discrete Fourier transform of the spatial part \mathbf{p} of the input signal. In what follows, all reported numerical results arise from solving Kirchoff's laws (9.2) for 80×100 lattices, subject to the boundary conditions described in Section II-D.

Sinusoidal inputs. Figure 9.14 shows the Fourier transform of two sinusoids, with two different spatial wavelengths.

The lattice parameters are nearly the same as before for Figure 9.7: namely, outside the lens-shaped region shown in Figure 9.13, we take $L = 30\text{pH}$, $C = 20\text{fF}$,

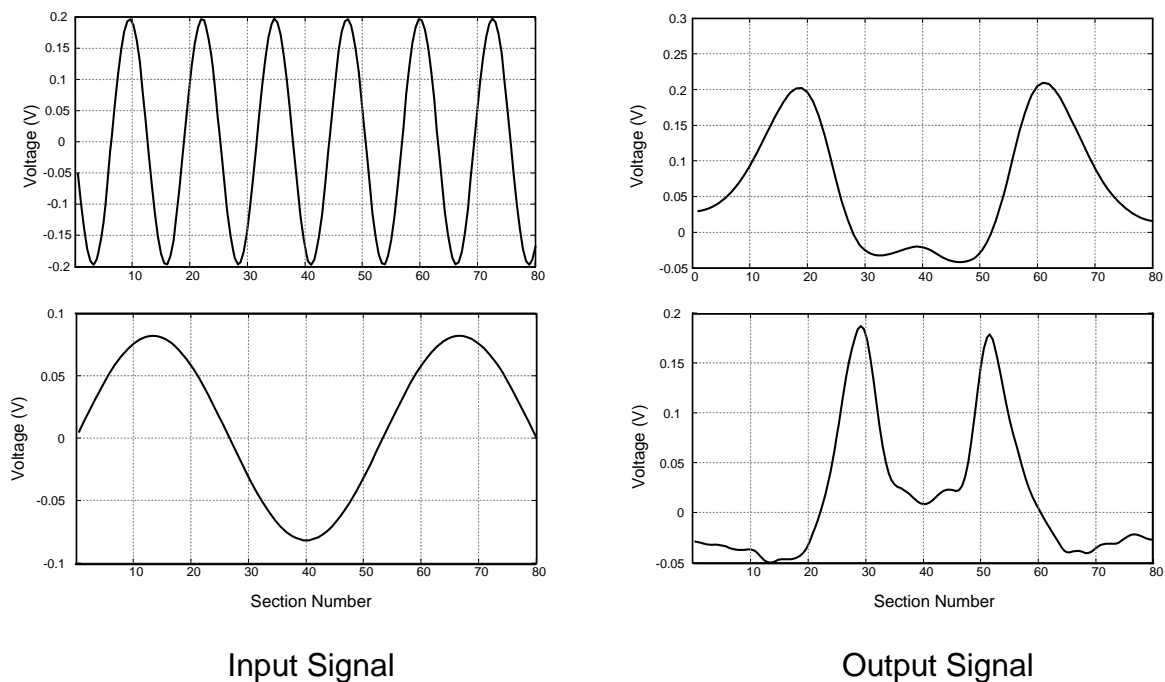


Figure 9.14: Results for two different numerical simulations of the 2-D LC lattice showing how diffraction and lensing effects combine to effectively take the spatial 1-D Fourier transform of the input signal. The plots on the left (input signals) correspond to two different choices of p_j in expression (9.33), with $\omega = 60\text{GHz}$. Lattice parameters are $L = 30\text{pH}$ and $C = 20\text{fF}$, except in a lens-shaped region in the center of the lattice where L is unchanged but $C = 60\text{fF}$. For each input signal, such a lattice was simulated, and the plots on the right show $V_{100,j}(t)$ as a function of vertical section number j , for a particular instant of time $t > 0$.

and $\omega = 60\text{GHz}$. Inside the lens-shaped region, we leave L unchanged but take $C = 60\text{fF}$. The lattice has 80 nodes in the vertical direction and 100 nodes in the horizontal direction. We force the left boundary with a sinusoidal forcing function of the form (9.25), and examine the output at the right boundary.

To ensure that the simulations are realistic, we add two effects not present in our mathematical analysis above. Namely, we add a mutual inductance term that takes into account coupling of adjacent inductors. As mentioned above, the coupling coefficient for this term is very small compared with unity (0.1), and the effect is not large. Furthermore, we assume each section as a resistance of 0.1Ω , and that all inductors and capacitors vary randomly by about 5% from the values reported above.

The output of the circuit shows clearly two peaks, as expected. Furthermore,

the sinusoid with smaller wavelength (and therefore higher wave number) yields two peaks that are more widely separated than those generated by the sinusoid with larger wavelength (and therefore smaller wave number). Because the aperture of the lens is comparable with the wavelength of the input signal, diffractive effects are quite important. The output is *not* simply a focused version of the input, but a focused and diffracted version of the input. Comparing Figure 9.7 and Figure 9.14, it is now clear that the lens brings into focus the blurry Fourier transform that results from diffraction alone.

Finally, Figure 9.14 clearly shows the DC value of the input. The first waveform has a lower average value compared to the second one and we can clearly see this difference in our output waveform.

Step input. Next we consider precisely the same lattice, changing the boundary forcing to be equal to a step function, namely,

$$V_{1,j}(t) = 0.15 \sin(2\pi\omega t). \quad (9.34)$$

The output signal is shown in Figure 9.15.

The Fourier transform of the step input is a sinc function, shown by the green curve. Our mathematical analysis predicts that the output should be given by the blue curve, while the numerical simulation itself yielded the black curve.

The three curves are qualitatively the same except in the tails, where there is some discernible disagreement. In the tails, one finds that our analysis is closer to the numerical simulation than the true Fourier transform. The error in the tails is due to two factors: (1) due to boundary effects, the finite lattice is not exactly the same as a thin slit diffraction problem, though it features qualitatively identical physics, and (2) the lens-shaped region in the middle of the 2-D LC lattice is not quite a “thin lens,” meaning that the paraxial approximation is not quite valid. Some of the phase shift from the original Huygens-Fresnel diffraction integral is not quite canceled out in the tails.

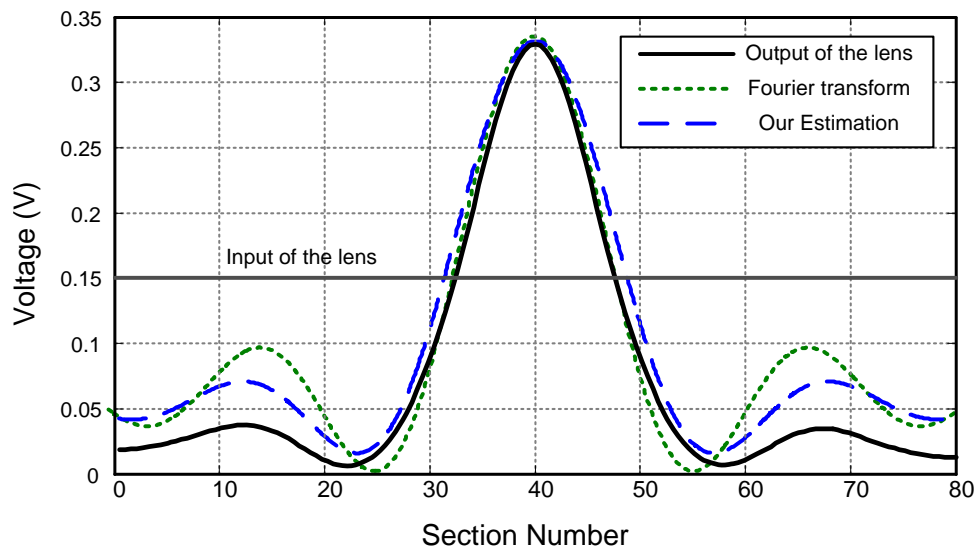


Figure 9.15: Numerical simulation of the 2-D LC lattice (in black) as compared with our analytical prediction (in blue) and the true Fourier transform (in green) of the input given by (9.34), with $\omega = 60\text{GHz}$. Lattice parameters are unchanged from Figure 9.14. The black curve shows the numerically computed values of $V_{100,j}(t)$ as a function of vertical section number j , for a particular instant of time $t > 0$.

Sinc input. Finally we consider the same lattice again but with input equal to a sinc function:

$$V_{1,j}(t) = 0.3 \text{sinc}(\beta j) \sin(2\pi\omega t). \quad (9.35)$$

The input signal is shown in Figure 9.16, and the output signal is shown in Figure 9.17. The output is roughly symmetric, and roughly constant between elements 28 and 52. The true discrete Fourier transform, limited to a particular band of wave numbers, would be perfectly symmetric and have much steeper rise and fall sections than the curve shown in Figure 9.17. However, given that we included just over two full cycles of the sinc function as input, the output is quite reasonable.

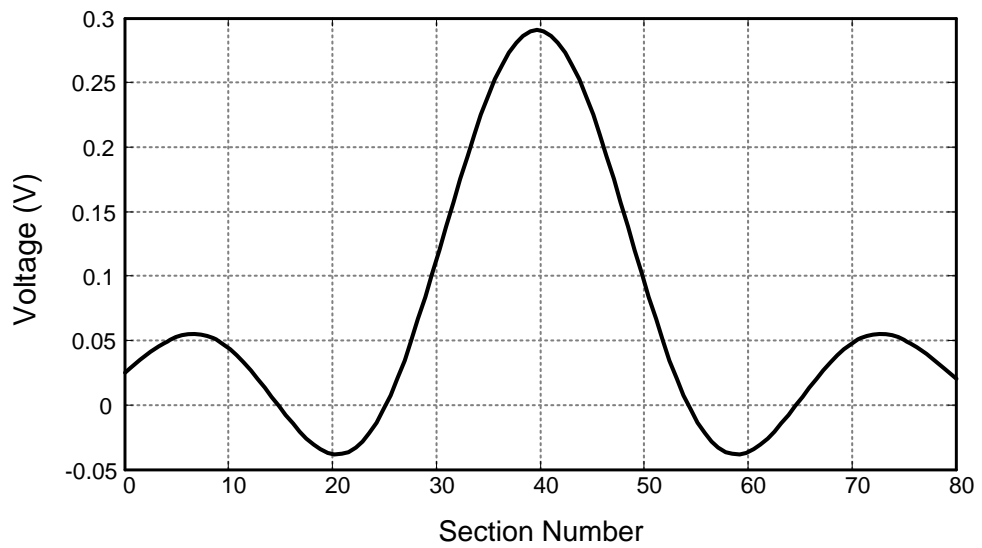


Figure 9.16: Sinc input for the 2-D LC lattice, corresponding to Equation (9.35) with $\omega = 60\text{GHz}$. The input $V_{1,j}(t)$ is plotted versus vertical section number j at a fixed instant of time t .

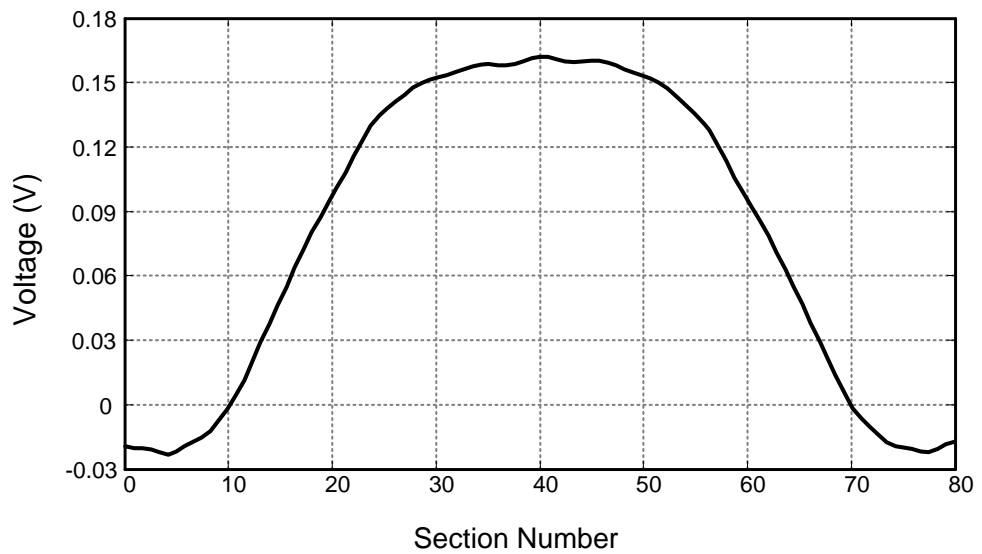


Figure 9.17: Simulated output $V_{100,j}(t)$ at a fixed instant of time $t > 0$, plotted versus vertical section number j . The input that generated this output is given by Equation (9.35) and Figure 9.16. Lattice parameters are unchanged from Figure 9.14.

Chapter 10

Conclusion

Broadly speaking, the main innovation in our work is to design circuits based on the mathematical theory of wave propagation, inspired by commonly used structures in electromagnetics, and more specifically optics. Let us examine how this process works. Given a discrete line/lattice, we write general continuum models that apply to a large range of circuits. These continuum models consist of nonlinear, dispersive differential equations with wave solutions. We subject these models to both mathematical analysis and numerical simulation. In doing so, we obtain relationships between the parameters (i.e. the local values of inductance/capacitance) of the line/lattice and the solutions of the differential equations. Then, if we want the solutions to behave in a particular way (e.g. focusing all the energy from the left boundary into a single pulse at the right boundary), we select the parameters accordingly. This procedure enables us to exploit the vast body of mathematical knowledge concerning nonlinear wave equations, and it opens a door to new techniques for circuit designers.

In this work we demonstrated:

- The narrowest reported pulse on silicon (2.5ps),
- The first in-silicon transmission line system capable of sharpening both rising and falling edges of NRZ data by increasing the bandwidth,
- For a single integrated-circuit silicon-based amplifier, the highest achieved center frequency of operation (85GHz) and the highest achieved power output (120mW) at this frequency,

- Ultra-fast computation systems such as a sub-nanosecond Fourier and Hankel transformers in silicon.

Also we showed how the same approach can be applied to realize other structures, leading to a new design discipline we like to call "*Optotronics*".

Bibliography

- [1] G. E. Moore, “Cramming more components onto integrated circuits,” *Electronics*, vol. 38, no. 8, pp. 114117, Apr. 1965.
- [2] www.census.gov/Press-Release/www/releases/archives/miscellaneous/003136.html.
- [3] M. J. Lighthill, and G. B. Whitham, “On Kinematic Waves .2. A Theory of Traffic Flow on Long Crowded Roads,” *Proc. Roy. Soc. A*, vol. 229, pp. 317-345, 1955.
- [4] A. C. Scott, *Active and Nonlinear Wave Propagation in Electronics*, Wiley, New York, NY, 1970.
- [5] C. A. Coulson, *Waves*, Oliver and Boyd, New York, 1947.
- [6] G. B. Whitham, *Lectures on Wave Propagation*, Springer-Verlag, New York, 1979.
- [7] I. Tolstoy, 1923- *Wave Propagation* , McGraw-Hill, New York, 1973.
- [8] E. Infeld and G. Rowlands, *Nonlinear Waves, Solitons and Chaos*, Cambridge University Press, Cambridge, second edition, 2000.
- [9] Z. Zhu, Q. S. Wu, R. Jiang, and T. Wu, “Numerical Study on Traffic Flow with Single Parameter State Equation,” *Journal of Transportation Engineering*, pp. 167-172, March/April 2002.
- [10] G. M. Coclite, M. Garavello, B. Piccoli, “Traffic Flow on a Road Network,” *SIAM Journal on Mathematical Analysis*, vol. 36(6), pp. 1862-1886, 2005.

- [11] R. Jiang, Q. S. Wu, “Cellular Automata Models for Synchronized Traffic Flow,” *Journal of Physics A*, vol. 36 (2), pp.381-390, JAN 2003.
- [12] A. Kotsialos, M. Papageorgiou, C. Diakaki, *et al.*, “Traffic Flow Modeling of Large-Scale Motorway Networks Using the Macroscopic Modeling Tool METANET,” *IEEE Transactions on intelligent Transportation Systems*, vol. 3(4), pp. 282-292, DEC 2002.
- [13] D. K. Lynch, “Tidal bores,” *Scientific American*, vol. 247, pp. 132-143, 1982.
- [14] <http://en.wikipedia.org/wiki/Tidalbore>.
- [15] J. W. Allen, W. Shockley, G. L. Pearson, “Gunn Domain Dynamics,” *Journal of Applied Physics*, vol. 37 (8), 3191, 1966.
- [16] P. N. Butcher, G. J. Rowlands, “Stability of Gunn Domains,” *Physics Letters A*, vol. 26 (6), 226, 1968.
- [17] D’Arcy Thompson, *On Growth and Form*, Cambridge, (abridged) 1961.
- [18] A. M. Turing, “The Chemical Basis of Morphogenesis,” *Philosophical Transactions of the Royal Society of London*, vol. B, pp. 37-72, 1952.
- [19] P. G. Drazin, and R. S. Johnson, *Solitons*, Cambridge University Press, Cambridge, 1989.
- [20] J. S. Russell, “Report on Waves,” *British Association for the Advancement of Science*, pp. 311-90, York, Sept. 1844.
- [21] E. Fermi, J. Pasta, S. Ulam, *Studies of Nonlinear Problems*, Document LA-1940, May 1955.
- [22] N. J. Zabusky, M. D. Kruskal, “Interaction of Solitons in a Collisionless Plasma and Recurrence of Initial States,” *Physical Review Letters*, vol. 15, pp. 240-243, 1965.
- [23] A. S. Davydov, *Soliton in Biology*, Elsevier Science Publisher B. V., 1986.

- [24] A. Hasegawa and F. Tappert, "Transmission of stationary nonlinear optical pulses in dispersive dielectric fibers," *Applied Physics Letters* vol. 23, Issue 3, pp. 142-144, 1973.
- [25] P. R. Alfano and S. L. Shapiro, "Observation of Self-Phase Modulation and Small-Scale Filaments in Crystals and Glasses," *Physical Review Letters*, vol. 24, Issue 11, pp. 592-6, 1970.
- [26] C. G. B. Garrett and D. E. McCumber, "Propagation of a Gaussian Light Pulse Through an Anomalous Dispersion Medium," *Physical Review A*, vol. 1, Issue 2, pp. 305-320, 1970.
- [27] Newton, "*Principia*," Book II, 1686.
- [28] P. Debye, *Vorträge über die kinetische der Materie und der Elektrizität*, Berlin: Teubner, 1914.
- [29] R. E. Peierls, "*Quantum Theory of Solids*," Wiley, 1961.
- [30] D. J. Korteweg and F. de Vries, "On the Change of Form of Long Waves Advancing in a Rectangular Canal, and on a New Type of Long Stationary Waves," *Philosophical Magazine*, vol. 39, pp. 422-443, 1895.
- [31] C. S. Gardner, C. S. Greene, M. D. Kruskal, and R. M. Miura, "Method for Solving the Korteweg-de Vries Equation," *Physical Review Letters*, vol. 19, pp. 1095-1097, 1967.
- [32] R. M. Miura, C. S. Gardner, and M. D. Kruskal, "Korteweg-de Vries Equation and Generalizations. II. Existence of Conservation Laws and Constants of Motion," *J. Math. Phys.*, vol. 9, pp. 1204-1209, 1968.
- [33] L. Brillouin, *Wave Propagation in Periodic Structures. Electric Filters and Crystal Lattices*, International Series in Pure and Applied Physics, McGraw-Hill, New York, NY, 1946.

- [34] R. A. Scholtz, "Signal Selection for the Indoor Wireless Impulse Radio Channel," *Proceedings IEEE VTC conference*, May 1997.
- [35] E. kameda, T. Matsuda, Y. Emura, and T. Ohzone, "Study of the Current-Voltage Characteristics in MOS Capacitors with Si-Implanted Gate Oxide," *Solid-State Electronics*, vol. 43, no. 3, pp. 555-63, 1999.
- [36] S. Matsumoto, *et al.*, "Validity of Mobility Universality for Scaled Metal-Oxide-Semiconductor Field-Effect Transistors Down to 100 nm Gate Length," *Journal of Applied Physics*, vol. 92, no. 9, pp. 5228-32, 2002.
- [37] L. Larcher, P. Pavan, F. Pellizzer, G. Ghidini, "A New Model of Gate Capacitance as a Simple Tool to Extract MOS Parameters," *IEEE Transactions on Electron Devices*, vol. 48, no. 5, pp. 935-45, 2001.
- [38] R. Landauer, "Parametric Amplification Along Nonlinear Transmission Lines," *Journal of Applied Physics*, vol. 31, pp. 479-484, 1960.
- [39] R. Landauer, "Shock Waves in Nonlinear Transmission Lines and Their Effect on Parametric Amplification," *IBM Journal of Research and Development*, vol. 4, pp. 391-401, 1960.
- [40] R. Hirota and K. Suzuki, "Studies on Lattice Solitons by Using Electrical Networks," *Journal of Physical Society of Japan*, vol 28, 1366, 1970.
- [41] V. Nejoh, "Cusp Solitons, Shock-Waves and Envelope Solitons in a New Non-linear Transmission-Line ," *Journal of Physics A*, vol. 20, pp. 1733-1741, 1987.
- [42] P. Pantano, "Inhomogeneous Dispersive and Dissipative Nonlinear Transmission Lines and Solitons," *Lettere Al Nuovo Cimento*, vol. 36, pp. 209-214, 1982.
- [43] H. Ikezi, S. S. Wojtowicz, R. E. Waltz, and D. R. Baker, "Temporal Contraction of Solitons in a Nonuniform Transmission-Line," *Journal of Applied Physics*, vol. 64, 6836, 1988.

- [44] M. J. W. Rodwell, M. Kamegawa, R. Yu, M. Case, E. Carman, and K. Giboney, "GaAs Nonlinear Transmission Lines for Picosecond Pulse Generation and Millimeter-Wave Sampling," *IEEE Transactions on Microwave Theory and Techniques*, vol. 39, no. 7, pp. 1194-1204, July 1991.
- [45] K. Muroya and S. Watanabe, "Experiment on Soliton in Inhomogeneous Electric-Circuit .1. Dissipative Case," *Journal of Physical Society of Japan*, vol. 50, pp. 3159-3165, 1981.
- [46] S. Watanabe and K. Muroya, "Experiment on Soliton in Inhomogeneous Electric-Circuit .2. Dissipative-Free Case," *Journal of Physical Society of Japan*, vol. 50, pp. 3166-3172, 1981.
- [47] M. Tan, C.-Y. Su, and W. J. Anklam, "7X Electrical Pulse-Compression on an Inhomogeneous Nonlinear Transmission-Line," *Electronics Letters*, vol. 24, pp. 213-215, 1988.
- [48] M. J. W. Rodwell, *et al.*, "Active and Nonlinear-Wave Propagation Devices in Ultrafast Electronics and Optoelectronics," *Proceedings of the IEEE*, vol. 82, pp. 1037-1059, 1994.
- [49] G. J. Ballantyne, P. T. Gough, and D. P. Taylor, "A Baseband Soliton Oscillator," *Chaos, Solitons & Fractals*, vol. 5, No. 6, pp. 1013-1029, 1995.
- [50] J. N. Dinkel, C. Setzer, S. Rawal, and K. E. Lonngren, "Soliton Propagation and Interaction on a Two-Dimensional Nonlinear Transmission Line," *Chaos, Solitons, and Fractals*, vol. 12, pp. 91-96, 2001.
- [51] B. B. Kadomtsev, and V. I. Petviashvili, "On the Stability of Solitary Waves in Weakly Dispersive Media," *Sov. Phys. Dokl.*, vol. 15, pp. 539-541, 1970.
- [52] H. Kaufman, "Bibliography of Nonuniform Transmission Lines," *IRE Transactions—Antennas and Propagation*, vol. 3, pp. 218-220, 1955.

- [53] I. Aoki, S. Kee, D. Rutledge, and A. Hajimiri, "Fully Integrated CMOS Power Amplifier Design Using the Distributed Active-Transformer Architecture," *IEEE Journal of Solid-State Circuits*, vol. 37, pp. 371-383, 2002.
- [54] A. Komijani and A. Hajimiri, "A 24GHz, +14.5dBm Fully-Integrated Power Amplifier in 0.18um CMOS," *Proceedings of IEEE Custom Integrated Circuits Conference*, pp. 561-564, Oct. 2004.
- [55] E. Afshari and A. Hajimiri, "Nonlinear Transmission Line for Signal Shaping on Silicon," *IEEE Journal of Solid-State Circuits*, vol. 40, pp. 744-752, 2005.
- [56] E. Afshari and A. Hajimiri, "Nonlinear Transmission Line for Signal Shaping on Silicon," *Proceedings of IEEE Custom Integrated Circuits Conference*, pp. 91-95, 2003.
- [57] W.-S. Duan, "Nonlinear Waves Propagating in the Electrical Transmission Line," *Europhysics Letters*, vol. 66, pp. 192-197, 2004.
- [58] S. Klainerman and A. Majda, "Formation of Singularities for Wave-Equations Including the Non-Linear Vibrating String," *Communications on Pure and Applied Mathematics*, vol. 33, pp. 241-263, 1980.
- [59] F. John, *Nonlinear wave equations, formation of singularities*, volume 2 of *University Lecture Series*, American Mathematical Society, Providence, RI, 1990.
- [60] J. L. Bona and R. Smith, "Initial-Value Problem for Korteweg-Devries Equation," *Phil. Trans. Roy. Soc. London Ser. A.*, vol. 278, pp. 555-601, 1975.
- [61] P. D. Lax and C. D. Levermore, "The Small Dispersion Limit of the Korteweg-Devries Equation .1.," *Communications on Pure and Applied Mathematics*, vol. 36, pp. 253-290, 1983.
- [62] A. S. Fokas and M. J. Ablowitz, "Forced Nonlinear Evolution-Equations and the Inverse Scattering Transform," *Studies in Applied Mathematics*, vol. 80, pp. 253-272, 1989.

- [63] R. Camassa and T. Y. Wu, “The Korteweg-Devries Model with Boundary Forcing,” *Wave Motion*, vol. 11, pp. 495-506, 1989.
- [64] D. J. Kaup and A. C. Newell, “Solitons as Particles, Oscillators, and in Slowly Changing Media- Singular Perturbation-Theory,” *Proc. Roc. Soc. London, Ser. A.*, vol. 361, pp. 413-446, 1978.
- [65] R. H. J. and S. R. Pudjaprasetya, “Generation of Secondary Solitary Waves in the Variable-Coefficient Korteweg-de Vries Equation,” *Studies in Applied Mathematics*, vol. 112, pp. 271-279, 2004.
- [66] *SONNET Software*, Sonnet Technologies Inc., 2004, High frequency electromagnetic software. Available online at <http://www.sonnetusa.com>.
- [67] *Advanced Design System User Guide*, Agilent Technologies Inc., 2002.
- [68] E. Afshari, H. S. Bhat, A. Hajimiri, and J. E. Marsden, “Extremely Wideband Signal Shaping Using One-and Two-Dimensional Nonuniform Nonlinear Transmission Lines,” *Journal of Applied Physics*, vol. 99, 2006.
- [69] E. Afshari, H. S. Bhat, X. Li, and A. Hajimiri, “Electrical Funnel: A Broadband Signal Combining Method,” *Proceedings of IEEE International Solid-State Circuits Conference*, pp. 206-208, 2006.
- [70] G. Friesecke, R. L. Pego, “Solitary Waves on FPU Lattices: I. Qualitative Properties, Renormalization and Continuum Limit,” *Nonlinearity*, vol. 12, pp. 1601-1627, 1999.
- [71] K. Maruno and G. Biondini, “Resonance and Web Structure in Discrete Soliton Systems: the Two-Dimensional Toda Lattice and its Fully Discrete and Ultra-Discrete Analogues,” *Journal of Physics A*, vol. 37, pp. 11819-11839, 2004.
- [72] *High-Frequency Structure Simulator*, Ansoft, 2006, High frequency electromagnetic simulator. Available online at <http://www.ansoft.com/products/hf/hfss/>.

- [73] M. G. Case, *Nonlinear Transmission lines for Picosecond Pulse, Impulse and Millimeter-Wave Harmonic Generation*, Ph.D. dissertation, University of California Santa Barbara, July 1993.
- [74] E. R. Benton and G. W. Platzman, "A Table of Solutions of the of the One-Dimensional Burgers Equation," *Quart. Appl. Math.*, pp. 195-212, Jul. 1972.
- [75] *MathWorks.*, Matlab User Guide, Available online at <http://www.mathworks.com/>
- [76] U. R. Pfeiffer, *et al.*, "A 77GHz SiGe Power Amplifier for Potential Applications in Automotive Radar Systems," *Proceedings of RFIC*, pp. 91-94, June 2004.
- [77] I. Aoki, *et al.*, "Distributed Active Transformer: A New Power Combining and Impedance Transformation Techniques," *IEEE MTT*, pp. 316-332, Jan. 2002.
- [78] D. M. Pozar, *Microwave Engineering*, Wiley, 2005.
- [79] E. Worner, C. Wild, W. Muller-Sebert, R. Locher, and P. Koidl, "Thermal conductivity of CVD diamond films: High-precision, temperature-resolved measurements," *Diamond and Related Materials*, Vol. 5, No. 6, pp. 688-692, 1996.
- [80] A. Komijani and A. Hajimiri, "A Wideband 77GHz, 17.5dBm Power Amplifier in Silicon," *Proceedings of IEEE Custom Integrated Circuits Conference*, pp. 571-575, Sept. 2005.
- [81] B. A. Floyd, *et al.*, "SiGe Bipolar Transceiver Circuits Operating at 60GHz," *IEEE Journal of Solid-State Circuits*, vol. 40, no. 1, pp. 156-167, Jan. 2005.
- [82] K. K. Ng, M. R. Frei, and C. A. King, "Reevaluation of the $f_{TBV_{ceo}}$ Limit on Si Bipolar Transistors," *IEEE Trans. on Electron Devices*, vol. 45, no. 8, pp. 1854-1855, Aug. 1998.
- [83] Y. A. Stepanyants, "Experimental Incestigation of Cylindrically Diverging Solitons in an Electric lattice," *Journal of Wave Motion*, vol. 3, pp. 335-341, 1981.

- [84] T. Kuusela, "Soliton Experiments in Transmission Lines," *Journal of Chaos, Solitons, and Fractals*, vol. 5, pp. 2419-2462, 1995.
- [85] A. C. Newell, *Solitons in Mathematics and Physics*, volume 48 of *CBMS-NSF Regional Conference Series in Applied Mathematics*, Society for Industrial and Applied Mathematics (SIAM), Philadelphia, PA, 1985.
- [86] J. W. Miles, "Obliquely Interacting Solitary Waves," *Journal of Fluid Mechanics*, vol. 79, pp. 157-169, 1977.
- [87] J. W. Miles, "Resonantly interacting Solitary Waves," *Journal of Fluid Mechanics*, vol. 79, pp. 171-179, 1977.
- [88] G. Biondini and Y. Kodama, "On a Family of Solutions of the Kadomtsev-Petviashvili Equation which also Satisfy the Toda Lattice Hierarchy," *Journal of Physics A*, vol. 36, 10519-10536, 2003.
- [89] K. E. Lonngren, J. L. Cooney, D. W. Aosey, and J. E. Williams, "A Heuristic Approach to Soliton Soliton Resonant Interaction," *Physica Scripta*, vol. 47, pp. 13-14, 1993.
- [90] M. Born and E. Wolf, *Principles of Optics*, Cambridge, Cambridge, UK, 7th edition, 1999.
- [91] J. W. Goodman, *Introduction to Fourier Optics*, Roberts & Company, Greenwood Village, CO, 3rd edition, 2004.
- [92] C. J. Bouwkamp, "Diffraction Theory," *Reports on Progress in Physics*, vol. 17, pp. 35-100, 1954,.
- [93] J. J. Stamnes, "Focusing of Two-Dimensional Waves," *Journal of Optical Society of America*, vol. 71, pp.15-31, 1981.
- [94] J. J. Stamnes, *Waves in focal regions*, Hilger, Bristol, UK, 1986.

- [95] J. J. Stamnes and H. A. Eide, "Exact and Approximate Solutions for Focusing of Two-Dimensional Waves. I. Theory," *Journal of Optical Society of America A*, vol. 15, pp. 1285-1291, 1998.
- [96] H. A. Eide and J. J. Stamnes, "Exact and Approximate Solutions for Focusing of Two-Dimensional Waves. II. Numerical Comparisons among Exact, Debye, and Kirchhoff Theories," *Journal of Optical Society of America A*, vol. 15, pp. 1292-1307, 1998.
- [97] H. A. Eide and J. J. Stamnes, "Exact and Approximate Solutions for Focusing of Two-Dimensional Waves. III. Numerical Comparisons between Exact and Rayleigh-Sommerfeld Theories," *Journal of Optical Society of America A*, vol. 15, pp. 1308-1319, 1998.
- [98] A. C. Green, H. L. Bertoni, and L. B. Felsen, "Properties of the Shadow Cast by a Half-Screen when Illuminated by a Gaussian-Beam," *Journal of Optical Society of America*, vol. 69, pp. 1503-1508, 1979.
- [99] S. L. Dvorak and H.-Y. Pao, "A New Solution for the Problem of Plane Wave, Diffraction by a 2-D Aperture in a Ground Plane," *IEEE Transactions on Antennas and Propagation*, vol. 53, pp. 2299-2306, 2005.
- [100] J. B. Keller, "Diffraction by an Aperture," *Journal of Applied Physics*, vol. 28, pp. 426-444, 1957.
- [101] J. B. Keller, R. M. Lewis, and B. D. Seckler, "Diffraction by an Aperture .2.," *Journal of Applied Physics*, vol. 28, pp. 570-579, 1957.